universität wien

DISSERTATION / DOCTORAL THESIS

Titel der Dissertation /Title of the Doctoral Thesis

„Levitated optomechanics in vacuum using hollow core photonic crystal fibers and optical cavities“

verfasst von / submitted by

David Grass, MSc

angestrebter akademischer Grad / in partial fulfilment of the requirements for the degree of

Doktor der Naturwissenschaften (Dr. rer. nat.)

Wien, 2018 / Vienna 2018

Studienkennzahl lt. Studienblatt / degree programme code as it appears on the student record sheet:	A 796 605 411
Dissertationsgebiet lt. Studienblatt / field of study as it appears on the student record sheet:	Physik
Betreut von / Supervisor:	Univ.-Prof. Dr. Markus Aspelmeyer

To Ina

Acknowledgements

Now that I am almost finished writing my thesis it comes as a surprise to me that assembling acknowledgements is such a difficult task. Although I am a scientist, which probably means I should be good at characterizing circumstances and conditions, I find it difficult to describe and express my gratitude for all the amazing things that happened to me during my PhD. However I will try... Also, I am almost certain that I will forget someone. If you really know me, you know that I didn't mean to forget you and that I am truly sorry.

First, I want to thank Markus for giving me the opportunity to work together with him and to learn from him. There are many things I am extremely thankful for, but two are outstanding - your motivational skills and your support. No matter how difficult the situation seemed, you always found a way to cheer me up and infect me with your unbridled passion for science. Sometimes this seemingly had to happen via "motivation by sarcasm" or discussing football over a beer. Sometimes I needed the freedom and time to tryout something on my own, and sometimes I just needed the right advice. I feel like you always got me back on track to finish the job.

As our research is a team effort I relied a lot on the help and support of my colleagues and lab-mates. Thank you Nikolai, Uros and Florian for integrating me so well into the group when I first started and teaching me the basics of our work. I hope I didn't give you too much of a hard time back in those days. Also Florian - you can still do it! Us trappers evolved quickly into a portly flock of people that I really enjoy working and discussing with - I hope we can continue this in the future Rainer, Julian, Lorenzo, Manuel, Markus ("the student"), Maxime, Mario, Tobias and Stefan (member of the M.A. group).

Instead of compiling a list along the the lines "who helped me and supported me by doing X", which would certainly go beyond the scope of these acknowledgements, I rather want to list striking moments and events that I will always remember: Uros - walking with me through thick and thin, also in ppp; Florian - I will never forget cycling on a tandem to Bratislava and participating in the Great Gorilla Run; Ralf - although drilling holes into a microwave oven hasn't solved any problems (yet), it surly was a lot of fun; Jonas (and Uros and Florian and ...) - the UnGrassBar was a nice welcome-back surprise; Josh (and all participants) - BMT was a genius move, almost as genius as the trip to the hockey world cup; Josh (again) - the U6 pub crawl was a worthy goodbye, no farewell party can ever live up to it; Sebastian - the shelter-seeking victim of Traunkirchen; Ramon - the only other football fan of the right team; Ralf and Lorenzo - climbing walls together in Benasque was nice for a change; Jonas, Lorenzo, Josh, Uros, Maxime - thanks for taking care of Mrs. Money Penny; Nikolai - Speed Reading and the one million discussions we had. Also, I want

to thank all the people (and alumnis) of our research group that I worked with over the years, maybe not directly, but all of you Michael, Garrett, Jason, Witi, Philipp, Hans, Claus, Mathias, Corentin, Joachim, Sunkung, Jeremias, (tall) Tobias, Karo, Friedrich, Martin, Christian, Thomas and Tom created this very comfortable work environment that I tremendously enjoyed being a part of. I also want to thank the CoQuS doctoral school for all the interesting retreats and events and for giving me the opportunity to go on a secondment.

Besides the professional acknowledgements, besides the help and support of Markus and my coworkers, there are of course family and friends. Without my parents I wouldn't be here today. They raised me to be a curious person and to go out into the world. Their unconditional encouragement and support helped me through my studies and helped me not to give up - thank you for all this. My partner Ina; she is the reason I moved to Vienna in the first place and hence, the reason for me finding my passion in experimental physics. Thank you for bringing me to Vienna and thank you even more for always being there for me when I needed you and for always believing in me. I want to thank my sister and Rainer for their support, for always having a room for me, for all the nice vacations we went on together, which took my mind off work and allowed me to recharge my batteries. I also want to thank my close friends outside work: Mätty and family, Julia and family, Jonas, Patrick and family, Dominik and family, Biene and Clara and Ralle, most of which I don't see as frequent as I would like to. Thanks for being around, keeping me sane and always finding the time for me on the few occasions I make it home. I always enjoy spending time with you - we should do it more often.

David Graß
Vienna, July 2018

Abstract

Optically levitated nanoparticles provide a promising platform for numerous sensing applications as well as fundamental tests of physics. This thesis explores novel approaches for manipulating and controlling such particles in different pressure regimes using nanophotonic structures and optical cavities.

In the first part, a novel optical trap for nanoparticles utilizing hollow core photonic crystal fibers is presented. The optical control and read-out allows particle transport over unprecedented distances and feedback cooling inside the fiber, which are relevant for loading nanoparticles into ultra-high vacuum. Using the levitated nanoparticle as a localized pressure sensor, also allows to directly study the hydrodynamic properties of the hollow core fiber channel. Our measurements are confirmed by DSMC simulations of the nonlinear Boltzmann equation and rule out previous, simplified models of the pressure distribution in narrow channels.

In the second part, an optically trapped nanoparticle is coupled to a Fabry-Pérot cavity at high vacuum. This is achieved by overlapping an optical dipole trap with the TEM00 mode of a compact high-finesse cavity. Three-dimensional feedback cooling inside the dipole trap allows stable operation of the optomechanical system in high vacuum. Compared to our previous experiments, the new architecture reduces the mechanical losses by at least six orders of magnitude and shows a promising route towards room-temperature quantum control.

Zusammenfassung

Optisch levitierte Nanoteilchen offerieren eine vielversprechende Plattform für zahlreiche Sensorikanwendungen als auch für fundamentale Tests der Physik. Diese Arbeit sondiert neue Ansätze zur Manipulation und zur Kontrolle dieser Teilchen in unterschiedlichen Druckbereichen unter der Verwendung von nanophotonischen Strukturen und optischen Resonatoren.

Im ersten Teil wird eine neue optische Falle die photonische Hohlkernkristallfasern verwendet präsentiert. Die optische Kontrolle und das optische Auslesen erlauben den Transport von Teilchen über noch nie da gewesene Entfernungen sowie das Rückkopplungskühlen innerhalb der Faser. Beides ist relevant um Nanoteilchen in Ultrahochvakuum zu laden. Die Verwendung des levitierten Nanoteilchens als lokalisierten Drucksensor erlaubt es die hydrodynamischen Eigenschaften des Hohlkernkanals direkt zu untersuchen. Unsere Messungen sind mit DSMC Simulationen der nichtlinearen Boltzmanngleichung bestätigt und wiederlegen vorhergegangene, vereinfachte Modelle von Druckprofilen in

engen Kanälen.

Im zweiten Teil wird ein optisch levitiertes Nanoteilchen an einen Fabry-Pérot Resonator im Hochvakuum gekoppelt. Dies wird verwirklicht indem eine optische Dipolfalle mit der TEM00 Mode eines Resonators hoher Güte überlagert wird. Dreidimensionales Rückkopplungskühlen in der Dipolfalle ermöglicht zuverlässigen Betrieb des optomechanischen Systems im Hochvakuum. Verglichen mit unserem vorhergehenden Experiment werden durch die neue Architektur die mechanischen Verluste um mindestens sechs Größenordnungen reduziert und der Ansatz zeigt einen vielversprechenden Weg zu Raumtemperaturquantumkontrolle auf.

Abbreviations

AOM	acousto-optical modulator
COM	center of mass
CPB (CCPB)	clockwise (counterclockwise) propagating beam
DSMC	direct simulation Monte Carlo
fbL	feedback logic
FSR	free spectral range
GLMT	Generalized Lorentz-Mie theory
GRIN	gradient index
HCPCF	hollow core photonic crystal fiber
LM	locking mode
LO	local oscillator
LP	linear polarized
NA	numerical aperture
NEB	nebulizer
OMC	optomechanical cavity
OMIT	optomechanically induced transparency
PBS	polarizing beamsplitter
ppm	parts per million
SMF	single mode fiber
TIR	total internal reflection
vacL (vacR)	left (right) vacuum chamber
VNA	vector network analyzer
WD	working distance

Contents

List of Figures

1. Prologue

Optical levitation is a field pioneered by Arthur Ashkin [1, 2] who realized that small dielectric objects can be trapped and manipulated with light. The first experimental optical trap in vacuum [3] gave already a hint on the unique properties of levitated systems. A silicon oil drop trapped at a pressure of $p \approx 10^{-6}$ mbar was kicked and started oscillating with a ringdown time of 4.5 h. A more quantitative measure of this property is the mechanical quality factor $Q = \Omega_\mathrm{m}/\gamma$ which compares the oscillation period Ω_m with the mechanical damping γ. The number is a measure for how often the particle oscillates until half of its energy is dissipated. For optically levitated systems numbers as high as $Q = 10^8$ (see [4]) have been measured and are predicted [5] to reach $Q = 10^{12}$. Therefore, a levitated object can be extremely well decoupled from its environment. The application of optical levitation was quickly expanded to atoms [6], contributing significantly to the field of atomic physics [7], and to biophysics by trapping bacteria and viruses [8].

This thesis presents two recent further developments in optical levitation. First, a novel optical trap based on a hollow core photonic crystal fiber (HCPCF) and its application for sensing and micro-manipulation are described. HCPCFs are microstructured optical fibers with the optical mode located inside a hollow core. The ability to confine light in air or vacuum over long distances in HCPCFs were already utilized to trap and guide atoms [9, 10] and dielectric particles of micrometer size [11–13]. Here, the use of the HCPCF trap is extended to optically levitate and manipulate dielectric particles in the intermediate range, between 100 nm and 1 μm. The combination of levitated nanometer-sized particles and HCPCFs allows us to access a new parameter regime for sensing with novel experimental measurement techniques and provides a promising tool for fundamental physics experiments.

In the second part of this thesis, we build up on our previous levitated cavity optomechanics experiments [14]. Such experiments [15] promise access to a new parameter regime for both, fundamental tests of quantum mechanics [16, 17] and ultra-sensitive force detection [18, 19] at room temperature. While current state of the art (non-levitated) optomechanical experiments routinely operate in the quantum regime, e.g. sideband cooling into the ground state of motion [20, 21], generation of non-classical states of light [22–24], generation of non-classical correlations between mechanical motion and light [25], generation of non-classical states of motion [26], generation of entanglement between light and mechanical motion [27] and generation of entanglement between two mechanical oscillators [28], this is still an outstanding goal for levitated optomechanics. While our previous experiment [14] was limited by particle loss from the optical trap around $p \approx 1$ mbar here we make it operational in high vacuum by combining it with an optical tweezer. This step pushes the quan-

tum cooperativity C_Q of the combined system by five orders of magnitude ($C_Q = 0.02$), thereby closing in onto full quantum control ($C_Q > 1$).

2. Optical Levitation With Hollow Core Photonic Crystal Fibers

Hollow core photonic crystal fibers (HCPCF) are micro-structured optical fibers with a hollow core in which the optical mode is located. In stark contrast to conventional fibers, where the mode is located in the high refractive index region, HCPCFs allow guiding of light in the gas or vacuum filled low index domain of the fiber. This is possible because the photonic crystal surrounding the hollow core provides a two-dimensional bandgap for optical frequencies [29], prohibiting light from leaving the core. In comparison, conventional optical fibers rely on total internal reflection (TIR) as the underlying guiding mechanism, which requires a higher refractive index material in the fiber core than in the cladding. Since, at optical frequencies, there is no material with a lower refractive index than air (or vacuum), guidance in an air core is not possible by means of TIR. Figure 2.1 a) shows a darkfield photograph of a hollow

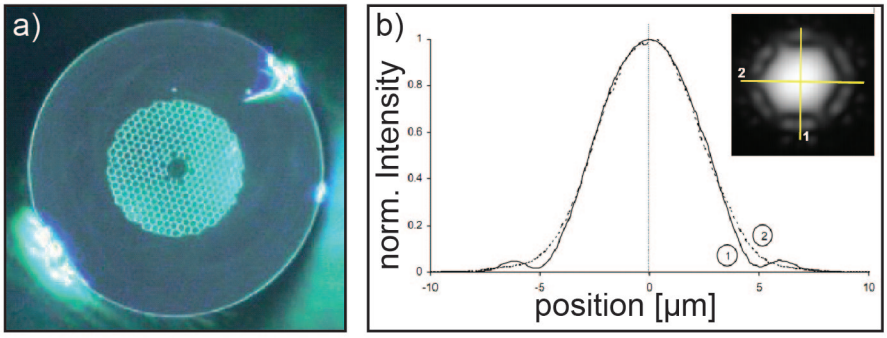

Figure 2.1.: Part a) displays a dark field microscope image of a HC1060 HCPCF from NKT Photonics. Part b) shows the manufacturer specification [30] of the HC1060. The intensity profiles along the two yellow lines in the inset are shown.

core photonic crystal fiber (NKT Photonics: HC1060). The photonic crystal surrounding the air core creates a full two-dimensional bandgap for a center wavelength $\lambda = 1060$ nm. It prevents light from penetrating the cladding and hence forms an optical mode inside the hollow region. In figure 2.1 b) the intensity profile of the fundamental mode is shown. Along the two orthogonal axes the intensity profile is well approximated by a Gaussian shape.

The first realization of a hollow core photonic crystal fiber was reported by Cregan et al. in 1999 [31]. The outstanding property of light confinement over long distances in air or vacuum enabled new experiments and applications, just to name a few: HCPCFs were used to guide [9] and trap atoms [10], for high power laser beam delivery (continuous wave and pulsed) [32], for laser beam delivery (continuous wave, pulsed, ultra-violet and supercontinuum) into ultra-high vacuum [33], for compact and efficient all-fiber gas cells [34] and for

excitation of caesium atoms to Rydberg states inside HCPCF [35]. Yet another application is guidance [11] and trapping [12] of micrometer-sized dielectric particles by means of radiation pressure, trapping with the aid of opto-thermal forces [36], and transport of micrometer-sized particles with a mode-based conveyor belt [13]. For further reading about hollow core fibers and their applications the reader is referred to [37–41].

The principle idea of our hollow core fiber experiment is sketched in figure 2.2. A HCPCF is mounted between two vacuum chambers (vacL and vacR) in which the pressure can be controlled individually. Two counterpropagating

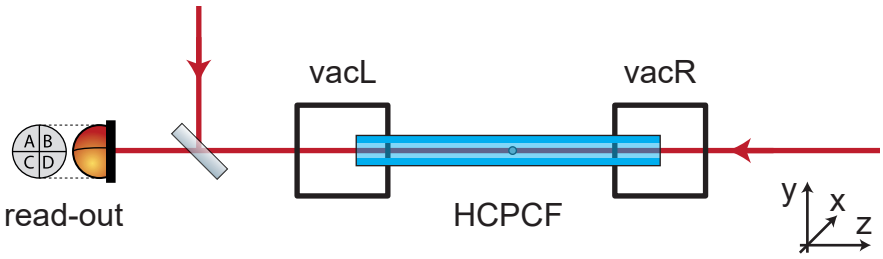

Figure 2.2.: Two counterpropagating lasers are focused into a hollow core photonic crystal fiber, mounted between two vacuum chambers (vacL and vacR) and form an optical trap. A nanoparticle is trapped inside the hollow core fiber and its motion can be detected optically (read-out).

laser beams coupled into the HCPCF form a standing wave which serves both, as optical trap and as optical conveyor belt. A dielectric particle trapped in an intensity maximum of the standing wave can be transported along the fiber. In addition, an all-optical read-out monitors the motion of the particle in three dimensions and is used for feedback cooling.

The following chapter is divided into five sections:

- Chapter 2.1 is devoted to the theory of optical levitation using HCPCF. The electromagnetic modes of the HCPCF are used to numerically compute the optical forces with generalized Lorentz-Mie theory (GLMT). The results are compared with the analytical Rayleigh approximation, which is also used to derive the harmonic oscillator model for levitated particles. Finally, two consequences of the multimode structure are discussed: Modulation of trapping position and frequency along the HCPCF and all-optical, three-dimensional read-out of the particle motion.

- Chapter 2.2 describes the experimental setup and procedures. The optical setup is divided into three parts which are explained separately:

Beam preparation, optical trapping and read-out. The following two parts describe how to cleave and mount HCPCFs and how the optical conveyor belt is implemented. The last part presents characterisation measurements of the HCPCF trap.

- Chapter 2.3 introduces linear feedback cooling, both, from a theoretical and an experimental perspective. Feedback cooling is performed optically along the fiber axis with an additional laser and electrically along one radial direction with a charged particle.

- Chapter 2.4 discusses the potential of the HCPCF experiment for controlled and deterministic particle loading into ultra-high vacuum. The important parameters defining the performance of the source are characterized and the current status on the next generation experiment, which is entirely fiber based, is summarized.

- Chapter 2.5 investigates the hydrodynamical properties of the HCPCF. The HCPCF is a narrow channel connecting two vacuum chambers in which the pressure can be controlled individually. A levitated particle is used as nanomechanical pressure sensor to measure the pressure profile along the fiber. We experimentally investigate a new parameter regime for the first time and our results are backed up by direct simulation Monte Carlo (DSMC) methods.

2.1. Principles of Optical Levitation inside Hollow Core Photonic Crystal Fibers

This chapter introduces optical levitation with a HCPCF based trap. The underlying principles of optical levitation are described in more detail elsewhere, for example [42–44]. Here the emphasis lies on the system specific physics.

2.1.1. The Electromagnetic Field inside Hollow Core Fibers

Hollow Core Photonic Crystal Fiber Modes

The mode structure of hollow core photonic crystal fibers can be approximated with linear polarized (LP_{mn}) modes [45, 46], which are also used to describe the modes in conventional fibers. The LP modes in cylindrical coordinates are

$$\begin{aligned} \mathrm{LP}^{j}_{mn}(r,\phi,z)\vec{p} &= E_0 J_m\left(\frac{u_{mn}r}{r_{\mathrm{co}}}\right)\cos(n\phi - j\frac{\pi}{2})e^{-i\beta_{mn}z}\vec{p} \\ &= E_0\varepsilon_{mn}(r,\phi)e^{-i\beta_{mn}z}\vec{p} \end{aligned} \tag{2.1}$$

with E_0 the electric field, J_m Bessel functions of the first kind, u_{mn} the n-th root of the m-th Bessel function, r_{co} the radius of the hollow core , $\vec{p}$ the polarization vector and the propagation constant

$$\beta_{mn} = \frac{2\pi}{\lambda}\left[1 - \frac{1}{2}\left(\frac{u_{mn}\lambda}{2\pi r_{\mathrm{co}}}\right)^2\right] \tag{2.2}$$

with λ the wavelength of the electromagnetic field in vacuum. The radial

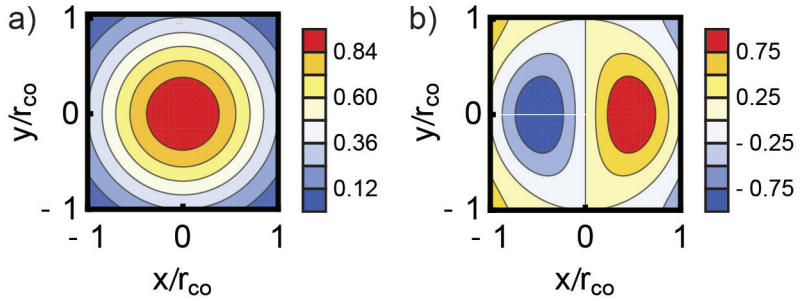

Figure 2.3.: Radial electric field distribution of the fundamental fiber mode ε_{01} a) and the first higher order mode ε_{11} b)

profile is lumped into the function $\varepsilon^{j}_{mn}(r,\phi)$. Throughout this thesis only the fundamental mode LP_{01} and the first higher order mode LP_{11} are of relevance.

Without loss of generality we consider $j = 0$ which means the mode LP_{11} is oriented along the x-axis, as shown in figure 2.3 b). The second mode LP_{11} with $j = 1$ is oriented along the y-axis (a 90° degree rotation of figure 2.3 b)). Without active mode stabilization in the experiment, the LP_{11} mode appears in an arbitrary superposition of $j = 0$ and $j = 1$. Figure 2.3 a) shows the radial electric field distribution of the mode LP_{01}.

Standing Wave Intensity Profile

A Gaussian laser beam with wavelength λ and polarization $\vec{p}$ is coupled from one side into a HCPCF and a second Gaussian beam of same power, wavelength and polarization is coupled from the other side into the HCPCF. The Gaussian beams mainly excite the fundamental mode LP_{01} and due to imperfect alignment the higher order mode LP_{11} is weakly excited. The electric field inside the HCPCF is

$$\vec{E}(r,\phi,z) = E_{01}\varepsilon_{01}e^{i\beta_{01}z}\vec{p} + E_{11}\varepsilon_{11}e^{i\beta_{11}z}\vec{p} + E_{01}\varepsilon_{01}e^{-i\beta_{01}z}\vec{p} + E_{11}\varepsilon_{11}e^{-i\beta_{11}z}\vec{p}. \tag{2.3}$$

It is assumed that the power of the fundamental and the higher order mode are the same for beams propagating in $+z$ and in $-z$ direction, respectively. The intensity in the fiber is proportional to

$$\begin{aligned} I &\propto |\vec{E}|^2 \\ &= 2P_{01}\varepsilon_{01}^2\Big[1+\cos(2\beta_{01}z)\Big] + P_{11}\varepsilon_{11}^2\Big[1+\cos(2\beta_{11}z)\Big] + \\ &+ 4\sqrt{P_{01}P_{11}}\varepsilon_{01}\varepsilon_{11}\Big[\cos(\Delta\beta z)+\cos(\Sigma\beta z)\Big] \end{aligned} \tag{2.4}$$

with $\Delta\beta = \beta_{01} - \beta_{11}$ and $\Sigma\beta = \beta_{01} + \beta_{11}$. The optical power is related to the electrical field via $E_{mn} \propto \sqrt{P_{mn}}$. The first two terms in equation 2.4 are standing waves of the fundamental and higher order mode and their wavelength is given by $\pi/\beta_{01} \approx \pi/\beta_{11} \approx \lambda/2$, similar to a standing wave in free space. The last two terms describe interference between the fundamental and the higher order mode. The interference occurs with two wavelengths: $2\pi/\Sigma\beta \approx \lambda/2$ which is comparable to a free space standing wave and $2\pi/\Delta\beta \approx 400 \times \lambda/2$ which is much longer than the free space standing wave pattern. Figure 2.4 is a plot of the intensity distribution across the x-z plane, averaged over the fast oscillating standing wave terms of equation 2.4. Due to the interference between the fundamental and the higher order mode, the intensity maxima oscillate around the fiber axis with a modulation wavelength $2\pi/\Delta\beta$. For comparison, in a standing wave of two counterpropagating LP_{01} modes only, the same plot would be invariant along the z-axis with all the intensity maxima

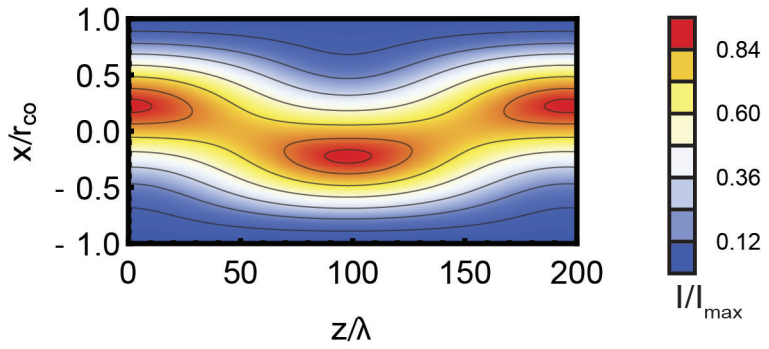

Figure 2.4.: Intensity distribution inside a HCPCF averaged over the standing wave contributions along the z-direction. The interference between fundamental and higher order mode lead to a modulation of the intensity around the fiber axis.

on the fiber axis. Figure 2.5 a) is a plot of the intensity distribution (without averaging) in the region around $z = 0$ (the fiber entrance) and figure 2.5 b) around $z = 100/\lambda$ (inside the fiber). The intensity maxima are off-axis compared to a standing wave composed of two counterpropagating LP_{01} modes. The modulation wavelength of the maxima is $\approx \lambda/2$.

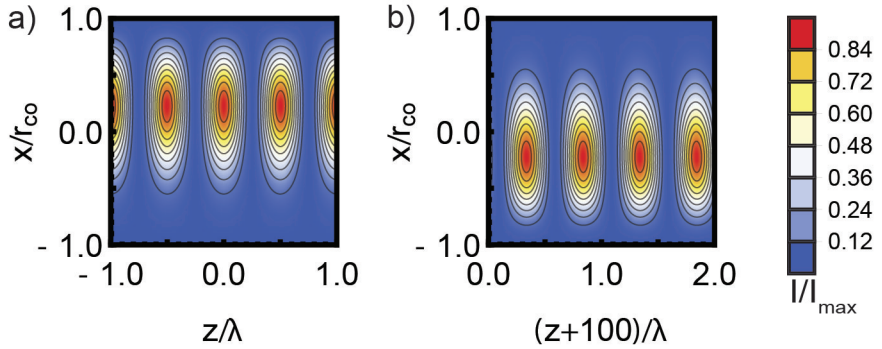

Figure 2.5.: Intensity distribution inside a HCPCF. Due to interference between fundamental and higher order mode the standing wave maxima are up-shifted a) and down-shifted b) with respect to the fiber axis.

2.1.2. Optical Forces

Maxwell's equations provide the most general Ansatz to compute forces of an electromagnetic field on a dielectric object. Integration of the Maxwell stress

tensor over a surface enclosing the dielectric object returns the mechanical force acting on the object [47]

$$\langle \vec{F} \rangle = \oint_{\partial V} \langle \mathbf{T} \rangle d\vec{n}$$

with $\mathbf{T}$ the Maxwell stress tensor, ∂V a surface enclosing the dielectric object and $\vec{n}$ the unit vector perpendicular to the surface. The time dependence of the electromagnetic field can be averaged $\langle ... \rangle$ as the oscillations of the electromagnetic field are much faster than any mechanical response. The Maxwell stress tensor contains the incident fields impinging on and scattered off the dielectric object. The forces acting on the dielectric object are a consequence of energy and momentum conservation of incident and scattered fields. Hence, in order to compute the optical forces the scattering problem of the field and the dielectric object needs to be solved first.

The most general solution for a spherical particle illuminated by a plane wave is Lorentz-Mie theory, which provides an analytical solution in form of an infinite series. Generalized Lorentz-Mie theory takes focused Gaussian modes (instead of plane waves) into account, see Gousbet and Gréhan [48] for further reading. In the special case of particles with radius a much smaller than the wavelength λ of the electromagnetic field ($a \ll \lambda$) the Rayleigh approximation is applicable [49, 50]. The Rayleigh approximation provides analytical, closed formulas to compute the optical forces. The experiments described in this chapter are used to levitate particles of a radius $a \approx 200$ nm and $a \approx 500$ nm with a laser of wavelength $\lambda = 1064$ nm. In order to verify that the Rayleigh approximation is still applicable the results are compared with GLMT (generalized Lorentz-Mie theory) simulations. The optical tweezers computational toolbox from Nieminen et al. [51] is used for the GLMT computations.

Rayleigh Approximation

The Rayleigh (or dipole approximation) treats the case of a particle that is small with respect to the trapping laser wavelength $a \ll \lambda$. The particle is described as a point dipole and its interaction with an electromagnetic field can be separated into two components: Scattering force and gradient force. A dielectric particle illuminated with a laser will either absorb, reflect (or scatter) or transmit the impinging photons. Each absorbed photon transfers a momentum $p = h/\lambda$ and each reflected photon transfers a momentum $p = 2h/\lambda$ onto the particle, resulting in an effective force along the direction of beam propagation. This type of interaction is called scattering force. Lets assume the incident photons have zero transverse momentum. All photons transmitted trough the particle will be diffracted (as a dielectric particle has a optical density $n > 1$) and acquire a non-zero transverse momentum component. Due to

momentum conservation there has to be a momentum transfer onto the particle. This component of the light-matter interaction is referred to as gradient force.

Harada and Asakura derived explicit analytical expressions for scattering and gradient force [50] which will be applied to the HCPCF system. The scattering force $\vec{F}_{\text{scatt}}$ of a laser beam propagating in z-direction is $\vec{F}_{\text{scatt}} = \sigma_{\text{scatt}}/cI\vec{e}_z$ proportional to the intensity I of the laser beam and the scattering cross-section $\sigma_{\text{scatt}} = 8\pi k^4 a^6/3(\varepsilon-1)^2/(\varepsilon+2)^2$ of the particle (a: particle radius, ε: dielectric constant of the particle, c: speed of light) and $\vec{e}_z$ the unit vector along the z-axis. The HCPCF trap consists of two counterpropagating laser beams of equal intensity. Therefore, the scattering force of one beam is the same as the scattering force of the counterpropagating beam with opposite sign and the resulting mean scattering force vanishes $\vec{F}_{\text{scatt}} = 0$. The gradient force $\vec{F}_{\nabla}$ is given [50] by

$$\vec{F}_{\nabla} = \frac{\alpha}{2}\nabla\vec{E}^2 \tag{2.5}$$

with $\alpha = 4\pi a^3\varepsilon_0(\varepsilon-1)/(\varepsilon+2)$ the polarizability of the particle. The polarizability is a measure for the induced dipole moment inside the particle. ε is the dielectric constant of the particle and ε_0 is the vacuum permittivity. The gradient force is proportional to the direction of the steepest slope of the intensity and attracts particles towards the highest intensity. For this reason dielectric particles are called high-field seeker. The gradient force can confine a particle in all three dimensions and counteracts displacements away from the intensity maxima. The gradient force can be used to stably levitate (or trap) particles.

Harmonic Approximation

Optically levitated particles in a gaseous environment are subject to thermal noise via collisions with surrounding gas molecules. If the particle is displaced by a collision, the gradient force acts in the opposite direction counteracting the displacement. For small displacements of the particle with respect to the next local intensity maximum, the gradient force can be approximated with a linear Hooke's law. The standing wave intensity distribution is locally approximated with a three-dimensional harmonic profile. Figure 2.6 shows the exact intensity profile (see equation 2.4) inside a HCPCF along x- (red dots), y- (green dots) and z-direction (blue dots) and a local fit of a harmonic function (solid lines). The fit function is

$$I_{\text{harm}} \propto E_0^2\left[\frac{a_x}{2}(x-x_0)^2 + \frac{a_y}{2}(y-y_0)^2 + \frac{a_z}{2}(z-z_0)^2\right] \tag{2.6}$$

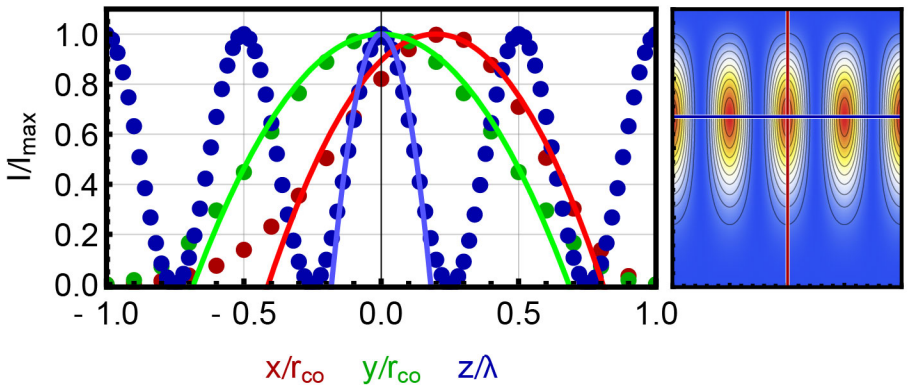

Figure 2.6.: Intensity distribution inside a HCPCF (see equation 2.4) along x-axis (red dots), y-axis (green dots) and z-axis (blue dots). The inset on the right is a contour plot of the intensity in the x-z plane. The red (blue) line correspond to the intensity along the x- (y-) direction in the left plot. The solid lines are fits to a harmonic function.

with a_x, a_y, a_z and x_0, y_0, z_0 as free fit parameters. The a_i parameters are a measure for the local curvature of the electric field around the intensity maximum x_0, y_0, z_0 respectively. The force on a dielectric particle in the proximity of an anti-node can be calculated with equation 2.5:

$$\vec{F}_\nabla = \alpha E_0^2 \Big[a_x(x - x_0)\vec{e}_x + a_y(y - y_0)\vec{e}_y + a_z(z - z_0)\vec{e}_z \Big]. \tag{2.7}$$

Equation 2.7 describes a three-dimensional restoring force around the intensity maximum (x_0, y_0, z_0) and allows to spatially confine a dielectric particle in a finite volume, hence optical trapping. The gradient force is conservative and can be written as gradient of an optical potential $\vec{F}_{\text{grad}} = -\nabla U_{\text{opt}} = -\nabla(-\frac{\alpha}{2} E^2_{\text{harm}})$. The combined system of a trapped dielectric particle and the electromagnetic field inside a HCPCF is well described by a three-dimensional harmonic oscillator. The oscillation frequencies in each spatial direction are $\Omega^i_{\text{m}} = \sqrt{\kappa_i / m}$ with m the mass of the dielectric particle and κ_i the spring constant along each spatial direction

$$\kappa_i = \frac{\partial^2 U_{\text{opt}}}{\partial i^2} = \alpha a_i E_0^2. \tag{2.8}$$

Interestingly, the oscillation frequencies in the Rayleigh approximation do not depend on the particle size, since both, polarizability α and particle mass m scale with volume, hence

$$\Omega^i_{\text{m}} = \sqrt{3E_0^2 \frac{a_i \varepsilon_0}{\rho} \varepsilon_0 \frac{\varepsilon - 1}{\varepsilon + 2}}. \tag{2.9}$$

The mechanical frequencies in the Rayleigh approximation are proportional to the square root of the optical power $E^2 \propto P$ of the laser beam, its curvature a_i and the square-root of the inverse particle density ρ.

Generalized Lorentz-Mie Theory

The Rayleigh approximation described in chapter 2.1.2 requires the particle radius to be much smaller than the wavelength of the trapping laser $a \ll \lambda$. However, in the current HCPCF experiments particles with a radius of either 200 nm or 500 nm and a trapping laser with $\lambda = 1064$ nm are used. The applicability of the Rayleigh regime is tested with GLMT computations to back up the analytical results from the previous section.

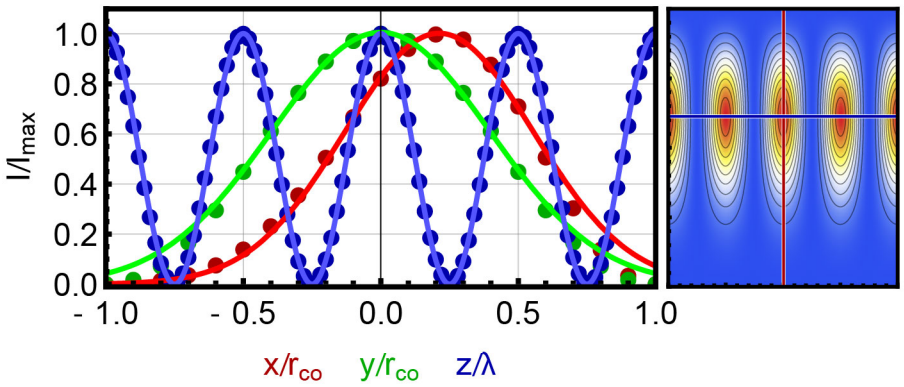

Figure 2.7.: Intensity distribution inside a HCPCF (see equation 2.4) along x-axis (red dots), y-axis (green dots) and z-axis (blue dots). The inset on the right is contour plot of the intensity in the $x - z$ plane. The red (blue) line correspond to the intensity along the x- (y-) direction in the left plot. The solid lines are fits to a Gaussian standing wave.

Instead of running the simulation with the intensity distribution inside the HCPCF described by equation 2.4, which is complicated due to multiple Bessel functions, the intensity distribution will be locally parametrized with two counterpropagating Gaussian beams. The dots in figure 2.7 represent the exact intensity inside the HCPCF given by equation 2.4 and the solid lines are a fit to a standing wave composed of two counterpropagating Gaussian beams. Figure 2.8 a) displays the optical force acting on a 200 nm silica particle and figure 2.8 b) on a 500nm silica particle. The points are GLMT simulations and the solid lines are computed with the Rayleigh approximation. Interestingly, the difference between the force computed with GLMT and the Rayleigh

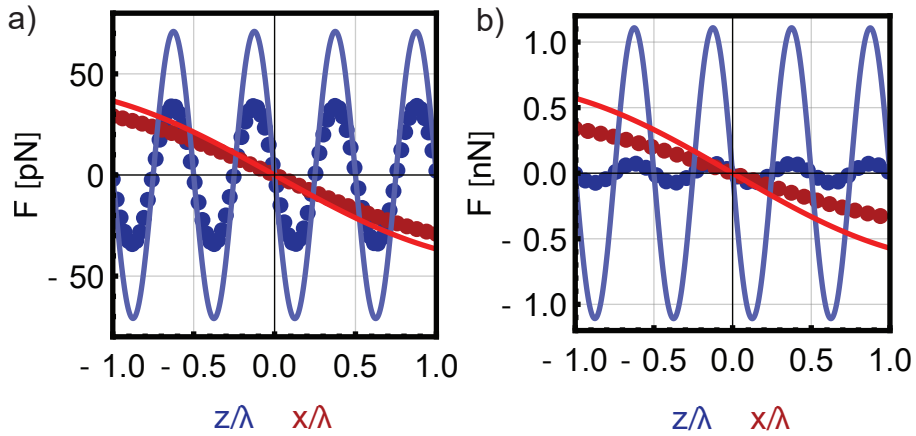

Figure 2.8.: Optical forces on a $a = 200$ nm (figure a)) and on a $a = 500$ nm (figure b)) silica particle along x- (red) and z-direction (blue). The dots are numerical simulations of GLMT and the solid lines are computed using the Rayleigh approximation.

approximation is a constant factor that only depends on the particle radius and direction. Figure 2.9 shows the same data as in figure 2.8 except that the Rayleigh data is rescaled by a factor of 2.08 (15.15) along the axial direction and by 1.27 (1.69) along the radial direction for a particle size of $a = 200$nm ($a = 500$nm). The plot confirms that the Rayleigh approximation and GLMT simulation differ only by a single multiplicative factor (dependent on particle radius and direction). The difference between axial and radial direction is due

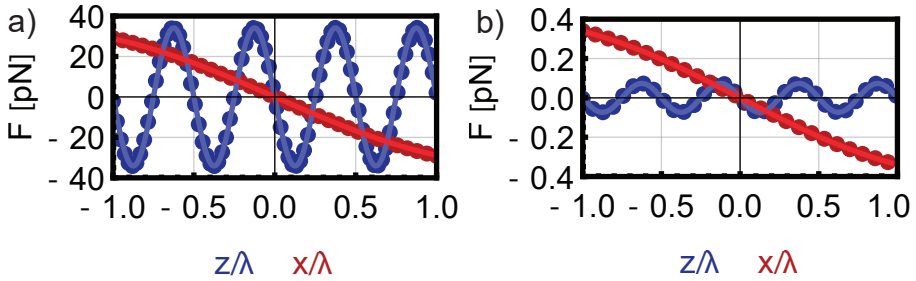

Figure 2.9.: Rescaled version of figure 2.8: Optical forces acting on a $a = 200$ nm (figure a)) and a $a = 500$ nm (figure b)) silica particle along x- (red) and z-direction (blue). The dots are the unchanged numerical simulations of GLMT and the solid lines are rescaled Rayleigh approximations.

to the standing wave trap. The Rayleigh approximation assumes a uniform

electric field surrounding the particle [52]. Along the standing wave direction, this condition is violated sooner compared to the radial directions. In order to investigate this effect further the optical forces for a wide range of radii are simulated.

Figure 2.10 displays the ratio between GLMT and Rayleigh approximation versus particle radius along z- (blue) and x-direction (red). For radii $a \ll \lambda$ the Rayleigh approximation coincides with GLMT, their ratio is almost one. For an increasing radius the Rayleigh approximation overestimates the optical forces. It is interesting to realize that the axial force ratio becomes negative in

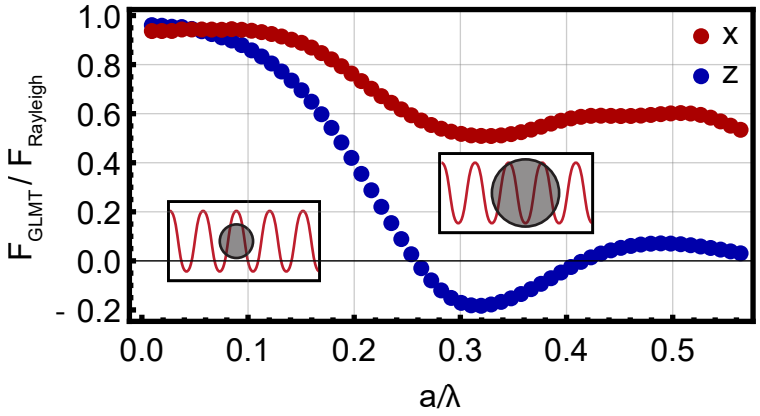

Figure 2.10.: Ratio between GLMT simulations and Rayleigh approximation for varying radii a along z- (blue) and x-direction (red). The insets show trapping positions with respect to the standing wave for a particle with $a/\lambda = 0.1$ and $a/\lambda = 0.3$.

a region of $a/\lambda \approx 0.3$. Within this region the particle diameter is comparable to one wavelength of the standing wave. The particle encloses one antinode and extends into the two neighbouring antinodes. It will feel the same attracting force to the left and to the right antinode and therefore it is no longer a stable trapping position. Instead, the particle will be trapped in a node of the field which is the new stable trapping position making the particle effectively a low-field seeker [53].

2.1.3. Consequences of Higher Order Modes for Optical Levitation

The interference between the modes LP_{01} and LP_{11} leads to a radial position modulation of the intensity maxima around the fiber center with a wavelength of $2\pi/\Delta\beta$, as already shown in figure 2.4 and figure 2.5. A direct consequence

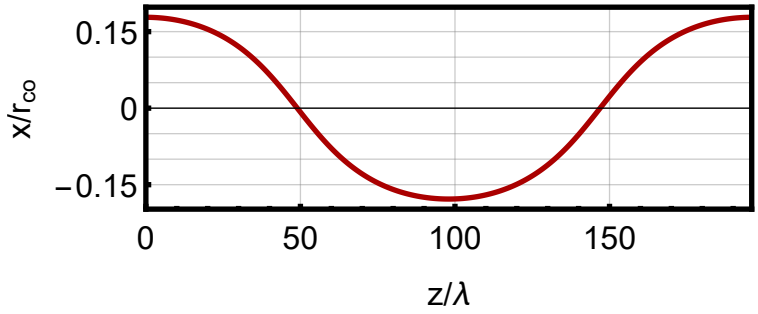

Figure 2.11.: The interference between mode LP_{01} and LP_{11} leads to a modulation of the intensity maxima around the fiber center. The red line indicates the positions of local intensity maxima of the standing wave, the position where a particle can be trapped.

is that particles, depending on there z-position along the fiber, are trapped off-center. Figure 2.11 plots the positions of the intensity maxima in the x-z-plane. Note that the trapping positions themselves are not a continuum, they are equally spaced by the wavelength of the standing wave.

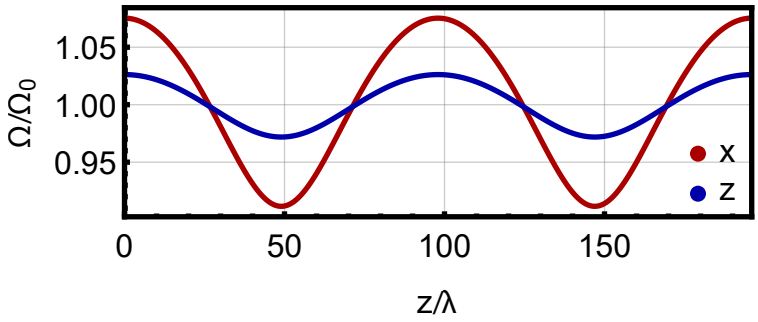

Figure 2.12.: The interference between mode LP_{01} and LP_{11} modulates the intensity maxima of the standing wave and therefore the local mechanical frequency of the oscillator. The blue (red) line are the normalized trapping frequencies along z-direction (x-direction).

The presence of a higher order mode does not only affect the radial trapping position, but also the mechanical frequencies Ω_m. The mechanical frequency is directly proportional to the square-root of the intensity and hence is modulated by a wavelength of $\pi/\Delta\beta$. A simulation of the normalized mechanical frequency $\Omega_z(z)/\Omega_0$ (blue) and $\Omega_x(z)/\Omega_0$ (red) along the fiber axis are shown in figure 2.12. Ω_0 is the mean mechanical frequency averaged over the z-position or the x-position inside the fiber. This dependence is used to infer the optical

power in the higher order mode LP_{11} as well as the hollow core radius r_{co}.

2.1.4. Equation of Motion of the Hollow Core Photonic Crystal Fiber Trap

The dynamics of the center of mass (COM) motion of a trapped particle inside a HCPCF can be described by a thermally driven, damped, three-dimensional harmonic oscillator. This description is only valid for small amplitudes of the particle, otherwise the anharmonicity of the potential needs to be considered [4]. In case the anharmonicity is negligible, the three dimensions are decoupled and each can be considered independently. Here, only one dimension is described, the expansion to three dimensions is straight forward. The Langevin equation for a levitated particle in one dimension is [54]

$$m\ddot{z} + m\gamma_{\mathrm{p}}\dot{z} + m\Omega_{\mathrm{m}}^2 = F_{\mathrm{th}} \tag{2.10}$$

with m the mass and Ω_{m} the mechanical frequency of the particle. Collisions with surrounding gas molecules cause a Stokes-like friction force $F = m\gamma_{\mathrm{p}}\dot{z}$ and a Brownian stochastic force noise F_{th} [55] coupling the COM motion to a thermal bath at room temperature $T_0 \approx 300$ K.

Mechanical Damping γ_{p} and Thermal Force Noise F_{th}

The trapped particle moves inside an environment of finite pressure p. Gas molecules will constantly hit the particle causing two interactions: a Stokes friction force $m\gamma_{\mathrm{p}}\dot{x}$ proportional to the velocity, damping the particle motion, and a Brownian force noise F_{th} at room temperature [55] driving the motion of the particle. The damping depends on the local pressure p of the gas surrounding the particle and is given by [56]

$$\gamma_{\mathrm{p}} = \frac{6\pi\eta a}{m}\frac{0.619}{Kn + 0.619}\left(1 + \frac{0.310\mathrm{Kn}}{\mathrm{Kn}^2 + 1.152\mathrm{Kn} + 0.785}\right) \tag{2.11}$$

with η the gas viscosity and $\mathrm{Kn} = \Lambda_{\mathrm{free}}/a$ the Knudsen number, which is the ratio of mean free path of a gas molecule Λ_{free} and the particle radius a. Formula 2.11 contains the conventional Stokes friction $\gamma = 6\pi\eta a/m$ and a correction factor for low pressures, as Stokes friction only holds for incompressible fluids. If the mean free path of gas molecules becomes larger than the particle radius, the mechanical damping can be simplified [4, 57] to

$$\gamma_{\mathrm{p}} \underset{\Lambda_{\mathrm{free}} \gg a}{\approx} 15.8\frac{a^2 p}{m v_{\mathrm{gas}}} \tag{2.12}$$

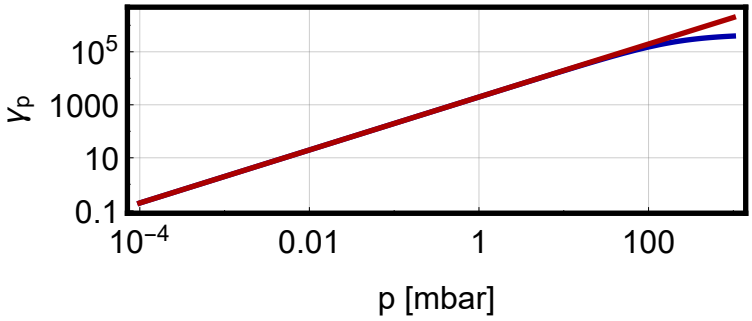

Figure 2.13.: Mechanical damping versus pressure (blue curve) for a 200 nm silica particle. The linear approximation (red curve) overestimates the damping at high pressures.

with v_{gas} the mean thermal velocity of gas molecules. The linear scaling of mechanical damping (or losses) with background pressure makes levitated particles a promising candidate for ultra-high Q oscillators [5]. Figure 2.13 compares the two equations for the pressure dependence of mechanical damping for a $a = 200$ nm silica particle immersed in air.

Spectrum of the Mechanical Motion

The noise-power spectral density of a mechanical oscillator is given by [55]

$$S_{\mathrm{zz}}(\omega) = \frac{2k_{\mathrm{B}}T\gamma_{\mathrm{p}}}{\pi m}\frac{1}{(\Omega_{\mathrm{m}}^2 - \omega^2)^2 + \gamma_{\mathrm{p}}^2\omega^2}. \tag{2.13}$$

This equation is derived by taking the Fourier transform of equation 2.10. The Wiener-Khinchin theorem [58] relates the Fourier transform of the spectral density with the autocorrelation function of the displacement

$$\langle z(t)z(t-t')\rangle = \int d\omega \langle \tilde{z}(\omega)\tilde{z}(\omega)^*\rangle e^{i\omega t}.$$

For the special case of $t = 0$ the mean square displacement is given by the area of the spectral density

$$\langle z^2\rangle = \int d\omega S_{\mathrm{zz}}(\omega). \tag{2.14}$$

For a system described by the equation of motion 2.10, equation 2.14 can be used to assign a temperature to the COM motion using the equipartition theorem $k_{\mathrm{B}}T = m\Omega_{\mathrm{m}}^2\langle z^2\rangle$. The integral of the mechanical spectrum S_{zz} is directly proportional to the COM temperature. This relation will appear again in chapter 2.3 to quantify the effect of feedback cooling. Note that for anharmonic potentials [4] or oscillators which couple to more than one bath [59, 60] a more careful assignment of the mode temperature is required [61].

2.1.5. Three-Dimensional Read-Out of the Mechanical Motion

Due to the multimode character of the light field inside the HCPCF, analysing the light leaving the HCPCF is sufficient to infer the three-dimensional motion of the particle. The following chapter is oriented on the supplementary information of [62] and on the master thesis of Julian Fesel [46].

The read-out of the particle COM motion inside the HCPCF is based on interference between scattered light from the particle and the fundamental trapping mode LP_{01}. It provides position information of the particle with respect to the intensity maximum it is trapped in. The levitated particle is treated as dipole scatterer E_{dp} which is preeminently excited by the fundamental trapping mode LP_{01}, see chapter 3.1.2.

The read-out along the axial (z) direction relies on interference between light scattered off the particle into the symmetric fundamental mode LP_{01} and the trapping laser. The radial read-out (x, y) relies on interference between light scattered off the particle into the anti-symmetric higher order mode LP_{11} and the trapping laser.

Let us assume a particle trapped in an intensity maximum inside the HCPCF is displaced by δz along the fiber axis. The mode overlap between scattered light from the particle and the fundamental fiber mode LP_{01} is $\eta_{01}(\delta z) = \langle \mathrm{LP}_{01}, E_{\mathrm{dp}}(\delta z)\rangle = |\eta_{01}|e^{i\beta_{01}2\delta z + i\phi_{01}}$ with $|\eta_{01}|$ and ϕ_{01} constants independent of δz. The values of $|\eta_{01}|$ and ϕ_{01} are computed numerically [46]. Both fields, the trapping mode and the light scattered off the particle into the fundamental mode interfere and their intensity is given by

$$\begin{aligned} I_z(\delta z) &= \frac{\varepsilon_0 c}{2}\left|\mathrm{LP}_{01} + \eta_{01}(\delta z)\mathrm{LP}_{01}\right|^2 \\ &= I_0\Big[1 + |\eta_{01}|^2 + 2|\eta_{01}|\cos\Big([\beta_{01} - k]\delta z + \phi_{01}\Big)\Big] \\ &\approx I_0 - 2I_0|\eta_{01}|(\beta_{01} - k)\delta z \end{aligned} \tag{2.15}$$

with I_0 the intensity of the trapping mode. The second order term can be neglected as the scattering off the particle into the fundamental HCPCF mode LP_{01} is an inefficient process ($O(|\eta_{01}|^2) \ll 1$). With the combination of the numerically computed scattering phase of $\phi_{01} \approx \pi/2$ and for small displacements δz of the particle the cosine function can be approximated with its argument. The first term of equation 2.15 is constant and the second term is proportional to the axial displacement δz of the nanoparticle. The implementation of our detection scheme, see chapter 2.2.2, allows subtraction of the constant term and the resulting detector signal is solely proportional to the axial displacement δz.

The radial read-out relies on interference between light scattered from the particle into the higher order mode LP_{11} and the trapping mode. A particle moving radially by δx (without loss of generality we assume motion along the x-axis, the treatment in the orthogonal direction y is analogous) excites the anti-symmetric mode LP_{11} with a position dependent phase and amplitude, i.e., $\eta_{11}(\delta x) = \langle \mathrm{LP}_{11}, E_{\mathrm{dp}}(\delta x)\rangle = E_{01}(a+ib)\delta x$. The values for a, b are computed numerically [46]. The interference between light scattered off the particle into the higher order mode LP_{11} and the fundamental trapping mode is

$$\begin{aligned} I_x(\delta x) &= \frac{\varepsilon_0 c}{2}|\mathrm{LP}_{01} + \eta_{11}\mathrm{LP}_{11}|^2 \\ &= I_0 + |\eta_{11}|^2\varepsilon_{11}^2 + \varepsilon_0 c E_{01}\Re\{\eta_{11}^* e^{i\Delta\beta z}\} \\ &\approx I_0 + \varepsilon_{01}\varepsilon_{11}\varepsilon_0 c E_{01}^2|\eta_{11}|\sin(\Delta\beta z + \phi_{11})\delta x \end{aligned} \tag{2.16}$$

with $|\eta_{11}| = \sqrt{a^2+b^2}$ and $\phi_{11} = \arctan(b/a)$. It is important to note that the first term $I_0 = \varepsilon_0 c/2 E_0^2\varepsilon_{01}^2(x,y)$ is symmetric with respect to the y-axis ($x = 0$) and the second term $\propto \varepsilon_{01}(x,y)\varepsilon_{11}(x,y)$ is anti-symmetric with respect to the y-axis ($x = 0$). Here, $\varepsilon_{01}(x,y)$ and $\varepsilon_{11}(x,y)$ are the radial field distributions of the LP_{01} and LP_{11} mode, see chapter 2.1.1. Detection with a single photodiode, which corresponds to an integration over the intensity I_x along the x-axis, would only result in the optical power of the fundamental trapping mode $P_0 \propto I_0$. The contribution of the second term of equation 2.16 vanishes due to its anti-symmetry with respect to $x = 0$. Therefore, a split-detection scheme is used, see chapter 2.2.2. In a split-detection scheme, half of the intensity of I_x is measured with one photodiode and the other half with a second photodiode (equally split around $x = 0$). The difference signal between both diodes is proportional to

$$S_x \propto \int_{-x_0}^{0} dA\ I_x - \int_{0}^{x_0} dA\ I_x \propto P_0|\eta_{11}|\sin(\Delta\beta z + \phi_{11})\delta x \tag{2.17}$$

with x_0 the extent of the photodiodes. Here, the symmetric part of I_x vanishes and the anti-symmetric part survives, resulting in a signal directly proportional to the radial particle motion δx. Note that the signal also depends on the axial particle position z. In a consequence, the sensitivity of the radial read-out is modulated with the wavelength of the interference pattern between fundamental and higher order mode $2\pi/\Delta\beta \approx 208\ \mu\mathrm{m}$.

2.2. Experimental Setup and Procedures

In this chapter the experimental setup and experimental procedures are explained in detail. It is separated into optical and vacuum setup, loading and trapping particles, moving particles through the fiber and how the HCPCF is prepared and mounted into vacuum chambers.

2.2.1. Optical Trapping Setup

The optical trapping setup can be divided into two parts, the beam preparation and the optical trapping part. The beam preparation part is sketched in figure 2.14.

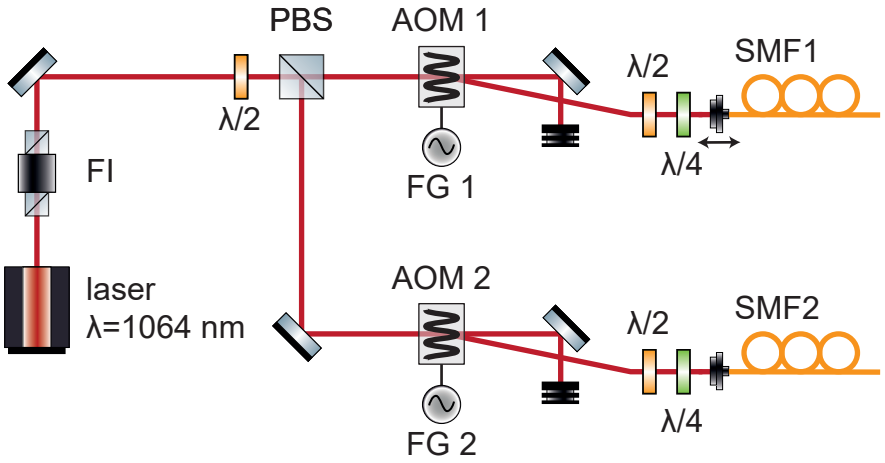

Figure 2.14.: A laser with $\lambda = 1064$ nm is split into two parts with a combination of half waveplate ($\lambda/2$) and a polarizing beamsplitter (PBS). Each beam propagates through an acousto-optical modulator (AOM1 and AOM2) which is driven with a frequency generator (FG1 and FG2). The deflected light leaving the AOMs is coupled into a single mode fiber (SMF1 and SMF2) and the light that is not deflected is sent onto a beam dump. Before each SMF, a combination of half waveplate ($\lambda/2$) and quarter waveplate ($\lambda/4$) compensates polarization rotations introduced by the SMF. A Faraday isolator (FI) protects the laser from back-reflections.

The output of a Coherent Verdi IR laser with a center wavelength of $\lambda = 1064$ nm is split into two parts with a combination of half waveplate ($\lambda/2$) and a polarizing beamsplitter (PBS). The beam in transmission of the PBS is referred

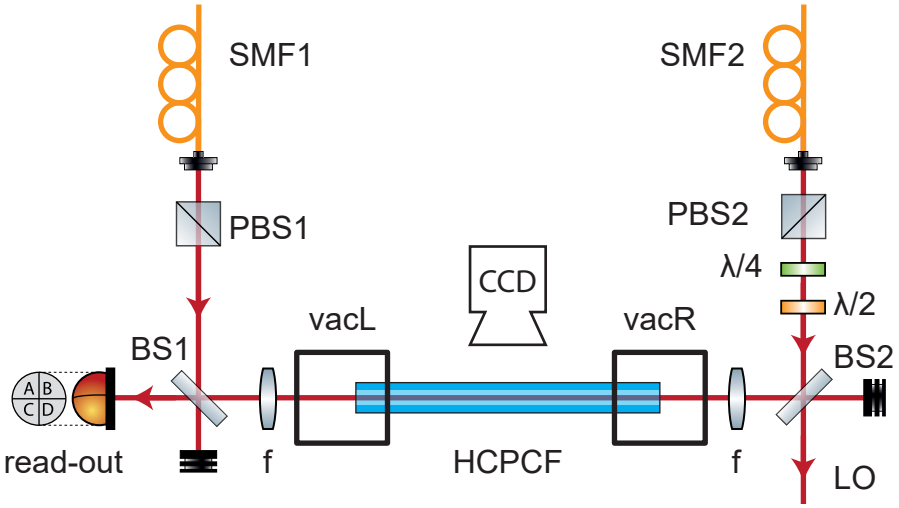

Figure 2.15.: Light from the beam preparation setup is guided through single mode fibers (SMF1 and SMF2) to the optical trapping part. The HCPCF is mounted into two vacuum chambers (vacL and vacR) and can be imaged with a laterally mounted camera (CCD). The laser light exiting the SMF is reflected on two 90:10 beamsplitter (BS1,BS2) and coupled into the HCPCF with lenses outside the vacuum chambers. 10% of the light transmitted on BS1 is sent to the read-out part of the experiment and 10% of the light transmitted on BS2 is used as local oscillator (LO) for the read-out. The half ($\lambda/2$) and quarter ($\lambda/4$) waveplate are aligned to compensate the polarization rotation introduced by the HCPCF.

to as counterclockwise propagating beam (CCPB) and the beam in reflection as clockwise propagating beam (CPB). Each, CCPB and CPB propagate through an ATM-804DA6M acousto-optical modulator (AOM) from IntraAction Corp. The AOM deflects the incident light depending on its drive frequency and amplitude. They are typically driven with a 80 MHz tone and a power on the order of 1 W (FG1 and FG2). In the first realization of the experiment a DFE-804A4 dual channel frequency synthesizer from IntraAction Corp. was used as AOM driver, which was recently exchanged with a Moglabs XRF421. The new driver allows for finer tuning of the drive frequency compared to the DEF-804A4, which was limited to 10 kHz steps. The first diffraction order of the AOM is coupled into a single mode fiber (SMF) and the zeroth diffraction order is dumped into a beam block. The maximum deflection efficiency of the AOM is between 70-80 %. The single mode fibers are used as a mode cleaner

since the mode leaving the laser is slightly elliptical. In order to compensate rotations of the polarization by the SMFs, a combination of half and quarter waveplate is placed before each fiber input. A Faraday isolator (FI) protects the laser from back-reflections.

The main trapping setup is shown in figure 2.15. A HC1060 HCPCF from NKT Photonics is mounted between two vacuum chambers (vacL and vacR). The CCPB (light leaving SMF1) and the CPB (light leaving SMF2) are coupled into the HCPCF with two lenses ($f = 13$ mm) outside of the vacuum chamber. Two polarizing beamsplitters (PBS1, PBS2) in combination with the waveplates before the SMFs, see figure 2.14, are used to define the polarization state of light leaving the SMFs. The HCPCF, as any non-polarization maintaining fiber, rotates the polarization state which is compensated for by another pair of half ($\lambda/2$) and quarter ($\lambda/4$) waveplate between the HCPCF and PBS2. Roughly 10% of the CPB is transmitted at the 90:10 beamsplitter (BS2, Thorlabs: BSX11) and coupled into another SMF (not shown in figure 2.15). This fraction of light serves as local oscillator (LO) for the read-out of the particle motion. Another 10% of the CPB after propagation through the HCPCF is transmitted at the 90:10 beamsplitter (BS1, Thorlabs: BSX17) and is used as signal beam for the particle read-out. A Playstation Eye camera (CCD), with the infrared filter removed, is used for particle monitoring from the side. A typical CCD image can be seen in figure 2.23.

2.2.2. Optical Read-Out

This chapter describes the experimental implementation of the read-out of the COM motion. Figure 2.16 gives an overview of the read-out including the z read-out. 10% of the scattered light from the nanoparticle and the CPB trapping beam are transmitted at the beamsplitter (BS1), which is referred to as signal beam. The signal beam is split into three parts with two polarizing beamsplitters (PBS1 and PBS2) and two half waveplates ($\lambda/2$). The light reflected at PBS1 is used for detection of the nanoparticle along the y-axis, the light reflected at PBS2 is used for detection along the x-axis and the light transmitted at PBS2 is used for detection along the z-axis.

As already described in chapter 2.1.5, the axial read-out relies on interference between light scattered from the particle into the mode LP_{01} and the trapping mode. The signal beam consists of a constant intensity I_0 contribution from the trapping laser and an alternating contribution of the particle motion, see equation 2.15, which is coupled into a single mode fiber (SMF). A balanced, amplified photodetector (Thorlabs: PDB420C-AC) is used for detection of the light. The detector has two photodiodes, a difference circuit and an amplifier. It subtracts the photocurrents from each diode and returns an amplified output

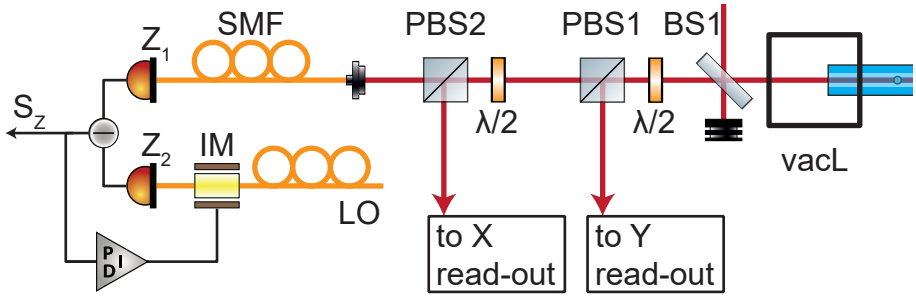

Figure 2.16.: 10% of the light leaving the HCPCF is transmitted at the beamsplitter (BS1). It is split into three beams with two polarizing beamsplitters (PBS1 and PBS1) and two half wave-plates ($\lambda/2$). Light transmitted at PBS1 and PBS2 is used for radial motion detection. The transmitted light is coupled into a single mode fiber (SMF) and sent to the photo diode Z_1. The local oscillator (LO, see figure 2.15) propagates via an in-fiber intensity modulator (IM) to the photodiode Z_2. The difference signal between Z_1 and Z_2 is used as error signal for a PID feedback loop and feed back to the IM. The feedback loop stabilizes the difference signal between Z_1 and Z_2 to be zero on a timescale much slower than the axial mechanical frequency Ω_z. The difference signal S_z is proportional to the particle motion along the fiber axis.

voltage proportional to the difference current. The detector also provides a monitor output for each diode. The signal beam from the SMF is sent onto photodiode Z_1 and light from the local oscillator (LO, see figure 2.15), passing an in-fiber intensity modulator (IM, Jenoptik: AM1060HF) is sent onto the photodiode Z_2. The difference between the two monitor outputs is computed with an analog differential amplifier circuit, see appendix A.5, and used as error signal for a feedback loop. A PID controller (Toptica: PID110) and the IM are used to stabilize the power difference between both diodes to zero with a bandwidth between 0 and ≈ 5 kHz, not to interfere with the particle dynamics at higher frequencies $\Omega_z \gg 100$ kHz. In doing so, the contribution from the constant intensity I_0 detected by photodiode Z_1 is eliminated and the resulting difference signal S_z is solely proportional to the axial particle motion, see equation 2.15. Note that the anti-symmetric contribution in the signal beam (due to the radial particle motion) vanishes due to its detection with a single photodiode.

The read-out of the two radial directions x and y relies on interference between scattered light from the nanoparticle into the mode LP_{11} and the

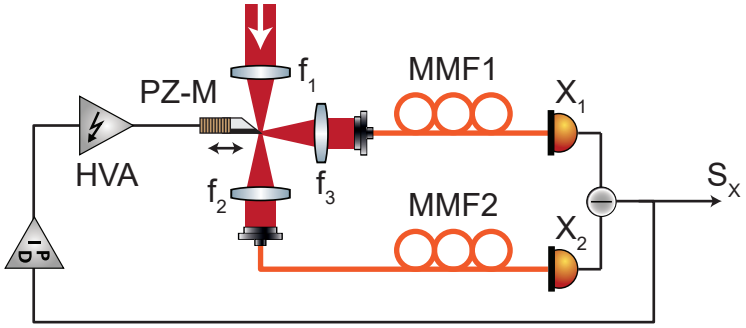

Figure 2.17.: Signal light (light reflected from PBS1 or PBS2, see figure 2.16) is focused with the a lens (f_1) onto a knife edge on a piezo stack (PZ-M) such that half of the impinging light is reflected and half of the light is transmitted. The reflected light is collimated with a lens (f_3) and coupled into a multimode fiber (MMF1). The light transmitted is collimated with a lens (f_2) and coupled into another multimode fiber (MMF2). The multimode fibers go onto the photodiodes X_1 and X_2. The difference signal between both diodes is used as error signal for a PID feedback controller. The output of the PID is amplified to high voltages (HVA) and sent to the piezo stack with the knife edge. The feedback loop controls the position of the knife edge such that the optical power reaching the photodiode X_1 is the same as on X_2. Their difference signal is proportional to the particle displacement along the x-direction.

trapping mode. The read-out architecture along x- and y-direction is identical up to a rotation by 90° around the fiber axis. Figure 2.17 displays a sketch of a radial read-out. Light reflected from PBS1 (for the y read-out) or PBS2 (for x read-out), see figure 2.16, is focused with a $f_1 = 25$ mm lens onto a knife edge glued onto a piezo stack (PZ-M). The knife edge consists of a piece of a Indium Gallium Arsenide which has high reflectivity for the wavelength $\lambda = 1064$ nm. The plate is positioned in such a way that the impinging mode is cut in half, such that one half of the mode is reflected and collimated by the lens $f_3 = 25$ mm and the remaining half is transmitted and collimated by the lens $f_2 = 25$ mm. Both collimated beams are coupled into multimode fibers (MMF1 and MMF2) and sent onto a balanced, amplified photodetector (Thorlabs: PDB420-C). The difference between the two monitor outputs is computed with an analog differential amplifier circuit (see appendix A.5) and used as error signal. A PID controller (Toptica: PID110) including a high-voltage amplifier (HVA) generates a control signal acting on the piezo stack.

The feedback loop stabilizes the knife-edge in such a way that half of the mode is detected by detector X_1 and the other half by detector X_2. This ensures that equation 2.17 is always fulfilled and, therefore, that the detector signal S_x is proportional to the radial displacement. The bandwidth of the feedback loop is between 0 and ≈ 1 kHz, far away from the radial particle motion $\Omega_x > 10$ kHz, not to tamper with the detection of the COM motion. If the knife position deviates from the center of the mode, the sensitivity of the read-out decreases. Note that the symmetric modulation of the signal beam, caused by the axial particle motion, vanishes due to the split-detection scheme.

Calibration of the Read-out

As described in chapter 2.1.5, the detector signal (along axial direction for example, the same procedure is applied to the two radial directions) $S_z = \sqrt{c_z} z$ is proportional to the particle displacement z. The proportionality constant

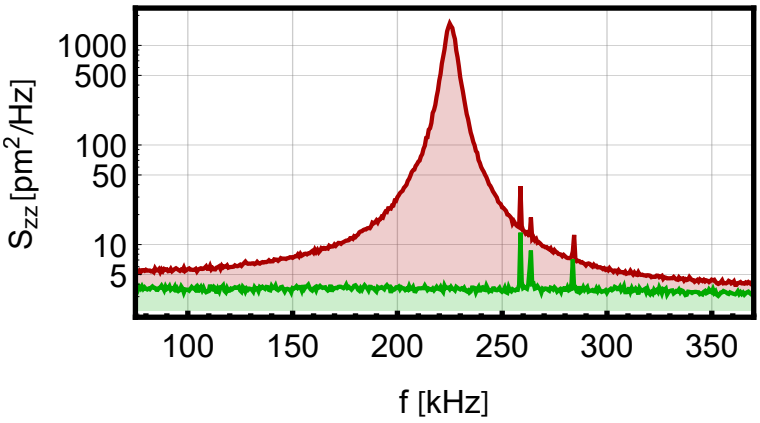

Figure 2.18.: S_{zz} noise-power spectrum of a 387 nm diameter silica particle trapped at a pressure of $p = 4.9$ mbar [62]. The red curve is the signal with particle and the green curve is the background signal without particle. The noise floor of the background sets the position sensitivity of 2×10^{-12} m/$\sqrt{\text{Hz}}$ for the read-out.

c_z depends on the mode overlap η_{01} between light scattered off the trapped particle and the fundamental trapping mode, see chapter 2.1.5, which contains the polarizability α of the particle. The polarizability is different for each individual particle (scatter in size and dielectric constant) and therefore it is not possible to calibrate the read-out independent of the levitated particle. Without any external control of the system and at a pressure of $p = 4.9$ mbar for example, where coupling to the thermal environment is dominant [14, 59], the particle COM motion is in thermal equilibrium with the environment

$m\Omega_z^2\langle z^2\rangle = k_B T_0$. A measured spectrum from the axial read-out is shown in figure 2.18. The green trace represents the noise floor of the read-out (recorded without a particle in the trap) and the red trace represents the particle signal in thermal equilibrium. The area of of a recorded signal with particle in the trap $\langle S_z^2\rangle = \int d\omega S_z(\omega)$ at thermal equilibrium can be used to calculate the proportionality c_z. In a first step, the contribution of the background $\langle S_{z,B}^2\rangle$ (green area) is subtracted from the particle signal $\langle S_{z,P}^2\rangle$ (red area) $\langle S_z^2\rangle = \langle S_{z,P}^2\rangle - \langle S_{z,B}^2\rangle$. In a second step the equipartition theorem is used to calculate the proportionality constant

$$c_z = \frac{k_B T_0}{m\Omega_z^2\langle S_z^2\rangle}.$$

With c_z, the voltage signal from the detection can be converted into a particle displacement $z = \sqrt{c_z} S_z$. The sensitivity of the read-out (the smallest detectable signal) is given by 2×10^{-12} m/$\sqrt{\text{Hz}}$ for the axial direction and better than 40×10^{-12} m/$\sqrt{\text{Hz}}$ for the radial directions for a levitated particle with a diameter of $d = 387$ nm.

Figure 2.19 shows a measured and calibrated three-dimensional trajectory of a trapped particle inside the HCPCF.

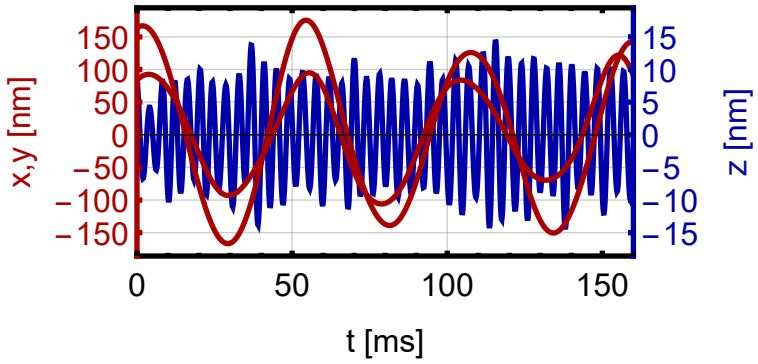

Figure 2.19.: Measured three-dimensional trajectory of a levitated particle inside a HCPCF at a pressure of $p = 0.3$ mbar [62]. The data is bandpass filtered (between 5-50 kHz along x, y and between 50-500 kHz along z) to eliminate technical noise.

2.2.3. Vacuum Setup

The vacuum system in the HCPCF experiment is designed to have independent pressure control and pressure monitoring in each vacuum chamber. Figure 2.20 schematically shows the vacuum setup combined with the basic optics setup.

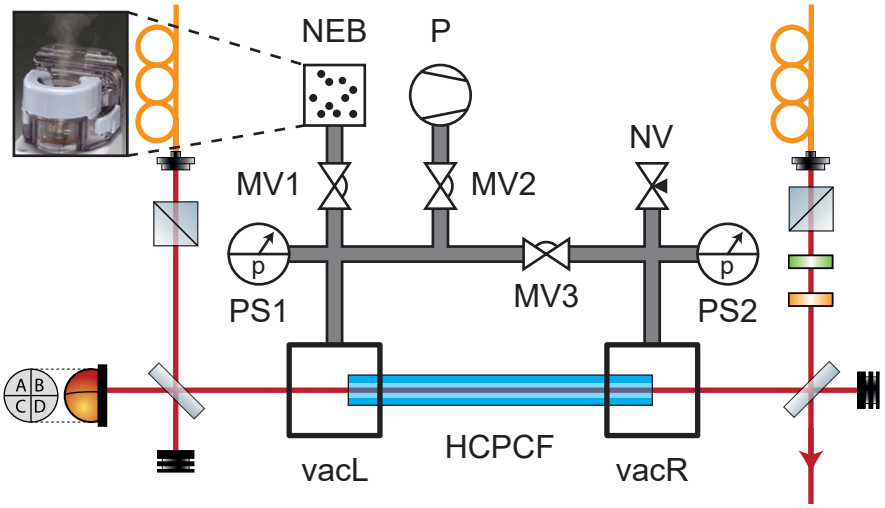

Figure 2.20.: A vacuum pump (P) is connected to the left vacuum chamber (vacL) and to the right vacuum chamber (vacR) and each connection can be individually controlled with membrane valves (MV2 for vacL, MV2 and MV3 for vacR). Each vacuum chamber is directly connected to a pressure sensor (PS1 and PS2). A source for airborne nanoparticles (NEB) is connected to the left chamber via a membrane valve (MV1). A needle valve (NV) is connected to the outside at $p = 1000$ mbar and is used to have a controlled influx of air.

A dry scroll pump (P, Edwards: nXDS6i) is connected to the left vacuum chamber (vacL) and to the right vacuum chamber (vacR). The membrane valves MV2 and MV3 allow individual evacuation of one or the other vacuum chamber. MV2 is an automatic valve that can be computer controlled for automatized measurements. A needle valve (NV) connects the vacuum system to the outside at room pressure. It can be used to have a controlled influx of air into vacR. Each chamber is connected to a vacuum gauge (PS1 and PS2 respectively, MKS: Baratron 622C13MDE) to measure the individual chamber pressure. A source of airborne nanoparticles (NEB) is connected via a membrane valve (MV1) to the left vacuum chamber. More details about loading particles and the source can be found in chapter 2.2.5.

2.2.4. Fiber Cutting and Fiber Mounting

The handling of a HCPCF is in general similar to standard optical fibers. Some of the differences were already mentioned in my Master thesis [63]. Here I want to present a more complete picture on preparation and mounting of

HCPCFs for optical levitation. There is a useful application note [64] from NKT photonics on HCPCF handling. In this chapter the steps from initial cutting (or cleaving) of a HCPCF until mounting it into an optical levitation experiment are described.

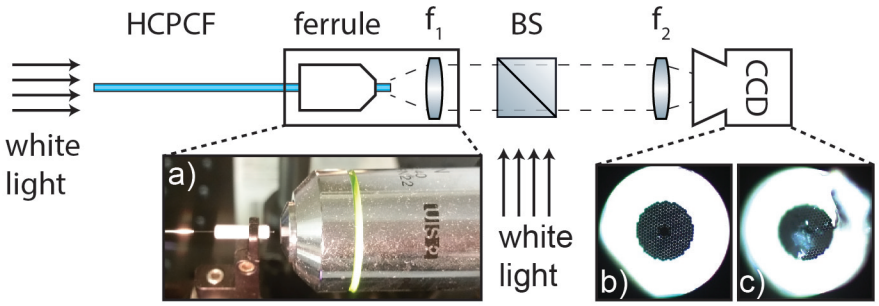

Figure 2.21.: HCPCF cleave and inspection station: The HCPCF is inserted into a fiber optical ceramic ferrule in which the fiber can be cleaved and visually inspected (inset a)). The station consists of a simple optical microscope with an objective lens f_1 and a condenser lens f_2. A CCD at the end of the microscope is used for imaging of the HCPCF end. An image of a HCPCF front surface after successful cleaving is shown in inset b) and for a bad cleave with fractures in the photonic crystal area in inset c). The fiber is illuminated either via the beamsplitter (BS) and a white light source, or through the HCPCF with a white light source.

In the experiments reported within this thesis the typical length of a HCPCF is on the order of $l_0 \approx 20$ cm. The acrylic cladding protecting the HCPCF can be removed with a sharp knife (a surgical scalpel or razor blade for example). One end of the HCPCF is inserted into a fiber optic ceramic ferrule (Thorlabs: CF126) and clamped into a self-made cleaving and inspection station. It allows cleaving and inspection of a HCPCF inside a ceramic ferrule which is also used for mounting the fiber later on.

A schematic of the station is shown in figure 2.21. A fiber optical ferrule is fixed and aligned to a simple optical microscope with an objective lens (f_1, Nikon: Plan N 40x) and a standard achromatic lens with a focal length of $f_2 = 30$ mm as condenser. The camera (CCD, Sony: Playstation Eye, all original optics and filters removed) in combination with the microscope is used to visualize the surface of the HCPCF. The insets b) and c) of figure 2.21 show typical images recorded with the CCD. Part b) shows the surface of a successfully cleaved HCPCF compared to part c), a bad cleave with fractures in the

photonic crystal area. The fiber is illuminated either with white light entering through the beamsplitter (BS) or with white light through the HCPCF.

The HCPCF is inserted into the ferrule until roughly 1 mm of fiber is standing out of the other side of the ferrule. A ceramic knife (Thorlabs: S90R) is used to gently carve the HCPCF along the front surface of the ferrule, perpendicular to the fiber axis. The front surface of the ferrule can be used as a guide for the knife. Then, the fiber is moved a few millimeters towards the microscope objective and a few taps on the fiber tip with the knife breaks the fiber along the carve. The microscope is used to visually inspect the surface immediately after cleaving. If the fiber has a smooth surface without fractures, the cleave is good. Otherwise the procedure of carving and breaking needs to be repeated. The same procedure is applied to the remaining fiber end.

The next step is controlling the transmission performance of the fiber. The easiest way to measure the transmission is butt-coupling the HCPCF to a SMF. The fiber optical ceramic ferrule is compatible with standard fiber components, such as the ceramic split mating sleeve (Thorlabs: ADAF1) and a FC/PC connected SM980-5.8-125 single mode fiber (from Thorlabs). The HCPCF inside the ferrule is inserted into the mating sleeve from one side and the FC/PC fiber from the other side. By rotating the FC/PC fiber the coupling can be optimized. As the mode field diameter of the HC1060 HCPCF and the SM980-5.8-12 singlemode fiber match, a coupling efficiency $> 90\%$ is easy to achieve. If the coupling efficiency is less than 90% a new piece of HCPCF should be prepared.

After cleaving and transmission testing, the HCPCF is mounted into the vacuum chambers. Figure 2.22 a) shows a picture of one vacuum chamber with a mounted HCPCF. Figure 2.22 b) shows a SolidWorks drawing of the vacuum chamber in a sectional view. The HCPCF and the fiber optical ferrule are inserted into a hole on the backside of the vacuum chamber. The hole is half a millimeter wider than the outer diameter of the ferrule to simplify the insertion process. The chamber is designed to be compatible with the Thorlabs cage system (Thorlabs: 30 mm Cage System). The HCPCF with the ferrule are centered with respect to the cage system axis. The lens used for coupling light into the HCPCF is outside the vacuum chamber and mounted inside the cage system. The fiber should stand 1-2 mm out of the ferrule to provide optical access with a camera from the side window and be within the focal length of the lens outside. After insertion, a thin layer of glue (two component Epoxy or Torr Seal) is put on the fiber-ferrule interface and on the ferrule-chamber interface. After hardening of the glue the same procedure is applied to the second fiber end and the second vacuum chamber. Once both fiber ends are mounted light can be coupled into the HCPCF. With a good cleave

a coupling efficiency around 80% can be achieved from a free space Gaussian mode into the HCPCF.

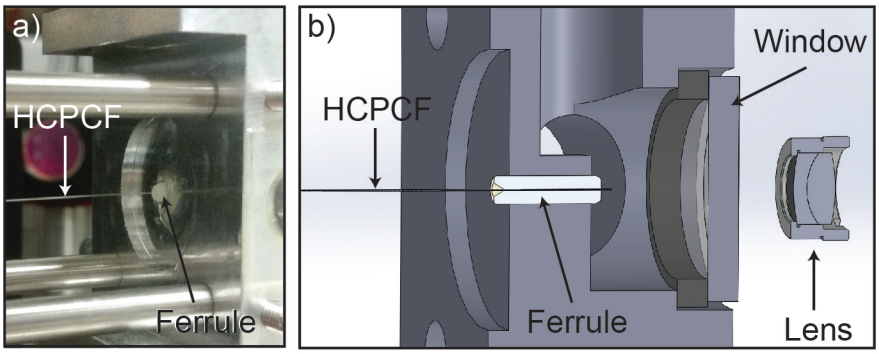

Figure 2.22.: a) Photograph of one vacuum chamber with a HCPCF inside a ferrule mounted. b) Sectional view of the vacuum chamber. The hole on the backside matches the outer diameter of the fiber optical ferrule. Once fiber and ferrule are inserted the chamber is sealed with glue. The lens outside the chamber is used to couple light through the optical window into the HCPCF.

2.2.5. Particle Loading and Trapping

The experiments described in this thesis primarily use plain silica particles with a diameter of either 387 nm (MicroParticles GmbH: SiO_2-F-0.4) or 969 nm (MicroParticles: GmbH SiO_2-F-1.0) for levitation. They are delivered in water with a mass concentration of 10%. The particle-water solution is further diluted with isopropanol to a final mass-solvent concentration of 10^{-7}. A medical asthma spray (Omron: MicroAir U22) is used to spray the solution into air or a nitrogen atmosphere in a closed container. The isopropanol and water will quickly evaporate and airborne silica particles are left. This approach was first reported in [65]. A typical loading protocol is as follow. The left vacuum chamber (vacL) is evacuated to a pressure of $p \approx 1$ mbar and the membrane valves MV1, MV2 and MV3 are closed (see figure 2.20). Then, valve MV1 is gently opened to have a steady flow of particles from the container (NEB) into the left vacuum chamber. At the same time the transport mechanism of the HCPCF trap, see chapter 2.2.6, is switched on. If a particle comes close to the HCPCF entrance it might be trapped and transported towards vacR. The CCD camera mounted laterally with respect to the fiber (see figure 2.15) detects if a particle enters the field of view and stops the transport mechanism.

Once a particle is trapped inside the HCPCF valve MV1 is closed. Typically a particle will be trapped within 10 s.

2.2.6. Optical Conveyor Belt

This chapter is based on [62]. The optical trap is built up of a standing wave of the counterpropagating modes inside the HCPCF. The standing wave is used as an optical conveyor belt for levitated particles, which has already been demonstrated in free space, both, for individual atoms [66] and macroscopic dielectric particles [53]. Those approaches are limited to distances on the order of the Rayleigh length of the laser beam. In our case, in contrast, transport is limited by the fiber length which can be several meters. An optical conveyor belt for micrometer sized particles inside a HCPCF has also been demonstrated [13], in which a feedback loop optimizes a higher order mode with a spatial light modulator. The method presented here is technologically simpler as only a frequency change of one laser beam is required.

The dominant part of the intensity distribution inside the HCPCF is given by the term proportional to P_{01} of equation 2.4. It can be rewritten as

$$\begin{aligned} I &\propto |e^{i(\beta_{01}z-2\pi\nu t)} + e^{i(\beta_{01}(z-z_0)+2\pi(\nu-\Delta)t}|^2 \\ &= 2\cos^2\left[\beta_{01}(z-\frac{z_0}{2})+\pi\Delta t\right] \end{aligned} \tag{2.18}$$

with $\nu = c/\lambda$ the frequency of the laser, z_0 a change of optical path length in one arm of the setup and Δ a relative detuning between CPB and CCPB. The end of the single mode fiber SMF1 (see figure 2.14) is mounted on a translation stage and introduces the change in optical path length z_0 to vary the distance between the end of SMF1 and the surface of PBS. The relative detuning Δ is introduced by driving AOM1 (see figure 2.14) with a frequency $\nu = 80$ MHz and AOM2 with a frequency $\nu = 80$ MHz $+ \Delta$. A particle will always be trapped in an intensity maximum of the standing wave, i.e. at a localization where $\beta_{01}(z - \frac{z_0}{2}) + \pi\Delta t = 0$. For $\Delta = 0$ the position of the trapped particle is $z = z_0/2$ which means by varying the path length difference the position of a trapped particle can be changed. The velocity of an intensity maximum and therefore the velocity of a particle trapped is $v = dz/dt = \pi\Delta/\beta_{01} \approx \Delta\ \lambda/2$. By detuning one laser beam by Δ the standing wave starts moving and acts as a conveyor belt for trapped particles.

In figure 2.23 ten consecutive pictures of a particle transported through the HCPCF with the optical conveyor belt (detuning $\Delta = 20$ kHz) are shown. The position of the particle is calibrated with the manual positioning stage. By calculating the velocity of the particle with the known frame rate of the

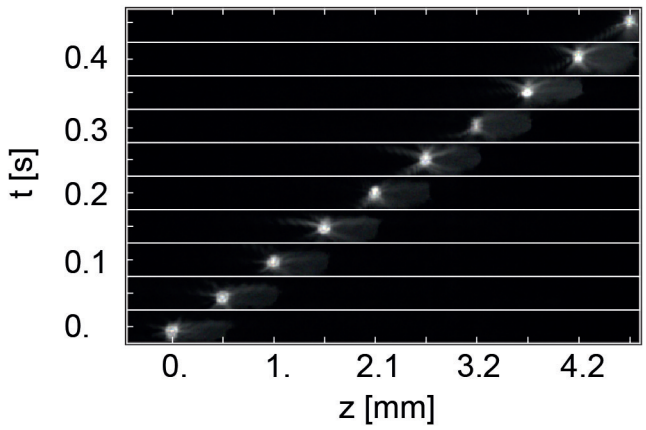

Figure 2.23.: Ten consecutive images of a 387 nm diameter particle at different positions (x-axis) and different times (y-axis) while transported with a detuning $\Delta = 20$ kHz inside the HCPCF [62].

camera we find $v = (10.66 \pm 0.06)$ mm/s, which agrees with the theoretical predicted value of $v = 10.64$ mm/s.

2.2.7. Optical Trap Characterization

This chapter presents characterisation measurements of the HCPCF trap. A set of power-, position- and pressure dependent measurements confirms the theoretical descriptions from chapter 2.1.

Power and Pressure Dependence

Two intrinsic parameters of a damped harmonic oscillator are the damping coefficient and the oscillation frequency. Together with the mass and the temperature of the force noise the system is uniquely defined, see chapter 2.1.4. In optically levitated systems the oscillation frequency Ω_m as well as the damping γ_p can be controlled by the optical trapping power and the target pressure, respectively. Figure 2.24 a) shows a mechanical damping measurement as a function of the pressure in the vacuum system $\gamma_\mathrm{p}(p)$ and a fit according to equation 2.11. Figure 2.24 b) shows a measurement of the frequency $\Omega_\mathrm{x}(P)$ as a function of the trapping power P. The solid line is a fit to equation 2.9. For each power or pressure setting a spectrum was recorded and fitted to the noise-power spectrum (see equation 2.13) with γ_p and Ω_m as free fit parameters. For both measurements the same silica particle with a diameter of $d = 387$ nm was used. The mechanical frequency has a square-root dependence on the trapping power. The mechanical damping depends linearly on the pressure, which is

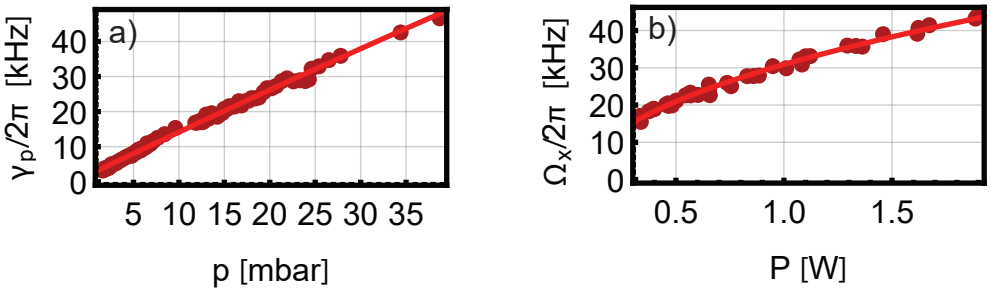

Figure 2.24.: a) Measurement of the damping γ_p (points) and fit (solid line) for different pressures p. b) Measurement of the mechanical frequency Ω_x (points) and fit (solid line) for different trapping powers P.

expected in the regime where the mean free path of air molecules is larger than the particle diameter, see equation 2.12.

Frequency z-Position Dependence

The appearance of multiple modes inside the HCPCF causes deviations from a free space standing wave, see chapter 2.1.1 and chapter 2.1.3. The intensity of individual anti-nodes is modulated and since the mechanical frequency depends on the intensity, this effect can be used to map out the interference pattern. A measurement of the mechanical frequency Ω_z for varying z-positions inside the HCPCF is shown in figure 2.25. A levitated particle is moved to different positions inside the HCPCF with the conveyor belt and at each position the mechanical frequency is measured (blue dots). The solid line is a sinusoidal fit

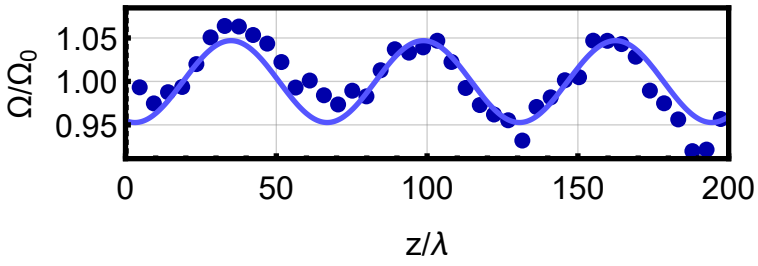

Figure 2.25.: Position dependent axial frequency: The normalized axial mechanical frequency along the fiber axis is measured (dots) and fitted to an interference pattern between fundamental and higher order fiber mode (solid line).

to the data with amplitude and frequency as free fit parameters. The wave-

length of the frequency modulation is defined by half the beating wavelength $\pi/\Delta\beta$ between mode LP_{01} and mode LP_{11}, see chapter 2.1.3. The value of $\Delta\beta$ can be used to estimate the HCPCF core radius r_{co}, according to equation 2.2. For this particular HCPCF the fit results in a core radius of $r_{co} = 4.2 \pm 0.1$ μm. The amplitude of the fit can be used to infer the power ratio between mode LP_{01} and mode LP_{11} and results in a ratio of $P_{11}/P_{01} \approx 0.1$.

Frequency x, y-Position Dependence

The same mechanisms that leads to a modulation of the axial mechanical frequency modulates the two radial frequencies, too. Figure 2.26 displays a

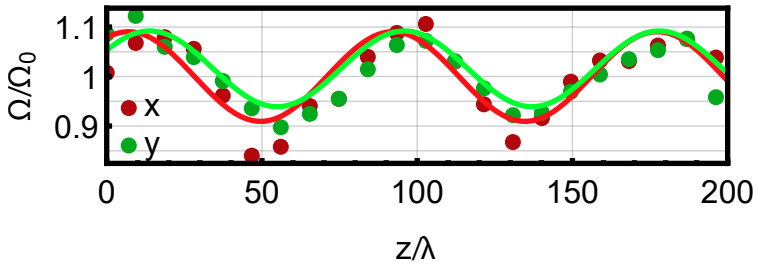

Figure 2.26.: Position dependent radial frequencies: The normalized radial frequencies along x- (red points) and y-direction (green points) are measured as a function of z-position inside the HCPCF. The solid lines represent fits to the interference pattern between fundamental and higher order mode.

measurement of the radial mechanical frequency as a function of position. It is in close analogy to the measurement in the previous chapter, see figure 2.25.

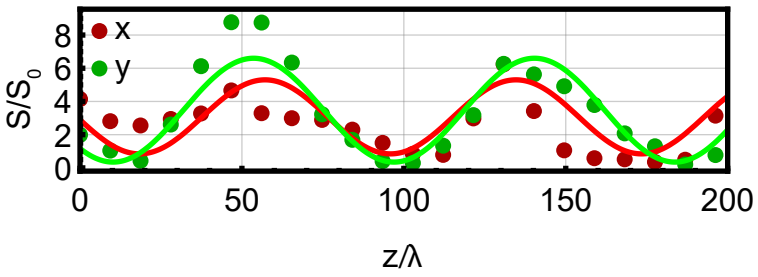

Figure 2.27.: Position dependent radial read-out sensitivity: Due to the interference between fundamental mode LP_{01} and higher order mode LP_{11}, the sensitivity is modulated with a wavelength of $\pi/\Delta\beta$. The solid lines are fits to the interference pattern.

In contrast to the axial direction, the sensitivity of the radial read-out is modulated with a wavelength of $2\pi/\Delta\beta$, see equation 2.17. A measurement of the sensitivity S is shown in figure 2.27. The sensitivity is defined as ratio between maximum of the mechanical spectrum S_{xx} and the noise floor of the spectrum. Note that this definition of the sensitivity is proportional to the absolute value of the read-out and hence, has the same wavelength as the frequency modulation.

2.3. Linear Feedback Cooling Inside a Hollow Core Fiber

Feedback control is a universal technique to stabilize a system parameter based on a measurement of the system. In the context of mechanical oscillators, feedback stabilization turned out to be extremely useful, for example in atomic force microscopy [67] and in gravitational wave detection [68]. It is also successfully applied to cool the center of mass (COM) motion of mechanical oscillators [69–71]. For levitated systems Ashkin and Dziedzic applied feedback stabilisation techniques already in 1977 to stabilize a levitated particle in high vacuum [72] and Li et al. used feedback to cool the COM motion of a levitated microsphere to ≈ 1.5 mK at room temperature [73].

The term linear feedback cooling is used to emphasize the difference to parametric feedback cooling. Linear feedback applies a force proportional to the displacement (or velocity or a combination of both) to the particle whereas in parametric feedback cooling the spring constant is modulated proportional to a product of displacement and velocity, see chapter 3.1.3. As a direct consequence, the modulation happens at the mechanical frequency in linear feedback and in the parametric case at twice the mechanical frequency. Beside the pioneering work of Ashkin and Li, linear feedback techniques are commonly applied to levitated systems, for example in the search of milli-charged particles [74], ultra-sensitive force measurements [75, 76], or pressure sensing [62].

2.3.1. Theory of Direct Feedback Cooling

In this chapter feedback cooling is explained with a general, system independent feedback force $F_{\mathrm{fb}} = m\Pi f(x)$. The feedback force is chosen to be proportional to the particle mass and a parameter Π which describes the physical implementation of the feedback. Most importantly, the feedback force is a linear function in the displacement variable x of the oscillator. The function $f(x)$ is implemented by, for example, a PID controller connected to the read-out of the experiment. The additional feedback force modifies the equation of motion to

$$\ddot{x} + \gamma_{\mathrm{p}}\dot{x} + \Omega_{\mathrm{m}}^2 x = \frac{F_{\mathrm{th}} + F_{\mathrm{fb}}}{m}. \tag{2.19}$$

High-Q Approximation

If the mechanical quality factor is large $Q = \Omega_{\mathrm{m}}/\gamma_{\mathrm{p}} \gg 1$, the displacement on short timescales $t < 1/\gamma_{\mathrm{p}}$ is well approximated with a sinusoidal function.

For a feedback function $f(x) = x_{t-\tau}$ which only introduces a delay τ between displacement and feedback force, i.e.

$$\begin{aligned} x_{t-\tau} &\approx x_0 \sin\left[\Omega_\mathrm{m}(t-\tau)\right] \\ &= x_t \cos\phi - \dot{x}_t \frac{\sin\phi}{\Omega_\mathrm{m}} \end{aligned}$$

with $\phi = \Omega_\mathrm{m}\tau$ the phase shift corresponding to the delay τ, the equation of motion can be rewritten as

$$\ddot{x}_t + (\gamma_\mathrm{p} + \frac{\Pi \sin\phi}{\Omega_\mathrm{m}})\dot{x}_t + (\Omega_\mathrm{m}^2 - \Pi\cos\phi)x_t = \frac{F_\mathrm{th}}{m}. \tag{2.20}$$

The term $\gamma_\mathrm{fb} = \Pi \sin\phi/\Omega_\mathrm{m}$ can be identified as additional damping and $\Omega_\mathrm{fb}^2 = \Pi\cos\phi$ as optical spring introduced by feedback control. Note that both effects can be controlled with the delay $\phi = \Omega_\mathrm{m}\tau$. For a value of $\Omega_\mathrm{m}\tau = \pi/2$ for example, the optical spring term vanishes and the only effect of the feedback is additional damping.

Derivative Feedback

Instead of introducing a time delay τ, the feedback function can also be chosen to be the derivative of the displacement, i.e. $f(x) = \dot{x}$. The feedback force becomes $F_\mathrm{fb} = m\Pi\dot{x}$ and the equation of motion is given by

$$\ddot{x}_t + (\gamma_\mathrm{p} + \Pi)\dot{x}_t + \Omega_\mathrm{m}^2 x_t = \frac{F_\mathrm{th}}{m}.$$

This corresponds to equation 2.20 for $\phi = \Omega_\mathrm{m}\tau = \pi/2$ in which the optical spring vanishes and the damping is maximal.

Effective Mode Temperature

The noise power spectral density corresponding to equation 2.20 is

$$\begin{aligned} S_\mathrm{xx}(\omega) &= \frac{2k_B T_0 \gamma_\mathrm{p}}{\pi m} \frac{1}{(\Omega^2 + \Omega_\mathrm{fb}^2 - \omega^2)^2 + (\gamma_\mathrm{p} + \gamma_\mathrm{fb})^2\omega^2} \\ &= \frac{2k_\mathrm{B} T_0 \gamma_\mathrm{p}}{\pi m} \frac{1}{\left(\Omega_\mathrm{eff}^2 - \omega^2\right)^2 + \gamma_\mathrm{eff}^2\omega^2} \end{aligned} \tag{2.21}$$

with $\Omega_\mathrm{eff}^2 = \Omega_\mathrm{m}^2 + \Omega_\mathrm{fb}^2$ the effective mechanical frequency and $\gamma_\mathrm{eff} = \gamma_\mathrm{p} + \gamma_\mathrm{fb}$ the effective mechanical damping caused by feedback control. Integration of the

spectrum

$$\begin{aligned}\langle x^2\rangle &= \int_0^\infty d\omega\ S_{\mathrm{xx}}(\omega) \\ &= \int_0^\infty d\omega\ \frac{2k_\mathrm{B}T_0\gamma_\mathrm{p}}{\pi m}\frac{1}{\left(\Omega_\mathrm{eff}^2-\omega^2\right)^2+\gamma_\mathrm{eff}^2\omega^2} \\ &= \frac{k_\mathrm{B}T_0}{m}\frac{\gamma_\mathrm{p}}{\Omega_\mathrm{eff}^2\gamma_\mathrm{eff}}\end{aligned}$$

and application of the equipartition theorem $m\Omega_\mathrm{eff}^2\langle x^2\rangle = k_B T_\mathrm{eff}$ allows the definition of an effective mode temperature

$$\begin{aligned}T_\mathrm{eff} &= \frac{m\Omega_\mathrm{eff}^2\langle x^2\rangle}{k_\mathrm{B}} \\ &= T_0\frac{\gamma_\mathrm{p}}{\gamma_\mathrm{eff}} = T_0\frac{\gamma_\mathrm{p}}{\gamma_\mathrm{p}+\gamma_\mathrm{fb}}.\end{aligned} \tag{2.22}$$

Note that for feedback control being switched off the effective mode temperature is $T_\mathrm{eff} = T_0$, the temperature of the environment. For $\gamma_\mathrm{fb} > 0$ the effective temperature $T_\mathrm{eff} < T_0$ is smaller than the environmental temperature. Hence, introducing damping via feedback is equivalent to operating at a colder environmental temperature and therefore also called cold damping. For low pressures and efficient feedback cooling $\gamma_\mathrm{eff} = \gamma_\mathrm{p} + \gamma_\mathrm{fb} \approx \gamma_\mathrm{fb}$. The effective temperature can then be simplified to $T_\mathrm{eff} \approx T_0\gamma_\mathrm{p}/\gamma_\mathrm{fb}$ and becomes inversely proportional to the damping introduced by feedback cooling.

2.3.2. Optical Axial Feedback Cooling

This chapter is based on [62]. Feedback control along the fiber axis (z-direction) is implemented via radiation pressure of an additional feedback laser. Figure 2.28 shows the additions to the optical setup for axial feedback control. A laser with $\lambda = 1064$ nm and power P_fb for feedback cooling is superimposed with the CCPB at PBS1. It is orthogonally polarized and shifted in frequency with respect to the trapping laser to avoid interference. The feedback laser propagates through the HCPCF and pushes the particle away from the intensity maximum of the standing wave due to radiation pressure $\vec{F}_\mathrm{scatt} = \sigma_\mathrm{scatt}/cI\vec{e}_z$.

For a constant power P_fb a trapped particle has a new equilibrium position z_0 where $F_\mathrm{scatt}(z_0) = F_\mathrm{grad}(z_0)$. An increase or decrease of the feedback laser power P_fb either pushes the particle further away from z_0 or the gradient force

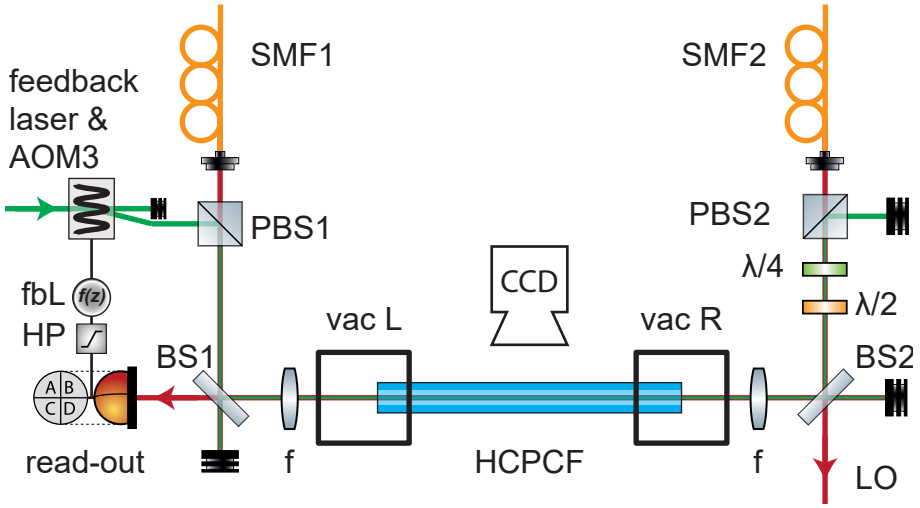

Figure 2.28.: A laser for feedback cooling (green line) is superimposed with the counterclockwise propagating trapping laser at a polarizing beamsplitter (PBS1). A feedback logic (fbL) and a highpass filter (HP) process the axial read-out signal of the particle. It is transduced to an intensity modulation of the feedback laser via the acousto-optical modulator (AOM3).

pulls the particle back towards intensity maximum of the standing wave. The feedback laser is modulated with a ATM-804DA6M acousto-optical modulator from IntraAction Corp (AOM3) which is driven by a MOD80 frequency source from AA Opto-Electronic .

The voltage signal of the detector is highpass filtered (HP) with an analog filter (corner frequency $\nu_{\mathrm{hp}} \approx 50$ kHz), see appendix A.2, to suppress unwanted low frequency noise. The feedback logic (fbL) converts the read-out signal into a modulation signal sent to AOM3. It consist of three parts: a phase shifter, a variable gain amplifier and a controlled switch. The variable gain amplifier and the phase shifter are described in appendix A.3 and appendix A.4, respectively. The phase shifter delays the signal by $t = \pi/(2\Omega_{\mathrm{z}})$, effectively resulting in a velocity feedback in the high-Q limit. The variable amplifier is used to adjust the amplitude of the feedback signal. The controlled switch (Mini-Circuits: ZASWA-2-50DR+) is used to enable or disable the feedback control with a TTL signal. Alternatively, the feedback logic is replaced with a field programmable gate array (FPGA, National Instruments: PXIe-7965 in combination with a NI-5781 transceiver module). The FPGA is used to delay the signal by $\tau = \pi/(2\Omega_{\mathrm{z}})$ in the same way as the phase shifter analog circuit.

A measurement of feedback cooling is shown in figure 2.29. A silica particle

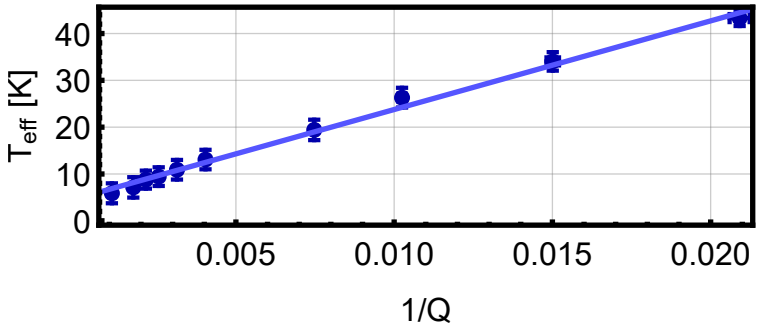

Figure 2.29.: Axial radiation pressure based feedback cooling: Effective axial COM temperature as a function of inverse mechanical quality factor $1/Q \propto p$. A silica particle with a diameter of 387 nm is feedback cooled via radiation pressure [62]. The lowest mode temperature achieved is $T_{\mathrm{eff}} = (4.83 \pm 0.28)$ K. The solid line is a linear fit to the data points.

with a diameter of 387 nm is trapped inside the HCPCF and feedback control is switched on. The delay of the feedback logic is chosen for optimal feedback cooling. The effective mode temperature is measured as a function of the pressure p, which effectively changes the mechanical quality factor $Q = \Omega_{\mathrm{m}}/\gamma_{\mathrm{p}}$. The solid line is a fit to equation 2.22 confirming the pressure dependence of linear feedback cooling $T_{\mathrm{eff}} \approx T_0\gamma_{\mathrm{p}}/\gamma_{\mathrm{fb}} \propto p$. The minimal effective mode temperature achieved is $T_{\mathrm{eff}} = (4.83 \pm 0.28)$ K, which is limited by particle loss from the trap at lower pressures. For the future, implementation of three-dimensional feedback cooling should prevent particle loss and allow cooling to much lower temperatures.

2.3.3. Electrical Radial Feedback Cooling on Charged Particles

The one-dimensional feedback cooling scheme needs to be extended to be able to levitate in vacuum. One approach is electrical feedback along the radial directions of motion (x and y).

Here we are using the fact that some of the particles from the nebulizer are charged during the loading process. Alternatively there are techniques available to control the charges on a levitated particle [74, 77]. Such a charged particle is used for a proof-of-principle demonstration of electrical feedback cooling. A plate capacitor around the HCPCF applies an electrostatic force on a particle $F_{\mathrm{el}} = qU/d$ (q: charges on the particle, d: distance between the plates, U: voltage applied to the capacitor). As above, for the optical case, the

electrical force is modulated proportional to the velocity of the particle and hence cooling the COM motion.

The experimental modifications to the setup are shown in figure 2.30 Two

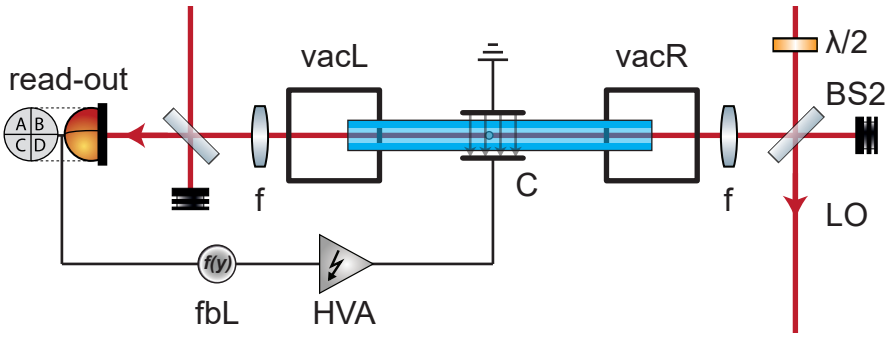

Figure 2.30.: A plate capacitor (C) is mounted around the HCPCF and a particle is positioned between the plates, where the electric field is homogeneous. The y read-out signal (which is parallel with respect to the electric field of C) is sent to a feedback logic (fbL) and is amplified with a high-voltage amplifier (HVA). The signal of the amplifier is connected to the capacitor modulating the electrostatic force on the particle.

copper plates (roughly 1 cm x 1 cm) separated by $d_C = 2$ mm are mounted around the HCPCF. A particle trapped inside the HCPCF is moved between the two plates with the optical conveyor belt. The capacitor is aligned such that the homogeneous electric field lines are parallel with the y-COM motion. One way of aligning is driving the capacitor and hence the particle COM with a sinusoidal tone. If the driving frequency appears in both, the x and y read-out, the capacitor needs to be rotated until only one direction is addressed.

The feedback logic consists of an analog derivative circuit, see appendix A.6 in combination with a variable gain amplifier, see appendix A.3. The y read-out is connected to the feedback logic generating the feedback signal $f(y) \propto g_y \dot{y}$ with g_y the gain of the variable amplifier circuit. The signal is further amplified with a high voltage amplifier (HVA, Trek: PZD350A-1-H-CE) which is connected to the copper plates.

A measurement of the effective temperature T_{eff} for a particle of diameter $a = 387$ nm at a pressure of $p = 2.9$ mbar is shown in figure 2.31 for different feedback gains g_y. Feedback cooling of the COM motion is clearly observable and a reduction to $T_y \approx 150$ K from room temperature was possible. The solid line is a fit to the effective mode temperature, see equation 2.22, with the feedback gain g_y as free fit parameter.

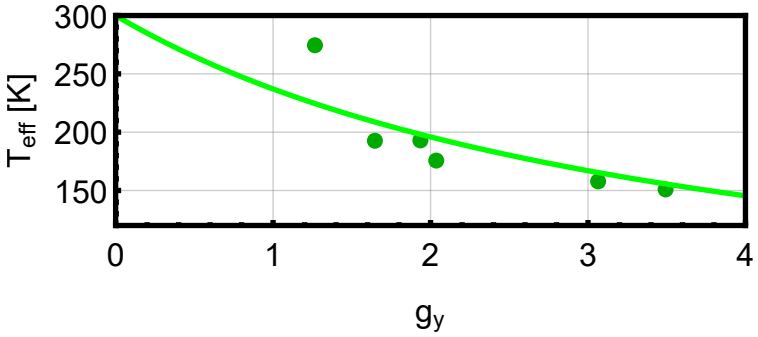

Figure 2.31.: Radial electric feedback cooling: Effective mode temperature of the y-COM motion versus feedback gain g_y. The solid line is a fit to the effective mode temperature.

The scheme could be extended to two dimensions. Instead of a plate capacitor one would need four rods around the HCPCF, arranged like a Paul trap. Relying on metal rods outside the fiber and not covering the entire fiber (the two vacuum chambers are in the way, for example) constrains the range in which feedback cooling could be applied and hence the range where particles could be trapped in high vacuum. A possible solution would be metal rods incorporated in the photonic crystal of the fiber, as already demonstrated for solid core photonic crystal fibers [78]. With this technology available, radial electric feedback cooling could be applied over the full extend of the fiber. In combination with the radiation pressure based feedback cooling described in the previous chapter levitation in high vacuum would be feasible.

2.4. The Hollow Core Trap as Source for Ultra-High Vacuum Experiments

Cavity optomechanics with levitated nanoparticles is a promising platform for fundamental tests of physics. Proposals range from ground state cooling of the COM motion to macroscopic superposition states of motion [5, 16, 79–81]. Several of them require extreme experimental conditions, particularly ultra-high vacuum levels $p \lesssim 10^{-10}$ mbar to isolate the system sufficiently well from the environment [81, 82]. While free particles in ultra-high vacuum have been prepared via laser ablation [83, 84], reliably trapping nanoparticles inside ultra-high vacuum, to perform this type of experiments, is still an outstanding challenge.

By loading a particle into the optical trap, neither the vacuum system nor parts of the experiment inside the vacuum chamber should be contaminated with residual particles or solvent. A standard approach to load particles into optical traps uses ultrasonic nebulizers [65], as described in chapter 2.2.5 and chapter 3.3.4. Optical mirrors inside the vacuum chamber, used for a high-finesse cavity for example, are susceptible to a high particle concentration in the solvent. We found experimentally that a mass concentration of 10^{-4} (particles to solvent ratio) degraded the finesse of our cavity from $\mathcal{F} = 200,000$ to $\mathcal{F} = 40,000$ (during a single loading attempt). However, a combination of optical tweezer and high-finesse cavity as proposed in [16], requires this concentration to load particles into the tweezer trap, see chapter 3.3.4.

Some protocols involving multiple modes inside the optomechanical cavity require a particle levitated at a specific position inside the cavity field, for example [5, 85]. By sucking a cloud of particles into the vacuum chamber or by shaking particles off a piezo [2] or by laser ablation [83, 84], there is no control over which trapping site will be occupied. Therefore a loading mechanism with a controllable location of delivery is mandatory.

2.4.1. HCPCF as Particle Source

The HCPCF experiment as source for particles has the potential to comply the previously mentioned requirements. The basic design is shown in figure 2.32. The left vacuum chamber (vacL) contains an ultrasonic nebulizer source (NEB) and the right vacuum chamber (vacR) contains the target experiment. In our case the target experiment is a high-finesse Fabry-Pérot cavity which is used to control the COM motion of a levitated nanoparticle. The HCPCF spatially separates the contaminating solvents from the cavity and is used to deliver particles on demand with the optical conveyor belt to a well controlled

position, i.e. the exit of the hollow core fiber.

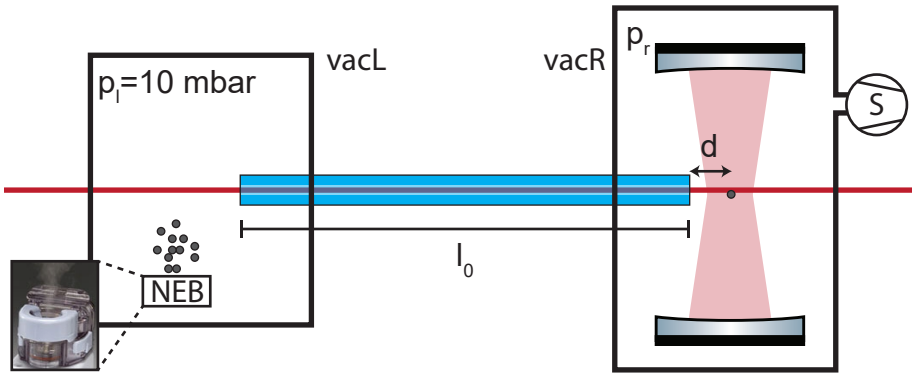

Figure 2.32.: A HCPCF of length l_0 connects the left vacuum chamber (vacL) containing an ultrasonic nebulizer operating at $p = 10$ mbar with the right vacuum chamber (vacR) containing a high-finesse Fabry-Pérot cavity. VacR is also connected to a pump with a volume pumping rate S. The optical conveyor belt is use to transport a nanoparticle from vacL on demand into the cavity mode in vacR at ultra-high vacuum.

The HCPCF is not only the loading channel for particles into ultra-high vacuum, it is also a leak which connects the chamber at ultra-high vacuum with a higher pressure region. In the context of vacuum technology the conductance C, the inverse of the flow resistance, is used to quantify the flow properties of a pipe. The conductance C of the HCPCF is the sum of its conductance for free molecular flow (the flow characteristics at the ultra-high vacuum side p_r) and its conductance for continuous flow (the flow characteristics at the high pressure side p_l) [86] and is given by

$$C = \frac{\pi v_{\text{gas}}}{12}\frac{d_{\text{co}}^3}{l_0} + \frac{\pi}{256\eta}\frac{d_{\text{co}}^4}{l_0}(p_l + p_r) \tag{2.23}$$

with v_{gas} the mean thermal velocity of gas molecules, η the gas viscosity, d_{co} the core diameter of the HCPCF and l_0 the length of the HCPCF. The volume flow from the left into the right vacuum chamber is $q_{pV} = C(p_r - p_l)$. The right vacuum chamber is connected to a vacuum pump with an effective volume pumping rate S. An equilibrium between gas influx through the HCPCF and evacuation via the pump is reached if

$$\Delta p C = p_r S \tag{2.24}$$

with $\Delta p = p_l - p_r$.

Ermolov et al. [33] showed for HCPCFs with a core diameter of $d_{\mathrm{co}} = 30\ \mu$m and a length $l_0 = 0.3$ m that eight orders of magnitude in pressure can be bridged. In their experiment one fiber end was at room pressure $p_l = 10^3$ mbar and a pump with $S = 225$ l/s was connected to the right vacuum chamber. A final pressure of $p_r = 8 \times 10^{-6}$ mbar was reached, consistent with equation 2.23 .

In our scenario, the left vacuum chamber will be held at $p_l = 10$ mbar for initial particle loading from an ultrasonic nebulizer source. The conductance C is dominated by the free molecular flow term proportional to $\propto d_{\mathrm{co}}^3$ and by the inverse proportional scaling with the fiber length l_0. Using the HC-1060 (the fiber used for the experiments presented in this thesis) HCPCF with a core diameter of $d_{\mathrm{co}} = 10\mu$m reduces the conductance by a factor of 80 and increasing the length to $l_0 = 1$ m further decreases the conductance by another factor of three, compared to the findings in [33]. In combination with a stronger vacuum pump (pumping speed of $S = 790$ l/s, Pfeiffer HiPace800 for example) the pressure in the right vacuum chamber can be reduced by eleven orders of magnitude and a desired ultra-high vacuum level of $p_r = 10^{-10}$ mbar can be reached.

A particle can be trapped in the left chamber at ambient pressures, transported with the conveyor belt into ultra-high vacuum and handed over into the mode of an optical cavity. Particles can be routinely trapped within 10 s on the high pressure side. Transport over $l_0 = 1$ m of fiber with a detuning of $\Delta = 40$ kHz takes 50 s (for this detuning, all acceleration and deceleration effects due to starting and stopping of the conveyor belt are negligible). In summary, a single particle could be delivered on demand into ultra-high vacuum to a well-defined position and without contaminants from a nebulizer source at a total time of $t = 60$ s. Currently, the system is limited by particle loss from the trap below a pressure of $p \approx 0.1$ mbar. Once the HCPCF is equipped with three-dimensional feedback cooling it is expected to levitate particles in ultra-high vacuum, making the system a promising candidate for loading.

2.4.2. Trapping in Front of the Hollow Core Fiber

One very important parameter for the HCPCF trap as particle source is the distance d a particle can be levitated away from the fiber entrance. As indicated in figure 2.32 the distance d needs to be bigger than the waist of the cavity mode. If the fiber clips the cavity mode it will decrease its finesse and therefore limit the performance of the optomechanical system. In our current cavity system the optical losses of both cavity mirrors are 10ppm (parts per million, limited only by the design transmission of the coatings). The pres-

ence of the HCPCF should not increase losses significantly. The situation is

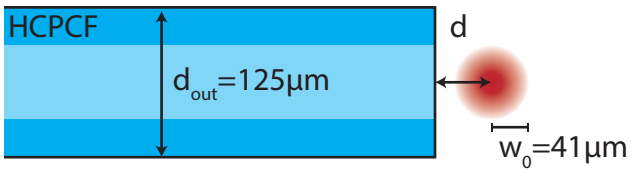

Figure 2.33.: A HCPCF with an outer diameter of $d_{\text{out}} = 125\ \mu$m is positioned in the vicinity of a TEM00 mode (red area, cross-sectional view, waist: $w_0 = 41\ \mu$m) with a distance of d between them.

illustrated in more detail in figure 2.33. A HCPCF with an outer diameter of $d_{\text{out}} = 125\ \mu$m (the outer diameter of a HC1060) is positioned in the vicinity of a TEM00 mode (indicated by the red area). In our cavity experiment the waist of this mode is $w_0 = 41\ \mu$m. The clipping losses η_{clip} due to the presence of the HCPCF are computed as one minus the ratio between the integral

$$a(p) = \frac{1}{\sqrt{2\pi w_0^2}} \int_p^\infty dx\ e^{-\frac{x^2}{2w_0^2}} \tag{2.25}$$

of the radial cavity field with the fiber at a position $p = d$ and without the fiber present $p = -\infty$. For a distance of $p = 5w_0$ between cavity mode and HCPCF the additional clipping losses are $\eta_{\text{clipp}} = 1 - a(5w_0)/a(\infty) = 0.3$ ppm. If the clipping losses should not exceed a value of $\eta_{\text{clipp}} < 10$ ppm, we find numerically that the minimal distance between fiber and cavity needs to be at least $d > 4.25w_0$.

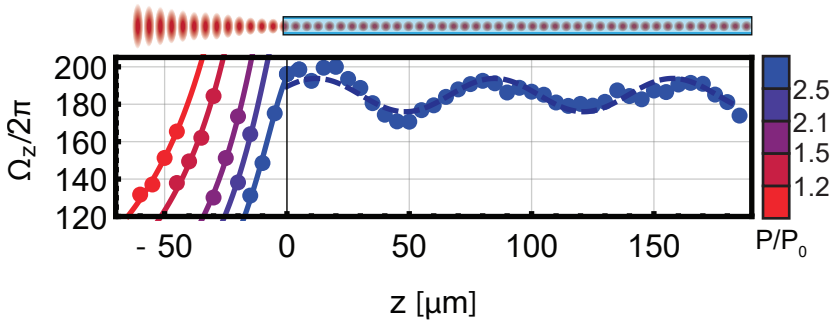

Figure 2.34.: Axial mechanical frequency Ω_z of a particle trapped inside ($z > 0$) and in front ($z < 0$) of the HCPCF [62].

Figure 2.34 shows measurements of a particle being trapped in front of the HCPCF. A particle at a pressure of $p = 0.2$ mbar is positioned inside the

HCPCF ($z > 0$) and in front of the HCPCF ($z < 0$). The modulation of the mechanical frequency Ω_z inside the fiber is due to the beating between fundamental trapping and the first higher order mode inside the HCPCF. The mode in front of the fiber is expanding with a Gaussian envelope. Therefore the trap frequency and the confinement decrease for increasing distance from the fiber tip. In order to keep the particle trapped, the power of the trapping laser is increased (color coding). At a pressure $p = 0.2$ mbar and without feedback

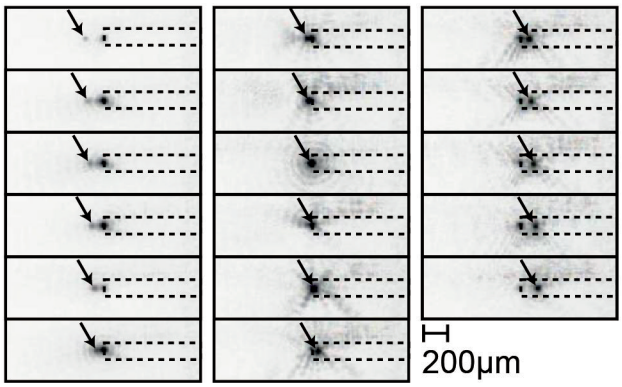

Figure 2.35.: A series (from top left to bottom right) of color-inverted pictures of a 387 nm diameter particle (black arrows) for positions outside and inside the HCPCF (black dashed lines) [62]. The black dot at the fiber entrance is scattered light from the HCPCF tip. The further outside of the HCPCF the less light is scattered from the nano-particle which is due to the diverging laser beam.

cooling the particle could be trapped up to a distance of $d = 65$ μm in front of the fiber. At higher pressures ($p \approx 5$ mbar) the distance can be increased, even without power compensation, to 160 μm away from the HCPCF tip. Figure 2.35 shows a selection of pictures from the particle at different positions inside and outside of the HCPCF in false coloring.

Once the HCPCF fiber experiment is equipped with three-dimensional feedback cooling we assume that a particle can be stably levitated in front of the HCPCF at any pressure and at distances $d \approx 200$ μm $= 5w_0$, which would allow safe loading of our levitated cavity optomechanics experiment [14].

2.4.3. All-Fiber Optical Trap

In the previous chapter the potential of the HCPCF setup as source for levitation experiments was introduced. In the scenario shown in figure 2.32 the

HCPCF needs to be aligned with respect to the cavity to hand over a particle. The current HCPCF setup trap does not offer such positioning capabilities. In this chapter I will present an all-fiber based optical trap that overcomes this deficiency and report the current progress. Some results were carried out in the Bachelor project of Christian Siegele [87].

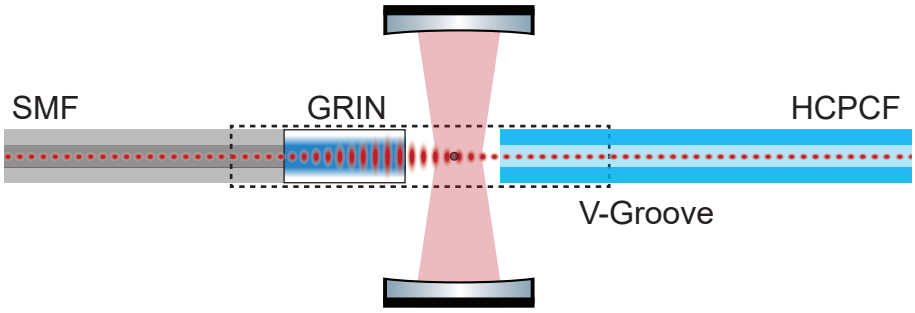

Figure 2.36.: A single mode fiber (SMF) with a grin lens (GRIN) is used to build a standing wave trap with a hollow core fiber (HCPCF). The SMF, GRIN and HCPCF are all fixed to the same v-groove (dashed black line) and can be moved around together.

The free space optics used to couple light into the HCPCF make the trap immobile. If one end of a HCPCF were to be aligned to a cavity mode, the optics used for coupling would require simultaneous movement. This can be avoided with the design shown in figure 2.36. A single mode fiber (SMF) with a gradient index lens (GRIN) is used to couple light into a HCPCF fiber. A GRIN lens is a cylindrical piece of glass which has radial variation of the refractive index. With the proper length, such a glass cylinder acts as focusing lens. The GRIN lens has a flat surface and therefore, it can be easily fused to an optical fiber. The SMF, the GRIN lens and the HCPCF fiber are glued to a v-groove such that all three components are quasi-monolithic. The second end of the HCPCF is mounted into a vacuum chamber as described in chapter 2.2.4 which is connected to an ultrasonic nebulizer. By coupling light into the HCPCF and into the SMF an optical conveyor belt trap is formed and can be used to transport particles towards the GRIN interface. The v-groove is mounted on a three-dimensional translation stage and the laser light for trapping and transport of particles arrives via flexible fibers. The combined system can easily be moved around with the translation stage and no realignment of optics is required. This is ideal to align a particle trapped in front of a HCPCF to a cavity mode.

On of the main results of [87] was the characterisation of the SMF-GRIN-HCPCF interface. For a distance of 1.3 mm between SMF (Thorlabs: SMPF0210)

and GRIN (Thorlabs: GRIN2910) the beam from the SMF is focused at $d = 1.3$mm behind the GRIN with a beam waist of $w_0 = 3.75$ μm, hence matching the mode field diameter of the HCPCF (Thorlabs: HC1060). That means that the combination of GRIN and SMF can be used to launch light into a HCPCF without any additional optics. The GRIN and SMF were held together inside a glass sleeve (Thorlabs: 51-2800-1800) while the HCPCF was glued into a ceramic ferrule (Thorlabs: CF270-10) with the same outer diameter as the glass sleeve. The SMF and GRIN combination on one side an the HCPCF with ceramic ferrule on the other side were glued into a self-made v-groove. A prototype is shown in figure 2.37 in combination with four snap-

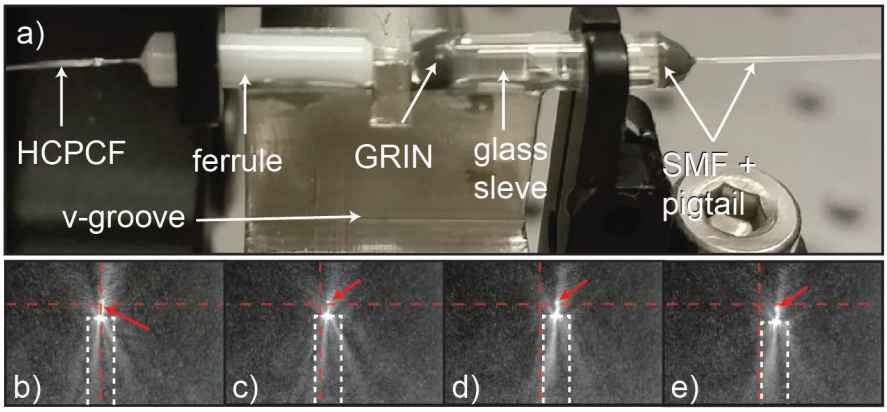

Figure 2.37.: Photograph a) shows a prototype of the all-fiber optical trap [87]. A hollow core fiber (HCPCF) inside a ceramic ferrule on one side and a GRIN lens and a pigtailed SMF inside a glass sleeve on the other side are both glued on the same home-made v-groove. b)-e) Photographs of a particle (red arrow) levitated in front of a HCPCF (indicated by white, dashed line). The all-fiber trap including particle is first moved to the right b)-d) and then towards the bottom d)-e). The red dashed cross marks the initial particle position.

shots of a video in which a particle is trapped inside the all-fiber trap and moved around with a three-dimensional positioner (picture b)-e)). More details on the experimental setup, alignment procedures and construction of the prototypes can be found in [87].

The current bottleneck of the all-fiber optical trap is the long-term stability. It seems that over the course of a few days the alignment between SMF and HCPCF deteriorates and the coupling efficiency from SMF to HCPCF reduces (from initially 80%) to zero. The best explanation so far is that the GRIN lens absorbs light (the manufacturer specifies 90% transmission), thermally expands

and reduces the coupling from SMF to HCPCF. The thermal expansion might deform the glue between GRIN and glass sleeve in an irreversible way until no light is coupled and trapping is not possible anymore.

The next step is improving the mechanical mounting of the three components with respect to each other. A first step is getting customized grin lenses already fused onto a SMF and with better transmission at the trapping wavelength. Also, a custom GRIN lens which is already fused on the SMF simplifies the alignment procedure.

2.5. A Nanomechanical Oscillator as Pressure Sensor

The application described in the previous chapter, namely loading particles into vacuum with a HCPCF, comes with an obvious question. If the left vacuum chamber holding the HCPCF is at moderate pressure (for initial particle trapping) and the right vacuum chamber holding the other end of the fiber (containing a sophisticated levitation apparatus) at ultra-high vacuum - what is the pressure profile along the fiber? It turns out that this problem, flow through a straight pipe, is non-trivial and requires modelling with the non-linear Boltzmann equation. The Boltzmann equation is a fundamental model for rarefied gas dynamics forming the basis for the kinetic theory of gases [88–90]. The Boltzmann equation also applies to electron transport in solids and plasmas, to neutron transport in nuclear reactors, to photon transport in superfluids [90] and is relevant for vacuum technology, chemical apparatuses, spaceship construction, gas-surface interaction and fabrication of semiconductors and microelectronics [91, 92].

The figure of merit to characterize flow through a pipe is the Knudsen number $\mathrm{Kn} = \Lambda_{\mathrm{free}}/d$. It compares the mean free path of gas molecules Λ_{free} with the relevant geometry d of the system, in this case the hollow core radius r_{co}. Continuous flow occurs for Knudsen numbers below $\mathrm{Kn} < 0.01$ if the mean free path of gas molecules is much shorter than the fiber core. Continuous flow in a pipe can be further separated into laminar and turbulent flow, depending on the Reynolds number $\mathrm{Re} = 8.41 \times 10^{-1} Q/d$ (this is a specific expression for air flow through round pipes [86] with Q the volume flow rate and d the pipe diameter). Up to values of $\mathrm{Re} < 1200$ the flow will be laminar [86]. In the extreme case of $p_r = 1000$ mbar and $p_l = 0$ mbar, the Reynolds number for flow through a $l_0 = 0.1$ m long HCPCF is $\mathrm{Re} = 0.07 \ll 1200$, placing the system well into the laminar regime. Here, the gas is described as fluid, molecules mainly interact with each other and have less frequent interactions with the fiber walls. The pressure profile in the laminar continuum regime for

Figure 2.38.: The HCPCF connects the left vacuum chamber at pressure p_l with the right vacuum chamber at pressure $p_r > p_l$.

the situation shown in figure 2.38 is given by [86]

$$p(z) = \sqrt{p_l^2 + \frac{z}{l_0}(p_r^2 - p_l^2)}. \tag{2.26}$$

with z the coordinate along the tube and l_0 the length of the tube.

Free molecular flow occurs for a Knudsen number Kn > 1 where the mean free path is much larger than the fiber core. In this regime gas molecules hardly interact with each other and the dynamics are governed by collisions with the walls. The pressure profile along the tube in the free molecular regime is given by [86]

$$p(z) = p_l + z\frac{p_r - p_l}{l_0}. \tag{2.27}$$

In the HCPCF experiment the Knudsen number can be controlled via the pressure in each vacuum chamber. For a pressure $p_l \approx 0.1$ mbar in the left vacuum chamber and $p_r = 1000$ mbar in the right vacuum chamber the Knudsen number lies between $70 >$ Kn > 0.007 including both, the free molecular flow regime and the continuum flow regime at the same time. For this scenario no general, analytical solution for the pressure profile is known to the author and numerical simulations have to be employed.

We use a levitated particle inside the HCPCF as a nanomechanical pressure sensor and directly measure pressure profiles along the hollow core fiber. The COM motion of a levitated particle is damped by the surrounding gas with a damping rate $\gamma_\mathrm{p}(p)$, which depends on the local pressure p. We have two methods to measure the damping of a levitated particle and hence measure the local pressure. For a highly underdamped oscillator $\gamma_\mathrm{p} \ll \Omega_\mathrm{m}$, feedback cooling is used to perform energy relaxation measurements. For the remaining cases of $\gamma_\mathrm{p} < \Omega_\mathrm{m}$ and $\gamma_\mathrm{p} \gtrsim \Omega_\mathrm{m}$ the read-out of the COM motion alone is sufficient to infer the damping from the mechanical spectrum, see equation 2.13.

The ability to choose the flow regime in the HCPCF experiment and directly measure the pressure profile makes this experiment an ideal candidate for hydrodynamical studies. In the next chapter the measurement and calibration procedures are described, followed by a chapter in which a direct measurement of the pressure profile for $p_l = 0.2$ mbar and $p_r = 100$ mbar is performed. The results directly contradict a theoretical prediction and an indirect measurement of Yang and Garimella [93]. To further understand our findings, more measurements for different pressure settings are performed and confirmed by direct simulation Monte Carlo (DSMC) simulations from the John Sader group of the University of Melbourne.

2.5.1. Measurement Procedures and Calibration

Spectral Evaluation

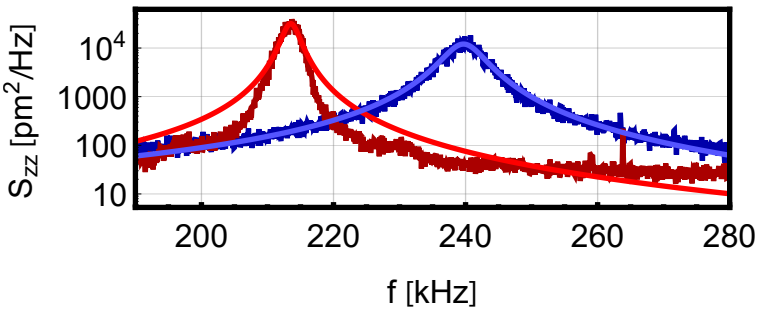

Figure 2.39.: Mechanical noise-power spectrum with fits of a particle at $p = 0.7$ mbar (red curve) and at $p = 5$ mbar (blue curve). The inhomogeneous broadening at low pressures is caused by drifts in the mechanical frequency and limits the spectral evaluation method.

The width of the noise-power spectrum, see equation 2.13, is given by the mechanical damping rate γ_p. Figure 2.39 shows two measured noise power spectra of the COM motion of a levitated particle. The red curve shows data taken at a pressure of $p = 0.7$ mbar and the blue curve at a pressure of $p = 5$ mbar. Power drifts in the trap laser cause drifts in the mechanical frequency Ω_m of the particle and lead to inhomogeneous broadening of the spectrum (red curve). We found experimentally that this effect limits the spectral evaluation method to damping rates above $\gamma_\mathrm{p} > 4$ kHz [62]. The effects of inhomogeneous broadening become negligible for higher pressures, where the damping γ_p dominates the width of the mechanical spectrum and where fits agree well with the measured data (blue curve).

Energy Relaxation Measurement

In the regime in which the spectral evaluation method breaks down feedback cooling is used for energy relaxation measurements. The Fokker-Planck equation describing the mean energy $E(t)$ of the COM motion at an environmental temperature T_0 is [94]

$$\dot{E}(t) = -\gamma_\mathrm{p} E(t) + \gamma_\mathrm{p} k_\mathrm{B} T_0. \tag{2.28}$$

Note that this equation will appear in chapter 3.1.5 in a modified version including recoil heating and feedback noise. However, recoil heating and feedback noise are small in the regime considered here and can be neglected. For

an initial state $E(t = 0) = E_0$ the solution of equation 2.28 is

$$E(t) = k_B T_0 + (E_0 - k_B T_0) e^{-\gamma_p t}. \tag{2.29}$$

In order to measure the relaxation constant and hence, the damping γ_p, the

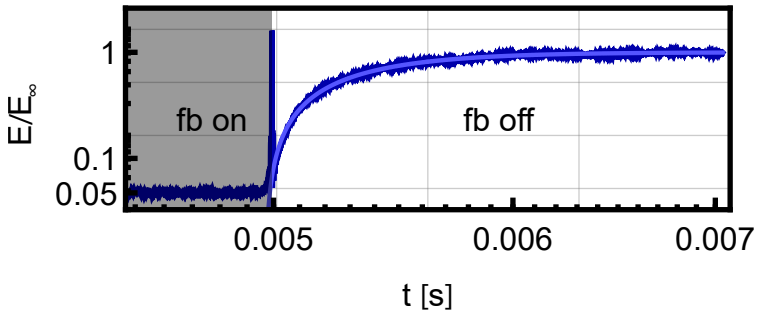

Figure 2.40.: Energy transient of the COM motion (dark blue curve) at a pressure of $p = 0.7$ mbar [62]. Feedback cooling is switched on until $t < 4.9 \times 10^{-3}$ s (grey shaded area) and switched off after. The COM motion is prepared at a low energy state $E_0 < k_B T_0$ and relaxes back to thermal equilibrium $E_\infty = k_B T_0$ with the damping rate γ_p. The light blue line is an exponential fit to the data (dark blue). The sharp peak is an electronic artefact due to the switching process.

particle is initially prepared in a low energy state $E_0 < k_B T_0$ with feedback cooling. If feedback cooling is switched off, the energy evolves according to equation 2.29 and relaxes back to thermal equilibrium $E(t = \infty) = k_B T_0$. Figure 2.40 shows a relaxation measurement at pressure of $p = 0.7$ mbar. The energy trajectory (dark blue curve) corresponds to an ensemble average over approximately 2000 repetitions of a cooling cycle. For each repetition the particle is cooled until the steady state E_0 is reached and then, feedback cooling is switched off until the COM motion reaches thermal equilibrium. The damping rate γ_p is obtained by fitting the relaxation data to equation 2.29 with γ_p as free fit parameter (solid light blue curve) .

Calibration of the Pressure Sensor

The levitated particle can be used to measure the local damping rate γ_p, and hence local pressure, inside the HCPCF. The relation between damping and pressure is given by equation 2.11 with the particle radius a as free parameter. Each particle has a slightly different radius (the manufacturer specification gives the standard deviation of the particle size as 10% of its radius) and

therefore a calibration for each levitated particle is necessary. The particle is trapped inside (or in front of) the HCPCF and the two vacuum chambers vacL and vacR are directly connected via valve MV3, see figure 2.20, such that $p_l = p_r$. The mechanical damping can now be measured at a known pressure which is read out by the pressure gauges. This procedure is repeated for different pressures, as shown in figure 2.41 and the data is fitted using equation 2.11. The resulting fit function is inverted and used to compute the pressure p for a measured mechanical damping γ_p.

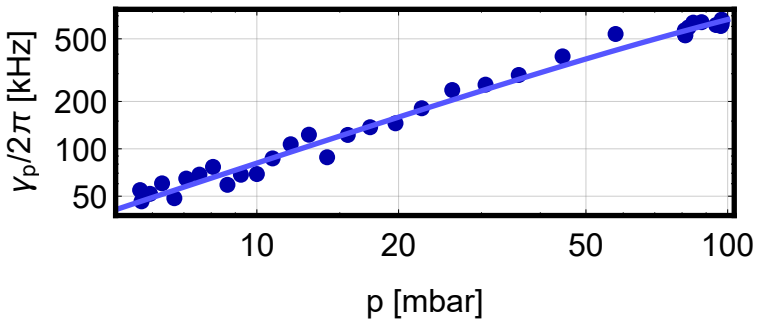

Figure 2.41.: The mechanical damping γ_p is measured as a function of pressure p (blue points). The solid curve is a fit to the measurement data and used as calibration for the nanomechanical sensor.

2.5.2. Measurements and Simulations

A measurement of the pressure distribution between vacL at $p_l = 0.2$ mbar and vacR at $p_r = 100$ mbar is shown in figure 2.42. At the beginning of the measurement a particle is positioned in front of the HCPCF inside vacL and successively transported towards vacR. On the way, the damping γ_p is measured as a function of position z. The red data points represent energy relaxation measurements and the blue data points represent spectral measurements. The two measurement procedures overlap in the regime between $1-10$ mbar. The data points represented with a circle (in light red as well as in light blue) indicate the limitations of their corresponding measurement methods. For the relaxation measurement, efficient feedback cooling is necessary to get a reliable fit to the energy transient and feedback cooling becomes inefficient at high pressures. The spectral method is limited by inhomogeneous broadening and this is why the blue data points reach a plateau around $p \approx 2$ mbar. The solid black line is a linear fit to the pressure profile excluding the circles. The linear pressure dependence describes the data very well and is consistent

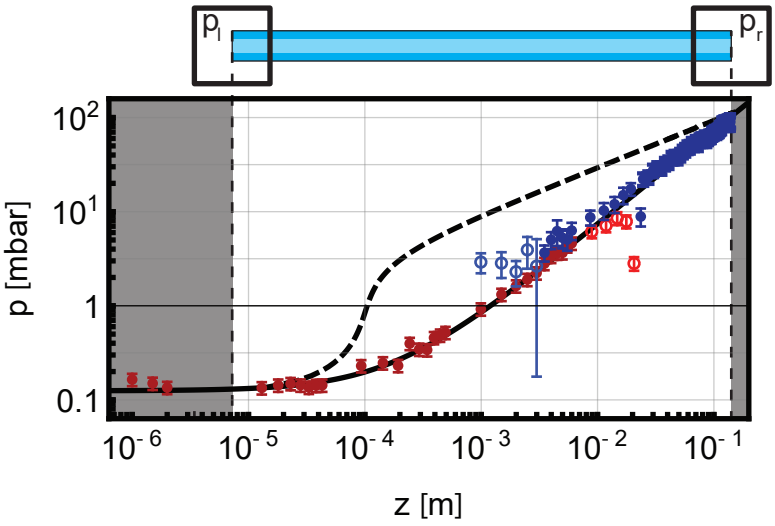

Figure 2.42.: Measured pressure profile inside a HCPCF. A particle is initially trapped in front of the HCPCF in the left vacuum chamber at $p_l = 0.2$ mbar (grey shaded area). The particle is transported in steps towards the right vacuum chamber at $p_r = 100$ mbar. At each position either energy relaxation measurements (red) or spectral measurements (blue) of the pressure are performed [62]. The solid black line is a linear fit to the data points and the dashed black line is the prediction for the pressure profile by Yang and Garimella [93].

with free molecular flow over the entire fiber length. This is a surprising result as the high pressure part of the fiber is described with a Knudsen number of Kn = 0.06 and, according to equation 2.26, a nonlinear pressure profile is expected due to the onset of laminar flow in this regime. Our result also directly contradicts the predictions by Yang and Garimella [93], plotted as dashed line in figure 2.42. Yang and Garimella solved the Burnett equation, which is only valid in the near continuum regime where Kn < 1 at maximum. Their claim that the solution holds for higher Knudsen numbers is rejected with our experimental data.

A rigorous analysis of our experimental situation requires solving the full nonlinear Boltzmann equation, which is done in collaboration with the John Sader group (University of Melbourne) who used direct simulation Monte Carlo (DSMC) methods. Figure 2.43 shows the results of the DSMC simulation for the scenario described above, which is matching our measurement data. This result can be interpreted as a combination of a short continuum flow region at the high pressure end and a free molecular flow for the rest of the pipe. If the

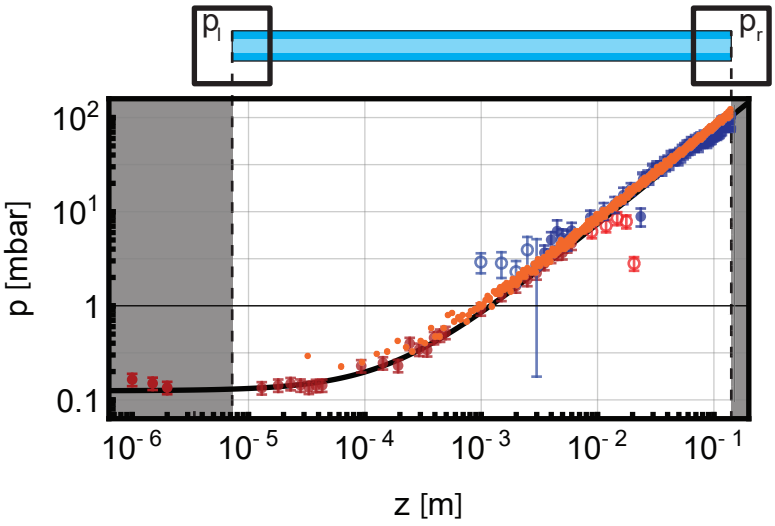

Figure 2.43.: DSMC simulations (orange dots) for pressure profile between $p_l = 0.2$ mbar and $p_r = 100$ mbar, overlapped with the measurement data from figure 2.42.

pressure difference between fiber inlet p_r and the pressure $p_r - \delta p$ at a position close to the inlet is small $\delta p \ll p_r$, the pressure profile for a continuum flow, see equation 2.26, can be approximated by

$$p(z) = \sqrt{(p_r - \delta p)^2 + \frac{z}{l_0}(p_r^2 - (p_r - \delta p)^2)}$$
$$\underset{\delta p \ll p_r}{\approx} p_r - \delta p + \frac{z}{l}\delta p$$

to a linear position dependence. This would explain the overall linear position dependence of pressure profile.

DSMC simulations of the nonlinear Boltzmann equation accurately reproduce our measured pressure profile inside the HCPCF. For the first measurement, between a pressure of $p_l = 0.2$ mbar and a pressure of $p_r = 100$ mbar, a linear dependence between pressure and position is found. A more general set of DSMC simulations, in which the pressure of the left vacuum chamber was held at $p_l = 10$ mbar and the pressure in the right vacuum chamber was selected to be at $p_r = 300$ mbar, at $p_r = 500$ mbar and at $p_r = 700$ mbar, was performed resulting in a nonlinear pressure dependence. The simulation data is shown in figure 2.44, the red curve corresponds to an inlet pressure of $p_r = 300$ mbar, the blue curve to $p_r = 500$ mbar and the green curve to $p_r = 700$ mbar. The same measurement procedure as described above is performed for the pressure parameters of the simulation: The left chamber is held

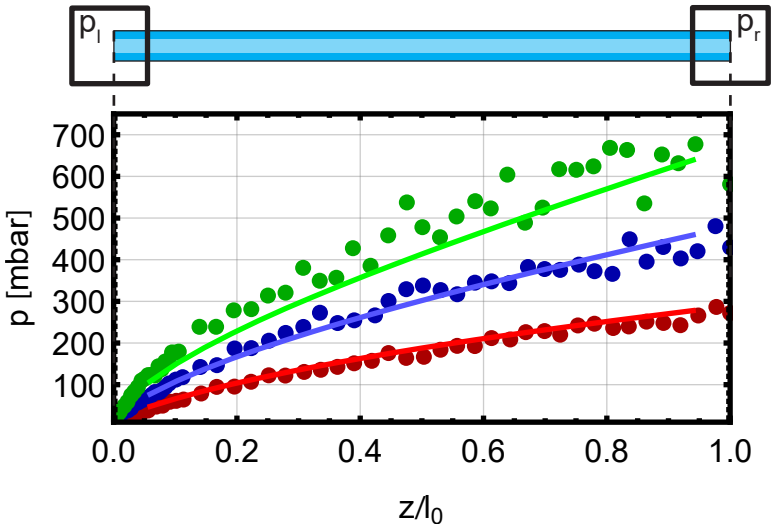

Figure 2.44.: Measured (dots) and DSMC simulation (curve) results for three pressure profiles along a HCPCF. The pressure in the left vacuum chamber is held at $p_l = 10$ mbar for each measurement and the pressure in the right vacuum chamber is held at $p_r = 300$ for the red, $p_r = 500$ mbar for the blue and $p_r = 700$ mbar for the green measured points and simulation results.

at a pressure of $p_l = 10$ mbar and the pressure in the right chamber varies between $p_r = 300$, $p_r = 500$ mbar and $p_r = 700$ mbar. A particle with a diameter of $d = 969$ nm was first calibrated as nanomechanical pressure sensor, see chapter 2.5.1, and then successively moved through the HCPCF for pressure sensing. The measurement results are also shown in figure 2.44 as solid points with the same color coding as the simulation results. The data confirms the nonlinear behaviour predicted by simulations.

2.6. Summary and Outlook

This chapter presented a novel optical trap based on a HCPCF. Particle levitation inside an evacuated hollow core fiber, particle transport with an optical conveyor belt, three-dimensional read-out of the particle COM motion as well as feedback cooling techniques were discussed. The system was used to investigate its potential as a source for loading particles into ultra-high vacuum and as a hydrodynamical platform to investigate relevant regimes of the nonlinear Boltzmann equation. Both applications turned out to be promising and will be further pursued in the future. Here I will discuss the roadmap for the HCPCF experiment as particle source and as hydrodynamical platform.

HCPCF as Particle Source

Currently, the lowest pressure a particle can be levitated both inside and outside of the HCPCF is around $p \approx 0.1$ mbar and is limited by particle loss from the optical trap at lower pressures. This is a phenomenon poorly understood but observed in many levitation experiments [14, 59, 62, 75, 95]. However, three-dimensional feedback cooling is known to stabilize the particle inside the optical trap and should allow levitation in ultra-high vacuum.

In order to transport particles into ultra-high vacuum, the experiment needs to be able to levitate particles below pressures of 0.1 mbar over the full extend of the fiber, hence three dimensional cooling needs to be applicable over the full extend of the fiber. A natural addition to the radiation pressure based feedback cooling along the fiber axis would be parametric feedback cooling along the two remaining radial directions. Parametric feedback cooling is applied via a modulation of the optical potential at twice the mechanical frequency (see chapter 3.1). The modulation can be realized with the already installed acousto-optical modulators in the beam-preparation part of the HCPCF experiment, see figure 2.14 and the radial read-out, necessary to generate the radial feedback signal is already in place, see chapter 2.2.2. The remaining task would be implementation of the parametric feedback electronics. The combination of axial direct feedback and radial parametric feedback can be applied to a levitated particle over the entire range of the fiber and should allow stable levitation at any given pressure.

The next step is fiber integration of the trap, as proposed in chapter 2.4.3. We need to find a more stable mechanical mounting of the individual components. We will start with custom produced GRIN lenses which are already fused onto a SMF. The remaining step is further optimization of aligning and gluing of the combination of GRIN lens and SMF with respect to a HCPCF on a v-groove. The reduction of individual components due to the custom made

parts should simplify this task. The reduction in optical absorption should eliminate the thermal drifts and expansions which were most likely responsible for degradation of the prototypes.

Nanomechanical Pressure Sensor

The successful measurement of pressure profiles along the HCPCF for different pressure gradients and the excellent agreement with DSMC simulations encouraged us to further investigate the hydrodynamical properties of the HCPCF. A critical parameter entering all simulations of pipe flow is the accommodation coefficient α. It defines the interaction between individual gas molecules with the walls of the fiber. For an accommodation coefficient of $\alpha = 1$ each molecule is absorbed by the wall, thermalizes and is re-emitted into a full solid angle. For an accommodation coefficient of $\alpha = 0$, a gas molecule interacts fully specular with the fiber wall, which is in essence a ballistic reflection. Only few experimental measurements exist to obtain values for the accommodation parameter. In most cases, accommodation parameters have to be assumed (e.g. $\alpha = 0.8$ for standard materials).

For our situation, preliminary simulations show that the accommodation coefficient does not affect the pressure profile, but the velocity profile along the fiber, as shown in figure 2.45. For different pressures $p_l < p_r$ there is a

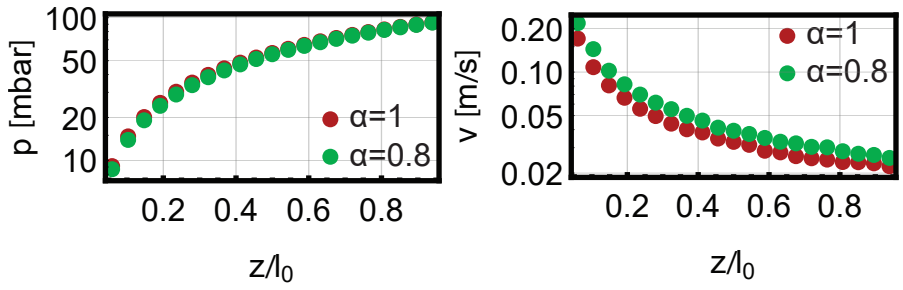

Figure 2.45.: Preliminary DSMC simulations of the pressure profile (left) and the gas velocity profile (right) for different accommodation coefficients.

flow of air from the right to the left vacuum chamber causing a drag force $F_{\mathrm{drag}} = m\gamma u$ on the particle, with u the velocity of the gas. As long as the trap is switched on the optical force is much stronger than the drag force and can be neglected, i.e. $m\Omega^2 z \gg m\gamma_{\mathrm{p}} u$. However, if the trap is switched off the particle will be displaced by the drag force, which is monitored with the laterally mounted CCD camera. The gas velocity at the fiber axis can then be obtained with the switching time and the measured displacement. This

type of measurement would allows us to access the accommodation coefficient experimentally.

3. Cavity Optomechanics With Levitated Nanospheres

Levitated cavity optomechanics is a promising platform for room-temperature quantum experiments and high-precision force sensing. Recent proposals include the preparation of massive superposition states [5, 16, 17, 79, 81] as well as ultra-sensitive force detection, e.g. for deviations from Newtonian gravity [18, 96] or gravitational wave detection [19]. One intriguing feature of levitated optomechanics is the ability to switch off the trapping field and change the system dynamics to a free evolution. A levitated particle, prepared in its ground state of motion, can be released from the optical trap and used to perform a matter-wave type experiment, both on earth [16, 81, 96] and in space [17] thereby testing the predictions of quantum mechanics for macroscopic objects beyond 10^6 atomic mass units.

A necessary requirement for those experiments is stable levitation at ultra-high vacuum and a sufficiently strong coupling of the center of mass motion to the cavity mode, i.e. reaching the strong quantum cooperativity [55] regime

$$C_Q = \frac{4g^2}{\kappa\Gamma} > 1. \tag{3.1}$$

Here, g is the coupling rate between the light field and the mechanical mode, κ the optical losses and Γ the mechanical losses given by

$$\Gamma = \gamma_\mathrm{p}\bar{n}_\mathrm{th} + \Gamma_\mathrm{rc} \tag{3.2}$$

with $\bar{n}_\mathrm{th}$ the occupation number of the thermal bath, γ_p the mechanical coupling rate to the thermal bath and Γ_rc the photon recoil heating. Compared

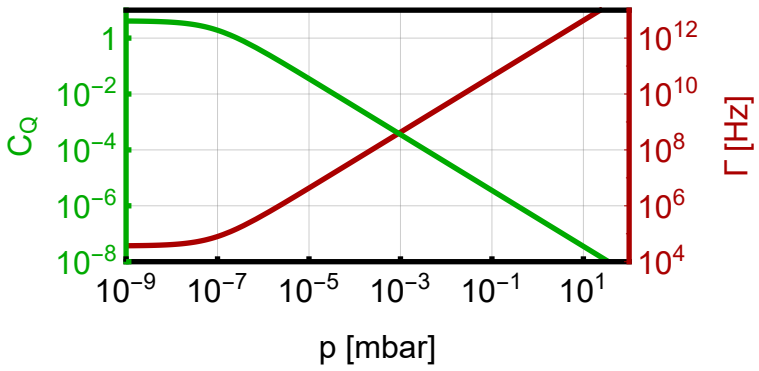

Figure 3.1.: Quantum cooperativity C_Q and mechanical heating Γ dependence projected for ultra-high vacuum for the experimental parameters of [14]. The experiment would reach the strong quantum cooperativity regime if it could be operated at pressures $p < 10^{-8}$ mbar.

to other optomechanical systems, which have a massive support, levitated systems do not suffer from clamping losses. While mechanical quality factors of $Q \approx 10^{12}$ were proposed [5] it became evident that for continuous trapping photon recoil heating sets an ultimate limit on the mechanical losses [57]. Nevertheless, the term $\gamma_{\mathrm{p}}\bar{n}_{\mathrm{th}}$ due to the interaction of a levitated particle with its thermal environment via gas collisions, see chapter 2.1.4, is linear in pressure $\gamma_{\mathrm{p}} \propto p$. This is the main reason why levitated systems can be well isolated from the environment and hence why they are a promising candidate for room-temperature quantum experiments. The photon recoil heating Γ_{rc} is unique to optically levitated systems. The restoring gradient force originates from a laser field which is subject to shot-noise. This unavoidable intensity fluctuations cause the additional heating of the COM motion [57, 97, 98].

Our goal is to enter the strong cooperativity regime $C_Q > 1$. In our previous experiment we demonstrated cavity cooling of a levitated nanoparticle [14] and reached a quantum cooperativity of $C_Q \approx 10^{-7}$, mainly limited by the mechanical losses Γ. The experiment suffered from particle loss around a pressure of $p \approx 1$ mbar. For the experimental parameters in [14] the quantum cooperativity (green) and mechanical losses (red) are projected to low pressures in figure 3.1. This plot clearly shows that if we were able to stabilize the optical trap and bring the system to a pressure of $p \approx 10^{-8}$ mbar, we would reach the strong quantum copperativity regime $C_Q > 1$. A cavity field was used for trapping in the previous experiment, which was the main limiting factor in reaching lower pressures since no feedback stabilization was possible. Here, we combine the three-dimensional feedback control of tweezers with the cavity setup to achieve high vacuum operation and hence large cooperativity. This chapter is portioned into four parts:

- Chapter 3.1 introduces optical tweezer and parametric feedback cooling. The trapping laser is tightly focused with a high numerical aperture objective and numerical methods are used to compute the focal field and the optical forces acting on a particle. A three-dimensional readout scheme and parametric feedback cooling for levitation in vacuum are explained in the second and third part of this chapter. The last part elaborates on photon recoil heating effects.

- Chapter 3.2 provides a brief introduction into cavity optomechanics with levitated particles. The levitation specific Hamiltonian is transformed into the standard optomechanical form and optomechanical cooling along with the quantum cooperativity are explained. Optomechanically induced transparency (OMIT) is introduced as well, which will be used to estimate the quantum cooperativity.

- Chapter 3.3 explains in detail the experimental setup and contains the main technological developments rendering the combination of tweezer and cavity possible. In the beginning, the cavity optomechanics and the tweezer setup are explained independently. The third part deals with cutting and mounting of the cavity mirrors which is necessary to overlap cavity mode with the tweezer trap. The last part explains how a particle is trapped in the tweezer without contaminating the cavity mirrors and how it is aligned with respect to the cavity field .

- Chapter 3.4 gives an overview of the performance of the system. In a first step it is shown that we can operate the tweezer close to the recoil limit in high vacuum. In the second part we measure the optomechanical coupling with OMIT measurements. The last part gives an estimate on the quantum cooperativity C_Q at the current state of the experiment.

3.1. Principles of Optical Tweezers and Parametric Feedback Cooling

The concept of optical tweezers can be traced back to a proposal for trapping of atoms by Arthur Ashkin [99]. It was first demonstrated for small dielectric particles in liquid [100] and later for atoms [6] in vacuum. An optical tweezer, in its simplest form, consists of a single laser beam and a focusing lens. Inside a tightly focused laser beam a small dielectric particle experiences a three-dimensional restoring force and can be trapped.

In 2012 Gieseler at al. demonstrated optical levitation of particles in high vacuum [101]. The particle was stabilized with parametric feedback cooling. A basic experimental setup for an optical tweezer including feedback cooling is shown in figure 3.2. A trapping laser and a feedback laser are superimposed on a polarizing beamsplitter (PBS) and focused with a high numerical aperture (NA) lens (f_{tw}). Scattered light from the particle is collected with a collimation lens (f_{coll}) and used for detection of the particle COM motion in three dimensions. The read-out signal is used to parametrically cool all three directions of motion. The previously mentioned particle loss, see chapter 2.4 for example, around a pressure of $p \approx 1$ mbar is prohibited by the parametric feedback cooling and allows stable trapping in vacuum. The currently lowest reported pressure for stable levitation know to the author is $p = 7 \times 10^{-9}$ mbar [57].

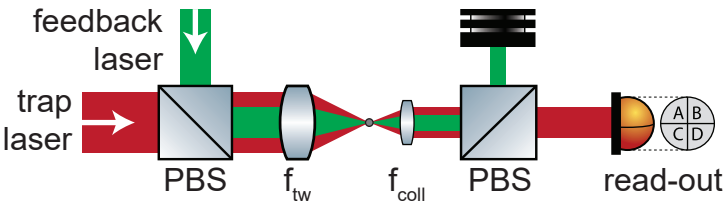

Figure 3.2.: A high NA lens f_{tw} is used for focusing of a trapping and a feedback laser to form an optical trap. A collimation lens f_{coll} is used to collect scattered light from a trapped particle in order to monitor its three-dimensional motion with a split-detection scheme (read-out).

The combination of an optical tweezer with parametric feedback cooling turned out to be a powerful tool in the field of levitated optomechanics. To date it is among the systems with the highest reported room-temperature mechanical quality factor [4] of $Q = 10^8$, alongside high-stress silicon nitride membranes [102] and "soft-clamped" membranes [103]. Besides the achievement of levitation in vacuum, this system is also used for levitation of nitrogen

vacancy centers [104], studies of non-equilibrium dynamics [94, 105], stochastic bi-stable dynamics [106] and nonlinearities in optical potentials [4, 107], transfer of nanoparticles into high vacuum [108], cooling of orthogonal mechanical modes by coherent control [109], measuring of photon recoil heating [57] and confirmation of Kramers turnover [110].

In this chapter I briefly introduce the basic concepts of optical tweezers and parametric feedback cooling. A more detailed description can be found in the PhD theses of Jan Gieseler [111] and Vijay Jain [112]. There is a big conceptual overlap between the optical tweezer and the HCPCF trap described in chapter 2. Here, I will mainly focus on the differences between both systems.

3.1.1. Forces in an Optical Tweezer

An optical tweezer is formed by focusing a Gaussian laser beam with a high numerical aperture (NA) lens. The optical forces arising from the laser acting on a dielectric particle are computed like in chapter 2.1.2. The main differences are particle size and electromagnetic modes forming the trap. Particles with a radius around $a \approx 75$ nm are trapped with a laser wavelength of $\lambda = 1064\,\text{nm} \ll a$ placing the system well into the Rayleigh regime, see chapter 2.1.2. For a tightly focused Gaussian beam the commonly used paraxial approximation is not applicable [47, 113] and a numerical method is used to compute the focal field instead. A second difference compared to the HCPCF trap is the absence of a counterpropagating beam. The scattering force does not vanish and needs to be taken into account.

Tightly Focused Gaussian Beams

The incident Gaussian laser beam used for trapping is described by

$$\begin{aligned}\vec{E}(x,y,z,t) &= E_0 \frac{w_0}{w(z)} e^{-i(kz+2\pi\nu t)} e^{-\frac{x^2+y^2}{w^2(z)}} e^{-ik\frac{x^2+y^2}{2R(z)}} e^{i\zeta(z)} \vec{p} \\ &= E(x,y,z) e^{-i2\pi\nu t} \vec{p}\end{aligned} \tag{3.3}$$

with E_0 the electric field amplitude, w_0 the minimal waist of the Gaussian, the waist function $w(z) = w_0\sqrt{1+(z/\mathrm{z_R})^2}$, the Rayleigh length $\mathrm{z_R} = \pi w_0^2/\lambda$, the radius of curvature of the wavefronts $R(z) = z[1+(z/\mathrm{z_R})^2]$, the wavenumber $k = 2\pi/\lambda$, the laser wavelength λ, the laser frequency ν, the Gouy phase $\zeta(z) = \arctan(z/\mathrm{z_R})$ and the polarization vector $\vec{p}$. Without loss of generality we assume the electric field to be polarized along the x direction $\vec{p} = \vec{e}_x$. The

time averaged intensity of the incident Gaussian laser beam is

$$I(x,y,z) = \frac{2P}{\pi w^2(z)} e^{-2\frac{x^2+y^2}{w^2(z)}}$$

with $P = \int dxdyI$ the optical power of the laser beam.

A lens with focal length f is used to focus a collimated incident laser beam. The relation between the waist w_0 of the incident laser beam and the waist w_{foc} in the focus depends on the numerical aperture $\text{NA} = w_0/f = \tan\theta$, the ratio between initial waist w_0 and the focal length f. The angle θ describes the divergence angle of the focused field. For the case of weak focusing $\tan\theta \approx \theta$ the paraxial approximation holds [113] and the waist in the focal spot is

$$w_{\text{foc}} = \frac{\lambda f}{\pi w_0}.$$

For a tightly focused beam a method described in [47] is used for numerical computations of the focal field. The angular spectrum representation of the focal field of an incident paraxial Gaussian beam focused with a high NA lens is given by [47]

$$\vec{E}(\rho,\varphi,z) = \frac{ikf}{2\pi} e^{-ikf} \int_0^{\theta_{\max}} \int_0^{2\pi} d\phi d\theta \; \vec{E}_\infty(\theta,\phi) e^{ikz\cos\theta} e^{ik\rho\sin\theta\cos(\phi-\varphi)} \sin\theta \quad (3.4)$$

with $\rho = \sqrt{x^2+y^2}$, $\varphi = \arg(x,y)$, $\vec{E}_\infty$ the refracted field after the lens and

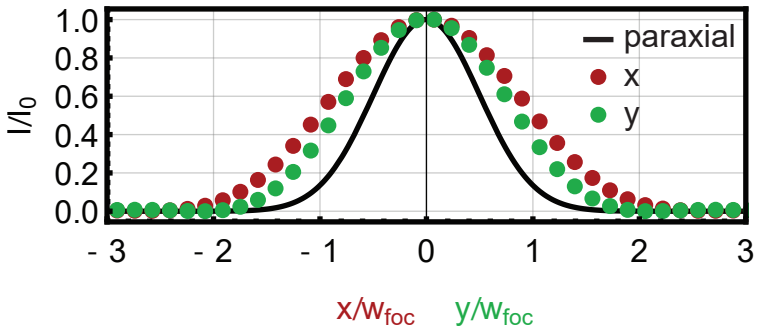

Figure 3.3.: Numerical solution of equation 3.4 for the intensity profile of a tightly focused Gaussian beam with NA = 0.8 along the x-direction (red dots) and the y-direction (green dots) compared to the paraxial approximation (solid black line).

f the focal length. The integral in equation 3.4 is solved numerically for a

lens with NA = 0.8 and the results are shown in figure 3.3, including the paraxial solution. The paraxial approximation underestimates the beam waist (solid black line) and does not resolve the difference along x- (red dots) and y-direction (green dots), which is due to the linear polarization along the x-axis. Since the mechanical frequency depends on the waits of the trapping field, see equation 3.10, this lifts the degeneracy of the mechanical frequencies along the radial directions. To describe our experimental situation correctly, a modified Gaussian beam with different waists in x- and y-direction is fitted to the numerical solution of equation 3.4

$$I(x,y,z) = \frac{2P}{\pi w_{\mathrm{xy}}^2(z)} e^{-\frac{x^2}{w_{\mathrm{xx}}^2(z)} - \frac{y^2}{w_{\mathrm{yy}}^2(z)}} \tag{3.5}$$

with $w_{\mathrm{ij}}(z) = w_i w_j (1 + (z/\mathrm{z_R})^2)$ and w_x and w_y the waist along x and y-direction, respectively. An example is shown in figure 3.4. For the following

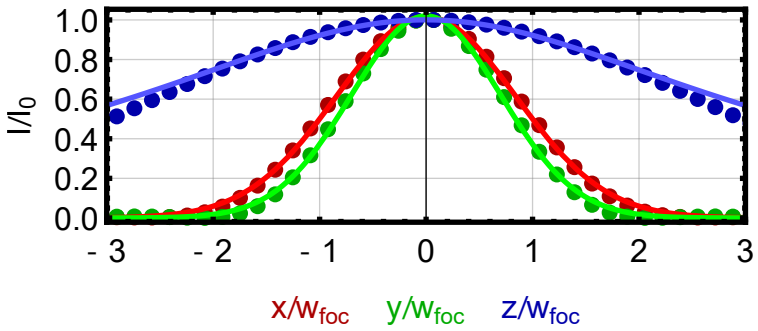

Figure 3.4.: Fits (solid lines) of Gaussian functions to solutions of the angular spectrum representation along x- (blue dots), y- (red dots) and z-direction (green dots) for a numerical aperture of NA = 0.8.

considerations the fitted Gaussian beam is used instead of the numerical results.

Rayleigh Approximation

In analogy to chapter 2.1.2, the optical forces can be computed with the Rayleigh approximation as the particle radius $a = 75$ nm is much smaller than the laser wavelength $\lambda = 1064$ nm. The validity of the Rayleigh approximation for this size regime is also backed up by the results of the GLMT simulations for the HCPCF trap, see figure 2.10. The main difference to the HCPCF system is the absence of a second optical beam. Therefore the scattering force does not vanish and needs to be taken into account. The scattering

force of a laser propagating along z-direction in a single beam dipole trap is [50]

$$\vec{F}_{\text{scatt}} = \frac{\sigma_{\text{scatt}}}{c} I \vec{e}_z \tag{3.6}$$

with c the speed of light and $\sigma_{\text{scatt}} = 8/3\pi k^4 a^6 (\varepsilon - 1)^2/(\varepsilon + 2)^2$ the scattering

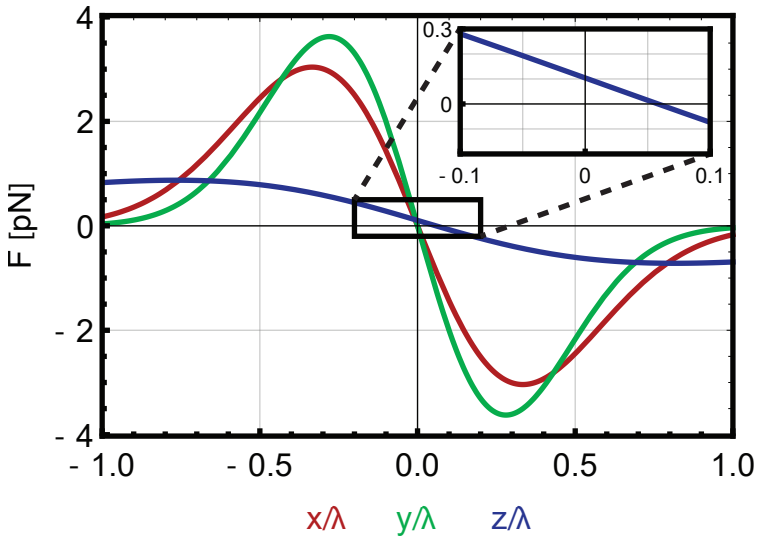

Figure 3.5.: Optical forces on a levitated $a = 75$nm particle along the x- (red), y- (green) and the z-direction (blue). Note that the scattering force pushes the particle away from the beam center and the equilibrium position is shifted. The inset is a zoom-in of the axial force close to the beam center.

cross section, ε the dielectric constant of the particle and $\vec{e}_z$ the unit vector along the axis of beam propagation z. Here, the intensity I is the modified Gaussian (the fitted result from the previous chapter). The gradient force is, as in chapter 2.1.2, given by

$$\vec{F}_{\nabla} = \frac{\alpha}{2} \nabla \vec{E}^2 = \frac{\alpha}{2c\varepsilon_0} \nabla I \tag{3.7}$$

with the particle polarizability $\alpha = 4\pi\varepsilon_0 a^3 (\epsilon - 1)/(\epsilon + 2)$. The optical forces acting onto a silica particle with a radius $a = 75$nm are shown in figure 3.5. A particle will be trapped where $\vec{F}_{\nabla} + \vec{F}_{\text{scatt}} = 0$, which is at the beam center along the x- and y-direction and at the axial position z_0 where $\vec{F}_{\nabla}(z_0)\vec{e}_z + \vec{F}_{\text{scatt}}(z_0)\vec{e}_z = 0$.

Harmonic Approximation and Equation of Motion

The optical forces can be further simplified and brought into a similar form as in chapter 2.1.2. For small particle motion, the scattering force can be approximated with a Taylor expansion

$$\vec{F}_{\text{scatt}} = \frac{n_2 \sigma_{\text{scatt}}}{c} I_0 \ \vec{e}_z + O(z^2) \tag{3.8}$$

with $I_0 = 2P/(\pi w_x w_y)$. The gradient force can be harmonically approximated, as already shown in chapter 2.1.2, to

$$\begin{aligned} \vec{F}_\nabla &= \frac{\alpha}{2c\varepsilon_0} \nabla I \\ &\approx \frac{4P\alpha}{\pi c \varepsilon_0 w_x w_y} \Big[\frac{x}{w_x^2} \vec{e}_x + \frac{y}{w_y^2} \vec{e}_y + \frac{z}{{z_\text{R}}^2} \vec{e}_z \Big]. \end{aligned} \tag{3.9}$$

The dynamics of a levitated particle in an optical tweezer are described by a thermally driven, damped, three-dimensional harmonic oscillator. The optical force along the radial x- or y-direction is conservative and can be written as gradient of an optical potential $\vec{F}_\nabla = -\nabla U_{\text{opt}}$, see equation 3.9. The oscillation frequencies along the radial directions are given by

$$\left(\Omega_\text{m}^{x,y}\right)^2 = \frac{4P\alpha}{m\pi c\varepsilon_0 w_x w_y} \frac{1}{w_{x,y}^2} \tag{3.10}$$

and along the axial direction by

$$\left(\Omega_\text{m}^{z}\right)^2 = \frac{4P\alpha}{m\pi c\varepsilon_0 w_x w_y} \frac{1}{{z_\text{R}}^2} \tag{3.11}$$

with P the power in the trapping laser. The equation of motions are the same as in chapter 2.1.4, for example along the x-direction

$$m\ddot{x} + m\gamma_\text{p}\dot{x} + m\Omega_\text{x}^2 x = F_\text{th} \tag{3.12}$$

with $m\gamma_\text{p}\dot{x}$ a Stokes-like friction force caused by interactions with surrounding gas particles and F_th a Brownian force noise at room temperature [55], also caused by collisions with gas molecules surrounding the particle. The axial direction (z) is modified due to the presence of the scattering force

$$m\ddot{z} + m\gamma_\text{p}\dot{z} + m\Omega_\text{z}^2 z = F_\text{th} + F_\text{scatt}.$$

For small particle motion, the scattering force is constant, see equation 3.8, and a new displacement variable $z \to \zeta = z - F_\text{scatt}/\Omega_\text{m}^2/m$, shifted by the

offset introduced by the constant scattering force, is introduced with $\dot{\zeta} = \dot{z}$ and $\ddot{\zeta} = \ddot{z}$. The transformation returns the equation of motion into the typical harmonic oscillator form and to keep a simple notation the new variable ζ is replaced by z

$$m\ddot{z} + m\gamma_{\mathrm{p}}\dot{z} + \Omega_{\mathrm{z}}^2 z = F_{\mathrm{th}} \tag{3.13}$$

Axial Stability in a Tweezer

The gradient force along all directions is attractive towards the beam center and forms a stable trap in the two radial dimensions. The scattering force pushes the particle away from the focal region which can destabilize the trap along the axial direction [50, 114]. If the gradient force along z is much stronger than the scattering force $F_{\mathrm{scatt}} \ll \vec{F}_{\nabla} \cdot \vec{e}_z$ the destabilization effect is negligible and three-dimensional trapping is possible. The ratio between maximal gradient force along z direction and scattering force is given by

$$\eta = \frac{\vec{F}_{\nabla} \cdot \vec{e}_z}{F_{\mathrm{scatt}}} \propto \frac{1}{a^3} \frac{\varepsilon + 2}{\varepsilon - 1}. \tag{3.14}$$

It is independent of optical power and only depends on the dielectric constant and radius of the particle. For a particle with a radius of $a = 75$nm and a lens with a numerical aperture of NA $= 0.8$, this ratio is $\eta = 7.5$. In that case, the trapping position is pushed 62 nm away from the focal position. This effect is shown in the inset of the force plot, see figure 3.5.

3.1.2. Tweezer Read-Out

A levitated particle scatters light off the trapping field with a position dependent phase. The phase information is read out with a split-detection scheme, similar to the detection scheme for the HCPCF experiment (chapter 2.1.5 and chapter 2.2.2), and allows three-dimensional monitoring of the COM motion. The read-out is required for parametric feedback cooling, which allows stable levitation in vacuum. The derivation for the read-out is similar to [111, 112] and partially based on a private communication with Jan Gieseler.

Gaussian Fields in the Focus and in the Far-Field

The levitated particle is treated as a dipole excited by a Gaussian trapping laser $\vec{E}_{\mathrm{tr}}$, see equation 3.3, that is linearly polarized along the x-direction. A trapped particle is close to the focal point where $x, y \ll w_0$ and $z \ll \mathrm{z_R}$, such

that the field exciting the particle can be approximated as a plane wave with

$$\vec{E}_{\mathrm{tr}}^{\mathrm{foc}} \approx E_0 e^{i\left(kz-\frac{z}{z_R}\right)}\vec{e}_x. \tag{3.15}$$

The trapping laser $\vec{E}_{\mathrm{tr}}$ also serves as local oscillator. In the far-field ($z \gg \mathrm{z_R}$) it can be approximated by

$$\vec{E}_{\mathrm{tr}}^{\mathrm{ff}} \approx E_0 \frac{\mathrm{z_R}}{z} e^{-\frac{z(x^2+y^2)}{w_0 z}} e^{ikz+k\frac{x^2+y^2}{2z}-\frac{\pi}{2}}\vec{e}_x.$$

and application of the paraxial approximation (light after the focal spot is collimated with the collimation lens f_{coll}, see figure 3.2) $z \gg x, y$ and therefore $r = \sqrt{x^2+y^2+z^2} \approx z$ further simplifies the expression to

$$\vec{E}_{\mathrm{tr}}^{\mathrm{ff}} \approx E_0 \frac{\mathrm{z_R}}{r} e^{ikr-\frac{\pi}{2}}\vec{e}_x = E_{\mathrm{tr}} e^{ikr-\frac{\pi}{2}}\vec{e}_x.$$

with $E_{\mathrm{tr}} = E_0 \mathrm{z_R}/r$

Scattered Light Field of a Levitated Particle

The electric field of a point-dipole is given by [47]

$$\vec{E}_{dp}(\vec{r},\vec{\delta r}) = \frac{\omega^2}{\varepsilon_0 c^2}\mathbf{G}(\vec{r},\vec{\delta r})\cdot\mu \tag{3.16}$$

with $\omega = 2\pi c/\lambda$, $\mathbf{G}$ the dyadic Green's function, $\vec{\delta r}$ the position of the dipole and $\vec{\mu} = \alpha\vec{E}_{\mathrm{tr}}$ the dipole moment of the trapped particle excited by the trapping field $\vec{E}_{\mathrm{tr}}$. The dyadic Green's function in the far-field is [47]

$$\mathbf{G}(\vec{r},\vec{\delta r}) = \frac{e^{ikr}}{4\pi r} e^{ik\left(\frac{x\delta x}{r}+\frac{y\delta y}{r}+\frac{z\delta z}{r}\right)} \begin{pmatrix} (1-x^2/r^2) & -xy/r^2 & -xz/r^2 \\ -xy/r^2 & (1-y^2/r^2) & -yz/r^2 \\ -xz/r^2 & -yz/r^2 & (1-z^2/r^2) \end{pmatrix}.$$

Combination of the dyadic Green's function and the trapping field inside the focus, see equation 3.15, results in this expression for the scattered field from the particle

$$\vec{E}_{dp}^{\mathrm{ff}}(\vec{r},\vec{\delta r}) = \frac{\alpha E_0 \omega^2}{4\pi r \varepsilon_0 c^2} e^{i\left(k-\frac{1}{\mathrm{z_R}}\right)\delta z} e^{ik\left(r+\frac{x\delta x}{r}+\frac{y\delta y}{r}+\frac{z\delta z}{r}\right)} \begin{pmatrix} (1-x^2/r^2) \\ -xy/r^2 \\ -xz/r^2 \end{pmatrix}.$$

It is detected in the far-field and hence, the paraxial approximation further simplifies this expression to

$$\vec{E}_{dp}^{\mathrm{ff}}(\vec{r},\vec{\delta r}) = E_{\mathrm{dp}} e^{ikr} e^{i(k_x\delta x + k_y\delta y + K_z\delta z)}\vec{e}_x.$$

with $E_{\mathrm{dp}} = \alpha E_0 \omega^2/(4\pi r\varepsilon_0 c^2)$, $k_x = kx/r$, $k_y = ky/r$ and $K_z = (k + z/r - 1/\mathrm{z_R})$.

Read-Out Signal and Detection

The interference between scattered light from a particle displaced by $\vec{r} = \delta\vec{r}$ from the focal point and the trapping beam is given by

$$\begin{aligned} I_{\text{sig}} &\propto |\vec{E}^{\text{ff}}_{dp}(\vec{r}, \vec{\delta r}) + \vec{E}^{\text{ff}}_{\text{tr}}(\vec{r})|^2 \\ &= E^2_{\text{dp}} + E^2_{\text{tr}} + 2E_{\text{dp}}E_{\text{tr}} \sin(k_x\delta x + k_y\delta y + K_z\delta z) \end{aligned} \tag{3.17}$$

which will be referred to as signal beam from now on. The detection of the signal beam happens in a similar fashion as the detection in the HCPCF read-out, see chapter 2.1.5 and chapter 2.2.2. A fraction $\eta_{x,y,z}$ of the signal beam is split into three parts and sent to the x-, y- and z-detection, respectively, see figure 3.13.

For the motion along the z-direction a single photodiode Z_1 is used to detect the signal beam $I_z = \eta_z I_{\text{sig}}$. The diode Z_1 returns a signal proportional to

$$\begin{aligned} S_{Z_1} &\propto \int_A dA\ \eta_z I_{\text{sig}} = \eta_z(AE^2_{\text{tr}} + AE^2_{\text{dp}} + 2E_{\text{tr}}E_{\text{dp}} \sin(K_z\delta z) \\ &\propto \eta_z(P_{\text{tr}} + P_{\text{dp}} + 2\sqrt{P_{\text{tr}}P_{\text{dp}}} \sin(K_z\delta z)) \\ &\approx \eta_z(P_{\text{tr}} + 2\sqrt{P_{\text{tr}}P_{\text{dp}}} \sin(K_z\delta z)) \end{aligned} \tag{3.18}$$

with A the area of the photodiode, P_{tr} the power in the optical trap and P_{dp} the scattered power by the particle. The scattered power of the dipole is small compared to the trap power, i.e. $P^2_{\text{dp}} \ll \sqrt{P_{\text{tr}}P_{\text{dp}}}, P_{\text{tr}}$ and can be neglected. A second photodiode Z_2 is used to detect a fraction η_z of the trapping laser before interaction with the particle. The resulting read-out signal in axial direction is the difference between the two signals

$$\begin{aligned} S_z &= S_{Z_1} - S_{Z_2} = \eta_z(P_{\text{dp}} + 2c_z\sqrt{P_{\text{tr}}P_{\text{dp}}} \sin(K_z\delta z)) \\ &\approx 2\eta_z c_z K_z \sqrt{P_{\text{tr}}P_{\text{dp}}}\ \delta z \end{aligned} \tag{3.19}$$

where we use the fact that for small displacements δz the sine function can be approximated with its argument. The resulting signal is therefore proportional to the particle displacement along the axial direction δz.

The radial read-out is based on a split-detection and is the same along x- and y-direction up to a rotation by 90° degree. A fraction of the signal beam $I_x = \eta_x I_{\text{sig}}$ is split into two halves along the y-axis ($x = 0$) and detected individually, see figure 3.13, with the photodiodes X_1 and X_2. The read-out

signal is proportional to the difference between the two detector signals

$$\begin{aligned} S_x &= S_{X_1} - S_{X_2} = \eta_x \left(\int_{-x_0}^{0} dx\ dy\ I_{\text{sig}} - \int_{0}^{x_0} dx\ dy\ I_{\text{sig}} \right) \\ &= \frac{8r^2 \eta_x E_{\text{dp}} E_{\text{tr}}}{\delta x \delta y k^2} \left[\cos\left(\frac{k\delta x\ x_0}{r}\right) - 1 \right] \cos(K_z \delta z) \sin\left(\frac{k\delta y\ y_0}{r}\right) \\ &\approx 2\eta_x c_x k_{\text{x0}} \sqrt{P_{\text{tr}} P_{\text{dp}}}\ \delta x \end{aligned} \tag{3.20}$$

with $k_{x0} = kx_0/r$ and x_0, y_0 the extend of the detectors. It is important to realize that equation 3.17 is an anti-symmetric function in the variable $k_x = kx/r$ and hence, in the x-variable. Due to the split-detection scheme, the symmetric contributions (containing z and y particle signal) with respect to the integration axis vanish up to third order in displacement and the anti-symmetric contribution, namely the particle signal along the x-direction, survives. In the the last step, all trigonometric functions are expanded into a Taylor series up to second order in $\delta x, \delta y$ and δz and the resulting signal is proportional to the displacement along the x-direction.

3.1.3. Parametric Feedback Cooling

Optical traps suffer from noise sources that are heating the particle's COM motion. Some are of technical nature, such as classical laser intensity noise or vibrations of the trap position [115]. There exist also more complicated heating mechanisms coupling the COM motion to the internal temperature of the particle, for example [59, 61]. A combination of mechanisms driving the particle motion will lead to particle loss from of the trap at low pressures. This is a phenomenon reported by multiple research groups for different experiments [14, 59, 62, 75, 95] and it typically happens at a pressure around $p \approx 1$ mbar. For optical tweezers this problem can be circumvented by parametric feedback cooling of all three motional directions [101]. Parametric feedback cooling is implemented with a second laser (the feedback laser) which is superimposed with the trapping laser, see figure 3.2, and which is modulated at twice the mechanical frequency $2\Omega_{\text{m}}$. In more detail, each directions' modulation at twice the mechanical frequency is summed to a single modulation signal and used as a feedback signal. Therefore, three-dimensional parametric feedback cooling requires only one additional laser beam co-propagating with the trapping laser. This is in contrast to linear optical feedback cooling schemes where one additional laser per direction [73, 75] or where multiple read-out lasers [74] are necessary.

A detailed theory of parametric feedback control can be found in [105, 111, 112] and a quantum description in [116]. To describe the relevant effects of parametric feedback for this thesis an approach from [117] is used.

In parametric feedback cooling the spring constant of an oscillator is modulated at twice the mechanical frequency. In optically levitated systems, the spring constant is proportional to the power of the trapping laser and hence a modulation of the trapping laser power is sufficient. To circumvent obstruction of the read-out, which is based on the trapping laser, an additional feedback laser is superimposed with the trapping laser and used for modulation instead. The equation of motion is extended by the feedback force $F_{\mathrm{fb}} = \Delta k/(x_0^2\Omega_{\mathrm{m}})x^2\dot{x}$ with Δk the modulation amplitude of the spring constant and x_0 the mean Brownian amplitude of the particle

$$\ddot{x} + \gamma_{\mathrm{p}}\dot{x} + \Omega_{\mathrm{m}}^2 x = \frac{F_{\mathrm{th}} + F_{\mathrm{fb}}}{m}. \tag{3.21}$$

Without loss of generality the principles are explained for the x-direction, the treatment of the other directions is analogous. With the linear-fluctuation approximation $x = \bar{x} + \delta x$ ($\bar{x}$: slowly varying amplitude, δx: fast fluctuations) the equation of motion 3.21 can be separated into an equation for the slowly varying amplitude and an equation for the fluctuations. The fluctuations are much smaller than the mean amplitude $|\delta x| \ll |\bar{x}|$ and the feedback force can be approximated to linear order in fluctuations

$$\begin{aligned} F_{\mathrm{fb}} &= \frac{\Delta k}{x_0^2\Omega_{\mathrm{m}}}(\bar{x} + \delta x)^2(\dot{\bar{x}} + \delta\dot{x}) \\ &\approx \frac{\Delta k}{x_0^2\Omega_{\mathrm{m}}}(\bar{x}^2\dot{\bar{x}} + 2\bar{x}\dot{\bar{x}}\delta x + \bar{x}^2\delta\dot{x}) \end{aligned}$$

For simplicity we change the notation for the fluctuations $\delta x \to x$ and the equation of motion for the fluctuations becomes

$$\ddot{x} + (\gamma_{\mathrm{p}} + \gamma_{\mathrm{fb}})\dot{x} + (\Omega_{\mathrm{m}}^2 + \Omega_{\mathrm{fb}}^2)x = \frac{F_{\mathrm{th}}}{m} \tag{3.22}$$

with the optical spring $\Omega_{\mathrm{fb}}^2 = \Delta k\dot{\bar{x}}\bar{x}/(x_0^2\Omega_{\mathrm{m}}m)$ and the optical damping $\gamma_{\mathrm{fb}} = \Delta k\bar{x}^2/(x_0^2\Omega_{\mathrm{m}}m)$. This approximation resembles the same dynamics as in linear feedback cooling, see chapter 2.3.1. The mechanical noise power spectral density is given by

$$S_{xx}(\omega) = \frac{2k_BT_0\gamma_{\mathrm{p}}}{\pi m}\frac{1}{(\Omega_{\mathrm{m}}^2 + \Omega_{\mathrm{fb}}^2 - \omega^2)^2 + (\gamma_{\mathrm{p}} + \gamma_{\mathrm{fb}})^2\omega^2}.$$

For $\Omega_{\mathrm{fb}} \ll \Omega_{\mathrm{m}}$ and $\gamma_{\mathrm{eff}} = \gamma_{\mathrm{p}} + \gamma_{\mathrm{fb}}$ an effective COM mode temperature can be defined

$$T_{\mathrm{eff}} = T_0 \frac{\gamma_{\mathrm{p}}}{\gamma_{\mathrm{eff}}} \tag{3.23}$$

Figure 3.6 shows a measurement of the effective mode temperature for a par-

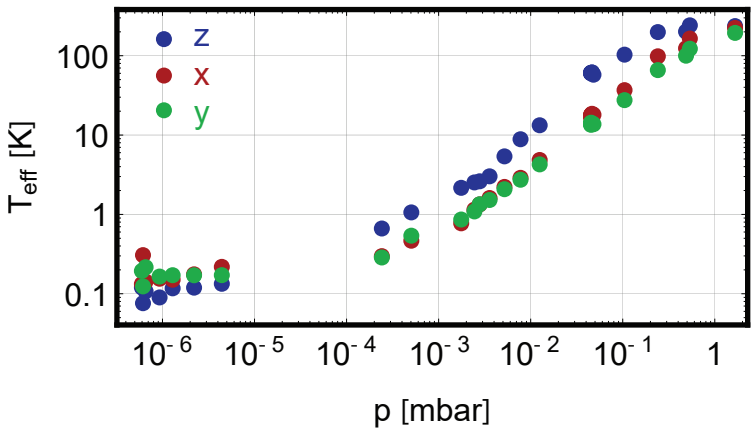

Figure 3.6.: Measured effective mode temperature as a function of pressure while three-dimensional parametric feedback cooling is switched on.

ticle with a radius of $a = 71.5$ nm while parametric feedback cooling switched on. The optical power in the feedback laser is approximately 1.5% of the optical power inside the trapping laser. The experimental implementation is described in chapter 3.3. During the measurement the pressure inside the vacuum chamber was reduced to the final base pressure of our current vacuum system $p = 6 \times 10^{-7}$ mbar. The effective temperature for each direction reaches a plateau around $T_{\mathrm{eff}} \approx 100$ mK. The performance of the feedback cooling is limited by the reduced signal-to-noise ratio at low effective temperatures but sufficient to keep the particle trapped in high vacuum. Note that the read-out can be improved and effective mode temperatures below 1 mK can be reached [57].

3.1.4. Beyond the Harmonic Approximation

The harmonic approximation, see chapter 3.1.1, works well for small displacements. However, if the amplitude grows bigger anharmonic effects become visible [4]. One indication is coupling of orthogonal modes or appearance of higher harmonics of the COM motion.

The harmonic approximation is based on a Taylor expansion of the optical potential that is truncated at the quadratic order (hence the term harmonic), which is equivalent to a Taylor expansion of the optical force to linear order. Here, the force along y-direction is developed into a Taylor series around the trapping position $(0, 0, z_0)$

$$\mathcal{T}\left(\vec{F}_\nabla \cdot \vec{e}_y\right) = \frac{2P\alpha}{c\varepsilon_0 \pi w_x w_y}\Bigg[\underbrace{\frac{1}{w_y^2(z_0)}y}_{\text{harmonic approx.}} + \underbrace{\frac{4z_R^4}{w_y^3(z_0)}y(z-z_0)}_{\text{1. anharmonic term}} + ...\Bigg] \tag{3.24}$$

The first term gives rise to the harmonic force. The second term is due to the nonlinear nature of the gradient force and introduces a coupling to the z motion of the particle. Intuitively, this can be understood by considering the waist of the trapping laser beam as seen by the particle. If the particle has a large amplitude along the z-direction, it samples a region where the waist of the laser beam is not constant anymore $w_0 \neq w(z)$ and hence, the confinement of the orthogonal modes changes depending on the particle position along the z-axis. This effect is weak but can be observed for large amplitudes. A similar term will appear in the second radial direction x. The axial direction z does not experience a coupling to the radial directions in quadratic order, as the amplitude of the radial motion is approximately a factor of four smaller compared to the axial motion and hence has less influence. Figure 3.7 shows

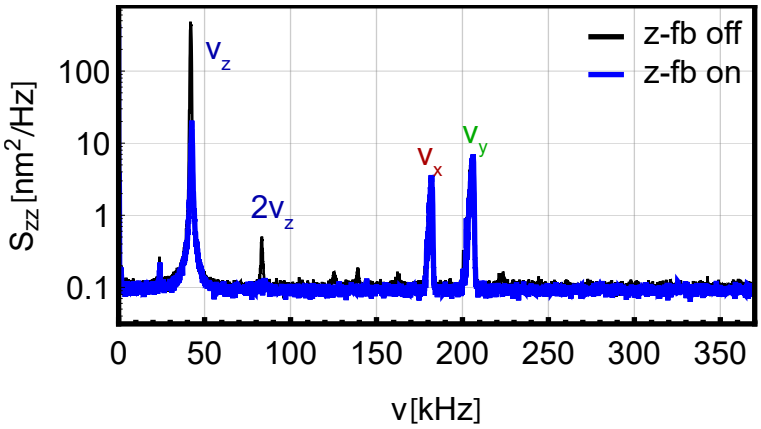

Figure 3.7.: Axial spectrum S_{zz} at $p = 4 \times 10^{-2}$mbar: While z-feedback cooling is switched on (blue trace), the area is reduced by a factor of 20 and the second harmonic peak vanishes, compared to feedback switched off (black trace). The two radial COM motions are present due to imperfect alignment.

two measured noise-power spectra of the z read-out. The axial mechanical

frequency is at $\Omega_z = 2\pi \times 42$ kHz and while feedback cooling is switched off the second harmonic of the axial motion is visible at $2\Omega_z = 2\pi \times 84$ kHz. Remnants of the two radial COM motions Ω_x, Ω_y are also present in the axial read-out. They do not appear due to anharmonic coupling, they origin from imperfect alignment of the axial read-out. While feedback cooling is switched on (blue curve) the area of the spectrum reduces from room temperature (black curve) to an effective mode temperature of $T_{\text{eff}} = 15$ K at a pressure of $p = 4 \times 10^{-2}$ mbar. As the amplitude of the z-motion is reduced the anharmonicities of the potential are not sampled anymore and the second harmonic peak vanishes.

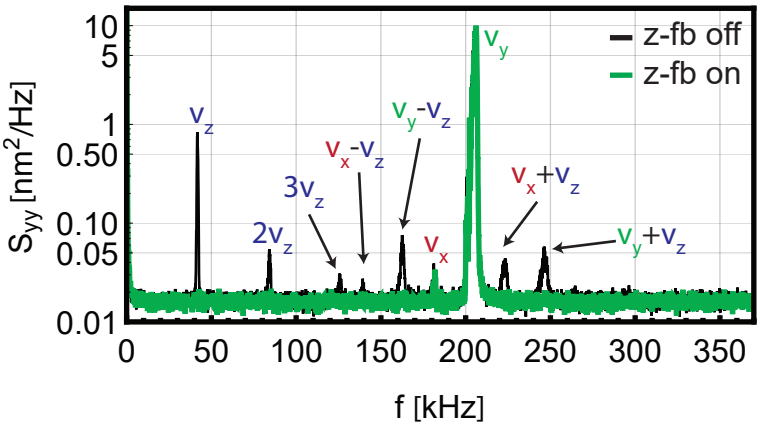

Figure 3.8.: Radial spectrum S_{yy} at $p = 4 \times 10^{-2}$ mbar: While feedback cooling is switched off (black curve) mixing between spatial directions and appearance of the axial motion is observable. If z-feedback cooling is switched on, the y peak is unaffected, the mixing is suppressed and the axial peaks vanish. Due to imperfect alignment a small x peak is present in the y read-out.

The radial read-out has a more complicated spectrum. Figure 3.8 displays two measured spectra S_{yy}, one while z-feedback is switched on (green curve) and one while z-feedback is switched off (black curve). The most prominent peak at $\nu = 206$ kHz belongs to the y-motion at Ω_y. Due to imperfect alignment, in particular the angle of the D-shaped mirror, there is also a small peak which belongs to the x-motion at $\nu = 181$ kHz. The axial motion in combination with the anharmonicity generates sidebands at $\nu = \nu_{x,y} \pm \nu_z$. This is due to the mixing term between z and y in equation 3.24, the axial displacement is imprinted on the radial motion. The axial COM motion including second and third harmonic are also visible in the y read-out. If z-feedback cooling is switched on (green curve), the axial COM motion does not sample the anharmonicity and all mixing terms and the axial peaks with its higher harmonics

vanish from the spectrum. The x and y peak are unaffected by the feedback cooling, as expected. A similar behaviour is found for the S_{xx} spectrum. These two measurements confirm the nonlinear behaviour of the gradient force and also the origin of the mixing between spatial directions.

3.1.5. Photon Recoil

The gradient force that is responsible for the three-dimensional confinement of the particle is based on a laser field. In general a laser field is subject to intensity and phase noise, which can be further divided into classical and quantum noise. An optical tweezer is not sensitive to phase noise because the gradient force $\vec{F}_\nabla \propto \nabla I$ of a single Gaussian beam is determined solely by its intensity profile. In turn, classical intensity noise of the laser gives rise to parametric heating [115], which can be avoided by using a low-noise laser and by actively stabilizing the intensity in a narrow bandwidth around twice the mechanical frequency.

The quantum nature of light sets a fundamental limit to the intensity noise of a laser, the shot-noise limit. A coherent state (the typical output of a laser) of power P has a mean number of photons $\bar{n} = P/\hbar\omega$ and an uncertainty $\sqrt{\bar{n}}$ due to quantum fluctuations. These fluctuations in the trapping field are imprinted on the gradient force and also on the particle motion. Random scattering events of photons transfer momentum onto the particle, resulting in the photon recoil heating Γ_{rc}. A typical recoil heating rate of an optical tweezer is on the order of $\Gamma_{\mathrm{rc}} \approx 10$ kHz [57]. The Brownian force noise causes a pressure dependent heating rate $\Gamma = \gamma_{\mathrm{p}}\bar{n}_{\mathrm{th}}$, due to collisions with the background gas, see equation 2.12 and equation 3.2, and scales like $\Gamma = \gamma_{\mathrm{p}}\bar{n}_{\mathrm{th}} \approx p \times 2 \times 10^8$ kHz/mbar for typical tweezer parameters (particle radius $a = 75$ nm, mechanical frequency $\Omega_{\mathrm{m}} = 2\pi \times 160$ kHz). Therefore, photon recoil only becomes relevant at low pressures. It was recently observed for a levitated particle at a pressure of $p \approx 10^{-8}$mbar [57] where photon recoil becomes comparable to collisions with gas molecules.

The following derivation is based on [57]: The Fokker-Planck equation describing the dynamics of the mean particle energy E is

$$\dot{E}(t) = -\gamma E(t) - \gamma E_\infty \tag{3.25}$$

with γ the cumulative damping and E_∞ the equilibrium temperature of the system. The damping $\gamma = \gamma_{\mathrm{p}} + \gamma_{\mathrm{rad}} + \gamma_{\mathrm{fb}}$ is the sum of damping due to collisions with gas molecules γ_{p}, radiation damping γ_{rad} due to scattering between particle and photons [118] and the effect of parametric feedback cooling γ_{fb}.

The equilibrium temperature is

$$E_\infty = \hbar\Omega_\mathrm{m}\frac{\Gamma}{\gamma} = \hbar\Omega_\mathrm{m}\frac{\Gamma_p + \Gamma_\mathrm{rc} + \Gamma_\mathrm{fb}}{\gamma}$$

with $\Gamma_p = k_\mathrm{B}T_0\gamma_\mathrm{p}$ the thermal heating rate, Γ_rc the photon recoil rate and Γ_fb the heating rate due to the parametric feedback cooling. The photon recoil rate along the axis of polarization (in our case the x-axis) is given by [57]

$$\Gamma^i_\mathrm{rc} = \frac{k\sigma_\mathrm{scatt}I}{10mc\Omega_i}. \tag{3.26}$$

The recoil heating sets the ultimate limit for the mechanical losses and therefore also for the quantum cooperativity C_Q. In order to measure the mechanical losses, the particle is cooled to a low energy state $E_0 \ll E_\infty$ much colder than the equilibrium temperature. At a time $t = 0$ the feedback cooling is switched off ($\gamma_\mathrm{fb} = \Gamma_\mathrm{fb} = 0$) and the mean particle energy evolves according to equation 3.25

$$E(t) = E_\infty + (E_0 - E_\infty)e^{-\gamma t}. \tag{3.27}$$

For small damping and short times ($\gamma t \ll 1$) the time evolution can be Taylor expanded to

$$\begin{aligned} E(t) &= E_\infty - \gamma t(E_0 - E_\infty) + O(t^2) \\ &\underset{E_0 \ll E_\infty}{\approx} E_0 + \gamma E_\infty t \\ &= E_0 + \hbar\Omega_\mathrm{m}(\Gamma_\mathrm{p} + \Gamma_\mathrm{rc})t \end{aligned} \tag{3.28}$$

Equation 3.28 is a linear function in time and the mechanical losses $\Gamma = \Gamma_p + \Gamma_\mathrm{rc} = \gamma_\mathrm{p}\bar{n} + \Gamma_\mathrm{rc}$ are precisely the parameter required to estimate the quantum cooperativity C_Q.

3.2. Principles of Cavity Optomechanics with Levitated Particles

The first experiments on levitated cavity optomechanics demonstrated cavity cooling of an optically trapped silica particle [14] and cavity cooling of free silicon particles [83]. Later on, cavity cooling was demonstrated for charged particles levitated inside a Paul trap [119, 120] and also for rotational degrees of freedom of nanorods [84].

In this chapter I will briefly introduce the optomechanical concepts of cavity cooling and optomechanical induced transparency (OMIT) for levitated systems. A more detailed theoretical description can be found in the PhD thesis of Uros Delic [121] .

3.2.1. Linearisation of the Optomechanical Hamiltonian

The Hamiltonian of a harmonically trapped Rayleigh particle that is linearly coupled to a driven, single TEM00 cavity mode [5, 14, 79] is

$$\begin{aligned}\mathbf{H}_{\mathrm{tot}} = &-\hbar\omega_{\mathrm{cav}}(\mathbf{a}^\dagger\mathbf{a}+\frac{1}{2})+\frac{m\Omega_{\mathrm{m}}^2\mathbf{x}^2}{2}+\frac{\mathbf{p}^2}{2m}+\\ &+iE_1(\mathbf{a}^\dagger e^{-i\omega_{\mathrm{co}}t}-\mathbf{a}e^{i\omega_{\mathrm{co}}t})-\hbar\mathcal{U}(\mathbf{x})\mathbf{a}^\dagger\mathbf{a}\sin^2(k\mathbf{x})\end{aligned} \tag{3.29}$$

with $\mathbf{a}^\dagger(\mathbf{a})$ the creation (annihilation) operator of the cavity mode with frequency ω_{cav}, $\mathbf{x}(\mathbf{p})$ the displacement (momentum) operator of the levitated particle COM motion with frequency Ω_{m}, E_1 the cavity drive with a frequency ω_{co} and $\mathcal{U}(\mathbf{x}) = \frac{\omega_{\mathrm{cav}}\alpha}{2\varepsilon_0 V_{\mathrm{cav}}}(1+\mathbf{x}^2/x_{\mathrm{R}}^2) = \mathcal{U}_0(1+\mathbf{x}^2/x_{\mathrm{R}}^2)$ (α: particle polarizability, V_{cav}: cavity mode volume, x_{R} cavity mode Rayleigh length) the frequency shift of the cavity resonance due to the presence of a particle [14]. Note, that the Hamiltonian changes for bigger particles outside the Rayleigh regime [122]. The first three terms of equation 3.29 represent the energy of the TEM00 cavity mode and the potential and the kinetic energy of the COM motion, respectively. Note that in contrast to [5, 14] no cavity mode provides the optical trap, but the particle is held in place by an optical tweezer. The mechanical frequency Ω_{m} is therefore defined by the tweezer trapping mode (in our case along the x-direction of the tweezer and hence $\Omega_{\mathrm{m}} = \Omega_{\mathrm{x}}$). The fourth term describes the cavity drive and the last term describes the interaction between optics and mechanics. The Hamiltonian can be transformed into a reference frame rotating with the driving frequency ω_{co} by the transformation

$\mathbf{H} \to \mathbf{U}\mathbf{H}\mathbf{U}^\dagger - i\hbar\mathbf{U}\partial\mathbf{U}^\dagger/\partial t$ with $\mathbf{U} = e^{i\omega_{\mathrm{co}}\mathbf{a}^\dagger\mathbf{a}}$, yielding

$$\begin{aligned}\mathbf{H}_{\mathrm{tot}} = -\hbar\Delta\mathbf{a}^\dagger\mathbf{a} - \frac{1}{2}\hbar\omega_{\mathrm{C}} + \frac{m\Omega_{\mathrm{m}}^2\mathbf{x}^2}{2} + \frac{\mathbf{p}^2}{2m} + \\ + iE_1(\mathbf{a}^\dagger - \mathbf{a}) - \mathcal{U}(\mathbf{x})\mathbf{a}^\dagger\mathbf{a}\sin^2(k\mathbf{x})\end{aligned} \tag{3.30}$$

with the cavity detuning $\Delta = \omega_{\mathrm{cav}} - \omega_{\mathrm{co}}$. The COM motion is separated into mean displacement and small fluctuations around the mean value $\mathbf{x} = \bar{x} + \delta\mathbf{x}$. We focus on particle locations that exhibit linear coupling to the cavity field, i.e. where $\sin^2(k\mathbf{x}) \propto \delta\mathbf{x}$. Experimentally, this can be achieved by moving the tweezer relative to the cavity, see chapter 3.3.5. In theory, a particle couples linearly to the cavity mode if the mean displacement is an integer multiple m of $\lambda/8$ such that $\bar{x} = m\lambda/8$. The coupling is maximal at the cavity center $w(\lambda/8) \approx w_0$ with a dispersive frequency shift $\mathcal{U}(\bar{x} = \lambda/8) = \mathcal{U}_0$. The interaction Hamiltonian can be developed in a Taylor series around $\bar{x} = \lambda/8$

$$\begin{aligned}\mathbf{H}_{\mathrm{int}}(\frac{\lambda}{8} + \delta\mathbf{x}) &= -\mathcal{U}_0\mathbf{a}^\dagger\mathbf{a}\sin^2\left(k\frac{\lambda}{8} + k\delta\mathbf{x}\right) \\ &= -\mathcal{U}_0\mathbf{a}^\dagger\mathbf{a}\Big(\frac{1}{2} + k\delta\mathbf{x}\Big) + \mathcal{O}(\mathbf{x}^3).\end{aligned}$$

The first term represents a constant shift of the cavity resonance frequency and is compensated for by the locking scheme of the laser to the cavity. That leaves the interaction Hamiltonian to be

$$\mathbf{H}_{\mathrm{int}} = -k\mathcal{U}_0\mathbf{a}^\dagger\mathbf{a}\delta\mathbf{x} = -g_0\mathbf{a}^\dagger\mathbf{a}(\mathbf{b}^\dagger + \mathbf{b}) \tag{3.31}$$

with $\delta\mathbf{x} = x_{\mathrm{ZPF}}(\mathbf{b}^\dagger + \mathbf{b})$, $\mathbf{b}^\dagger(\mathbf{b})$ the phonon creation (annihilation) operator, $x_{\mathrm{ZPF}} = \sqrt{\hbar/(2m\Omega_{\mathrm{m}})}$ the zero-point fluctuations and $g_0 = k\mathcal{U}_0 x_{\mathrm{ZPF}}$ the single photon coupling. The single photon coupling quantifies the interaction between a single mechanical excitation, a phonon, and a single photon in the cavity. Equation 3.31 is the commonly used starting point in cavity optomechanics and is generic for most optomechanical systems [55]. For a strongly driven cavity a similar approach as above can be applied to the optical mode. The cavity field is decomposed into its mean amplitude $\langle\mathbf{a}\rangle = \alpha_{\mathrm{co}}$ and its fluctuations $\delta\mathbf{a}$. The interaction Hamiltonian becomes

$$\begin{aligned}\mathbf{H}_{\mathrm{int}} &= -g_0(\alpha_{\mathrm{co}}^2 + \alpha_{\mathrm{co}}\delta\mathbf{a}^\dagger + \alpha_{\mathrm{co}}\delta\mathbf{a} + \delta\mathbf{a}^\dagger\delta\mathbf{a})(\mathbf{b}^\dagger + \mathbf{b}) \\ &\approx -g_0\alpha_{\mathrm{co}}^2(\mathbf{b}^\dagger + \mathbf{b}) - g(\delta\mathbf{a}^\dagger + \delta\mathbf{a})(\mathbf{b}^\dagger + \mathbf{b})\end{aligned} \tag{3.32}$$

with $g = \alpha_{\mathrm{co}}g_0 = \sqrt{n_{\mathrm{co}}}g_0$ the effective optomechanical coupling strength, which scales with the square-root of number of photons inside the cavity. The first

term is a constant radiation pressure force causing a mean displacement of the mechanics. As the mean field $|\alpha_{\mathrm{co}}| \gg |\delta\mathbf{a}|$ is much bigger than the fluctuations the term quadratic in fluctuations is neglected. Combination of equation 3.29, 3.31 and 3.32 results in the linearised optomechanical Hamiltonian

$$\mathbf{H}_{\mathrm{tot}} = \hbar\Delta\delta\mathbf{a}^{\dagger}\delta\mathbf{a} + \hbar\Omega_{\mathrm{m}}\mathbf{b}^{\dagger}\mathbf{b} + \hbar g(\delta\mathbf{a}^{\dagger} + \delta\mathbf{a})(\mathbf{b}^{\dagger} + \mathbf{b}) \tag{3.33}$$

where we have dropped constant terms that are not relevant for the following considerations. At this level, an optomechanical system is comprised of two coupled harmonic oscillators: the levitated nanoparticle and the cavity mode coupled with an interaction rate g.

3.2.2. Optomechanical Cooling and Quantum Cooperativity

One of the main benefits of levitated cavity optomechanics is the ability to prepare quantum states of motion of solids at room temperature, essentially by laser-cooling of the COM motion into the ground state. The quantum theory of ground state cooling can be found in [123–125] and applies for weak coupling ($g < \kappa, \gamma$) and the sideband-resolved regime ($\Omega_{\mathrm{m}} > \kappa$). Experimentally, optomechanical cooling based on radiation pressure was first demonstrated for the vibrational mode of a doubly clamped free-standing mirror [126, 127] and for the radial breathing mode of a toroid microcavity [128]. The ground state of a vacuum-gap capacitor has been reached via cryogenic cooling [129] and via radiation pressure cooling in the microwave regime [20, 130]. The first optical ground state cooling was performed on the vibrational mode of a silicon nanobeam [21]. All these experiments were either performed in Helium cryostats or dilution refrigerators. The isolation of levitated systems should allow the ground state to be reached starting from room-temperature [5, 79, 80].

Depending on the detuning Δ in equation 3.33 three different interactions can be specifically tailored [55]. Rewriting the light and mechanics operators with an explicit time dependence $\delta\mathbf{a} \to \delta\mathbf{a}_0 e^{-i\Delta t}$ and $\mathbf{b} \to \mathbf{b}_0 e^{i\Omega_{\mathrm{m}} t}$ allows for an intuitive understanding. The interaction Hamiltonian then reads

$$\begin{aligned}\mathbf{H}_{\mathrm{int}} &= \hbar g(\delta\mathbf{a}^{\dagger} + \delta\mathbf{a})(\mathbf{b}^{\dagger} + \mathbf{b}) \\ &= \hbar g\Big(\delta\mathbf{a}_0^{\dagger}\mathbf{b}_0^{\dagger} e^{-it(\Omega_{\mathrm{m}}-\Delta)} + \delta\mathbf{a}_0\mathbf{b}_0 e^{it(\Omega_{\mathrm{m}}-\Delta)} + \\ &+ \delta\mathbf{a}_0^{\dagger}\mathbf{b}_0 e^{it(\Omega_{\mathrm{m}}+\Delta)} + \delta\mathbf{a}_0\mathbf{b}_0^{\dagger} e^{-it(\Omega_{\mathrm{m}}+\Delta)}\Big).\end{aligned} \tag{3.34}$$

For a red-detuned cavity drive, i.e. detuned by the mechanical frequency $\Delta = -\Omega_{\mathrm{m}}$, the beamsplitter interaction prevails. The terms $\delta\mathbf{a}_0^{\dagger}\mathbf{b}_0 + \delta\mathbf{a}_0\mathbf{b}_0^{\dagger}$ are resonantly enhanced by the cavity and the terms $\delta\mathbf{a}_0^{\dagger}\mathbf{b}_0^{\dagger} + \delta\mathbf{a}_0\mathbf{b}_0$ rotate at twice the mechanical frequency $2\Omega_{\mathrm{m}}$. If the system is in the sideband-resolved

regime, the components rotating at twice the mechanical frequency are strongly suppressed (rotating wave approximation) [55]. The beamsplitter represents a swap of excitations from mechanics to optics and vice versa. If the optical state is in its ground state (shot-noise limited) no excitation from the optics will be swapped on the mechanical state, but excitations from the mechanics are swapped onto the optical state. For a finite lifetime of the optical state in the cavity $\kappa > g$ the optical excitations will leak out of the cavity before they are transferred back to the mechanics (Rabi-oscillations). The mechanical excitations are dissipated via the optical field of the cavity, thereby effectively cooling the mechanical state.

There exist alternative pictures to understand this mechanism, e.g. the scattering picture [55]. The motion of the nanoparticle at Ω_m inside the cavity field scatters photons into the optical Stokes and anti-Stokes sidebands at frequencies $\omega_\mathrm{co} - \Omega_\mathrm{m}$ and $\omega_\mathrm{co} + \Omega_\mathrm{m}$, respectively. During this process, photons with initial energy of $E = \hbar\omega_\mathrm{co}$ gain (loose) one mechanical quanta of energy $\hbar\Omega_\mathrm{m}$ due to inelastic scattering. If the cavity pump is red-detuned, i.e. $\Delta < 0$, the cavity envelope suppresses the Stokes process and amplifies the anti-Stokes process such that more anti-Stokes photons with an energy of $E = \hbar(\omega_\mathrm{co} + \Omega_\mathrm{m})$ are created than Stokes photons with $E = \hbar(\omega_\mathrm{co} - \Omega_\mathrm{m})$. This scattering anti-symmetry transfers energy from the mechanical motion into the cavity field and hence, cools the oscillator.

The efficiency of this cooling process depends on the optomechanical interaction g, the cavity lifetime κ and the sideband resolution parameter $4\Omega_\mathrm{m}/\kappa$. The sideband resolution describes how well the inverse process (simultaneous creation of mechanical and optical excitations) is suppressed. In addition, the mechanical system couples to the thermal environment via collisions of the particle with surrounding gas molecules $\gamma_\mathrm{p}\bar{n}_\mathrm{th}$ and via recoil heating due to the quantum nature of the trapping field Γ_rc, see chapter 3.1.5. The combined heating rate of both mechanisms is $\Gamma = \gamma_\mathrm{p}\bar{n}_\mathrm{th} + \Gamma_\mathrm{rc}$ and the final occupation of the mechanical state in the sideband-resolved limit is given by [123, 124]

$$\bar{n}_\mathrm{min} = \frac{1}{\gamma_\mathrm{opt} + \gamma_\mathrm{p} + \gamma_\mathrm{rad}} \left[\gamma_\mathrm{opt} \left(\frac{\kappa}{4\Omega_\mathrm{m}} \right)^2 + \Gamma \right] \tag{3.35}$$

with $\gamma_\mathrm{opt} = 4g^2/\kappa$ the optomechanical damping rate for a detuning of $\Delta = -\Omega_\mathrm{m}$ and $\gamma_\mathrm{rad} = \frac{4\sigma_\mathrm{scatt} I}{5mc^2}$ the radiation damping due to the motion of the particle inside a laser field [118]. For typical experimental parameters (particle radius of $a = 75$ nm, intensity in the trap $I \approx 10^{12}$ W/m^2) the radiation damping is $\gamma_\mathrm{rad} \approx 0.1$ mHz. For strong optomechanical interaction $\gamma_\mathrm{opt} \gg \gamma_\mathrm{p}, \gamma_\mathrm{rad}$ the denominator in equation 3.35 can be approximated with γ_opt. In the absence of mechanical heating $\Gamma = 0$ the final occupation number in the sideband-resolved limit is $\bar{n}_0 = (\frac{\kappa}{4\Omega_\mathrm{m}})^2 \ll 1$. Taking into account heating (neglecting

other technical noise sources) results in the minimal achievable occupation number

$$\begin{aligned}\bar{n}_{\mathrm{min}} &\approx \frac{1}{\gamma_{\mathrm{opt}}}(\gamma_{\mathrm{opt}}\bar{n}_0 + \Gamma) = \bar{n}_0 + \frac{\kappa\Gamma}{4g^2} \\ &= \bar{n}_0 + \frac{1}{C_Q}.\end{aligned} \tag{3.36}$$

Here the quantum cooperativity is defined as $C_Q = 4g^2/(\kappa\Gamma)$. Note that, in contrast to clamped optomechanical systems, photon recoil heating has to be taken into account for the quantum cooperativity, i.e. $\Gamma = \gamma_{\mathrm{p}}\bar{n}_{\mathrm{th}} + \Gamma_{\mathrm{rc}}$. In order to reach the quantum ground state of motion it is evident that $\bar{n}_0 + 1/C_Q$ needs to be smaller than one, which requires both, sideband-resolution and strong quantum cooperativity $C_Q > 1$.

3.2.3. Optomechanically Induced Transparency

Optomechanically induced transparency (OMIT) is an interference effect of the cavity-optomechanical system in presence of a strong optical pump and a weak probe tone. The interaction between a levitated nanoparticle coupled to the cavity mode renders the transmission properties of the cavity. The effect is in close analogy to electrically induced transparency (EIT) [131, 132] and was demonstrated using optomechanical crystals [133] and toroidal microcavities [134].

Let us consider a levitated particle coupled to a sideband-resolved cavity, as described by equation 3.33. The optomechanical cavity is driven with a strong control mode $\alpha_\Delta e^{-i\Delta t}$ at the mechanical frequency $\Delta = -\Omega_{\mathrm{m}}$ (indicated by the red arrow in figure 3.9 a)) with respect to the cavity resonance at ω_{cav}. The particle oscillates at its resonance frequency Ω_{m} and scatters photons from the control mode into the anti-Stokes and Stokes sideband, respectively (as indicated by the two red Lorentzian peaks in figure 3.9 a)). The frequency of the Stokes photons is off-resonant by $\delta\omega = -2\Omega_{\mathrm{m}}$ with respect to the cavity resonance in contrast to the anti-Stokes photons, which are resonant at $\delta\omega = 0$. The sideband-resolved cavity (black, dashed line) suppresses the Stokes scattering process while resonantly enhancing the anti-Stokes process. A second, weak probe mode $\alpha_\delta e^{-i\delta t}$ (blue arrow) detuned by the frequency δ with respect to the cavity is used to probe the optomechanical interaction caused by the control mode. For $\delta \approx 0$, the probe beam destructively interferes with the anti-Stokes photons from the pump beam. Figure 3.9 b) shows the transmission characteristics of an OMIT signal as a function of difference frequency $\delta - \Delta$ between pump and probe beam. The dip appearing around the mechanical

frequency Ω_m is called the "transparency window" and is an unambiguously feature of the coherent interaction between COM motion of the particle, pump and probe beam. The transmission T of the optomechanical cavity in presence

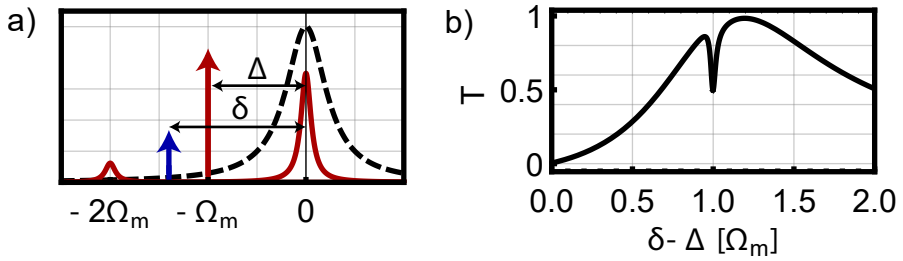

Figure 3.9.: a) The COM motion of the levitated particle scatters light of the drive laser (red arrow) into the Stokes and anti-Stokes sideband. For a red-detuned drive with $\Delta = -\Omega_m$ the Stokes sideband is suppressed by the cavity envelope (dashed black line) and the anti-Stokes sideband is resonant with the cavity. A weak probe mode at frequency δ (blue arrow) is used to scan the cavity resonance. b) A typical OMIT response T as a function of $\delta - \Delta$, the optomechanical interaction gives rise to the transparency window around the mechanical frequency.

of the particle and the pump as seen by the probe beam is given by [55, 134]

$$T = \left| 1 - \frac{\kappa}{2} \frac{\chi_{opt}(\delta)}{1 + g^2 \chi_m(\delta) \chi_{opt}(\delta)} \right|^2 \tag{3.37}$$

with the mechanical susceptibility $\chi(\delta)_m^{-1} = -i(\delta - \Omega_m) + \gamma/2$, the optical susceptibility $\chi_{opt}(\delta)^{-1} = -i(\delta + \Delta) + \kappa/2$ and the detuning between control mode and cavity mode $\Delta = \omega_{co} - \omega_{cav}$. For $\Delta = -\Omega_m$, the width of the transparency window is given by [55]

$$\gamma_{OMIT} = \gamma_p + \frac{4g^2}{\kappa} = \gamma_p + \gamma_{opt}. \tag{3.38}$$

In the following chapter OMIT will be used to measure the width of the transparency window in order to estimate the cooperativity of the levitated optomechanical system. The mechanical heating rate Γ, which is also required to estimate C_Q, is measured independently with relaxation measurements, see chapter 3.1.5.

3.3. Combination of a Tweezer and a Macroscopic Fabry-Pérot Cavity

The cavity optomechanical setup described here is based on [14] and the optical tweezer design is based on [101]. Both systems are combined inside the same vacuum chamber such that the levitated particle inside the tweezer is coupled to the fundamental cavity mode. The cavity optomechanical setup and the tweezer are introduced independently in the first two sections and the remaining parts of this chapter are devoted to the combination of both systems.

3.3.1. Cavity Optomechanical Setup

The experimental implementation of the cavity optomechanics part is divided into three parts: The main setup, the control mode generation and the homodyne read-out of the particle motion.

The Main Setup

Figure 3.10 shows a schematic drawing of the experiment. A $\lambda = 1064$ nm laser (Innolight/Coherent: Mephisto) is locked onto a Fabry-Pérot cavity (OMC, for optomechanical) with a Pound-Drever-Hall locking scheme [135]. A free-space electro-optical modulator (not shown in figure 3.10, between polarizing beamsplitter PBS2 and PBS3) generates sidebands for the lock. The OMC is in a near-confocal configuration. Both mirrors have a radius of curvature of $R = 1$ cm, the cavity has a length of $l_{\mathrm{cav}} = 10.7$ mm, a free spectral range of FSR $= 14$ GHz and a finesse of $F \approx 70,000$. The lock loop stabilizes the laser to the fundamental TEM00 mode of the resonator with a waist of $w_0 = 41$ μm. This mode is referred to as locking mode (LM). The cavity is inside a vacuum chamber which is connected to a scroll pump (Edwards: nXDS) and a turbo pump (Edwards: nExt300). The vacuum chamber is also connected to a ultrasonic nebulizer (Omron: MicroAir U22) providing a source for airborne nanoparticles [65]. A more detailed description about the mounting and particle loading follows in chapter 3.3.3 and 3.3.4. The base pressure of the vacuum system is $p \approx 6 \times 10^{-7}$ mbar, limited by outgasing of the elements inside the vacuum chamber. A fraction of the LM is split off at PBS1 and coupled into a single mode fiber (SMF). This light is used to generate the optomechanical control mode. A second fraction of the LM is separated at PBS2 and serves as a local oscillator (LO) for the homodyne read-out of the transmitted cavity field. After the vacuum chamber, in transmission of the OM cavity, the locking beam and the orthogonally polarized control

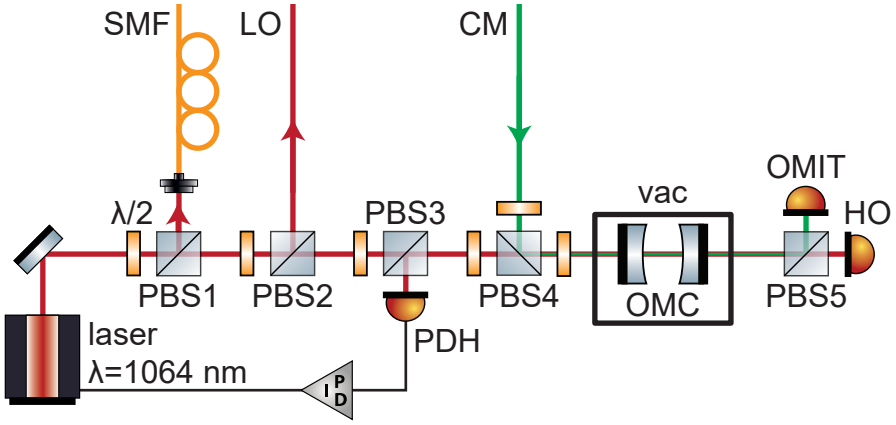

Figure 3.10.: A $\lambda = 1064$ nm laser is locked to a Fabry-Pérot cavity (OMC) inside a vacuum chamber (vac) with a Pound-Drever-Hall locking scheme (PDH: Pound-Drever-Hall detector, sideband generation not shown). A fraction of the locked laser is separated at a polarizing beamsplitter (PBS1) and coupled into a single mode fiber (SMF). It is used to generate the control mode (CM) which is orthogonally polarized and superimposed with the locking beam on PBS4 before the OMC. A second fraction is split at PBS2 and used as local oscillator (LO) for the homodyne detection (HO) in transmission of the OMC. The orthogonal control mode is separated from the locking beam on PBS5 and used for optomechanical induced transparency measurements (OMIT).

mode are separated at PBS5. The transmitted light is used for homodyne detection (HO) and the light reflected will be used for OMIT measurements (Thorlabs: SM05PD4A photodiode in combination with Femto: DHPCA-S current amplifier).

The Optomechanical Control Mode Generation

Figure 3.11 shows a schematic of the control-mode generation. Light in reflection of PBS1, see figure 3.10, is coupled into a SMF which is connected to a fiber-based electro-optical modulator (EOM, EOSpace: PM-0K5-20-PFA-PFA-106). A microwave signal generator (FG, Rhode&Schwarz: SMF100A) drives the EOM with a frequency $\nu_{\mathrm{FG}} = \mathrm{FSR} + \Delta$ such that the light after the EOM consists of three frequency components: the unmodulated carrier ν_{cav}, the upper sideband $\nu_{\mathrm{cav}} + \mathrm{FSR} + \Delta$ and the lower sideband $\nu_{\mathrm{cav}} - \mathrm{FSR} - \Delta$. For the optomechanical control mode only one of the two sidebands is required.

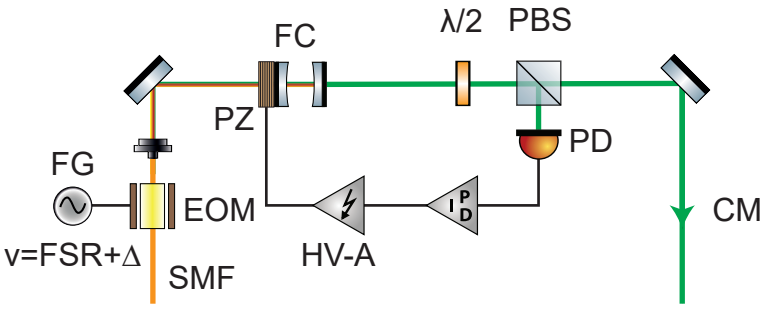

Figure 3.11.: Optomechanical control mode generation: A fiber based electro-optical modulator (EOM) is used to generate sidebands at $\nu = \nu_{\mathrm{cav}} \pm (\mathrm{FSR} + \Delta)$ of the laser resonant with the OMC. A free-space Fabry-Pérot cavity (FC) is used as a filter to reject the carrier frequency and one of the two sidebands generated by the EOM. A photodiode (PD) in combination with a PID controller and a high-voltage amplifier (HVA) are used to change the cavity length with a piezo (PZ) such that only one sideband of the laser is transmitted.

A low-finesse Fabry-Pérot resonator (FC) is used to reject the unwanted sideband and the unwanted carrier. The length of the FC and hence its resonance frequency ν_{FC}, can be changed with a piezo (PZ). The FC has a linewidth of $\kappa_{\mathrm{FC}} \approx 2\pi \times 100$ MHz, sufficiently narrow to reject the two unwanted frequencies. The cavity is stabilized with a "side-of-the-peak" locking scheme. Initially, the filtering cavity resonance frequency is tuned such that the upper sideband coincides with the linear slope of the cavity envelope. A photodiode (PD) detects a fraction of the transmitted light and provides an error signal for a software based feedback loop (LabView: PID and Fuzzy Logic Toolkit). The control signal from the PID is amplified with a high-voltage amplifier (HV-A, Piezomechanik GmbH: SVR 150/3) and connected to the piezo (PZ) to stabilize the cavity length such that the power measured on the PD is constant. Hence, the light after the PBS has a single frequency component at $\nu_{\mathrm{co}} = \nu_{\mathrm{cav}} + \mathrm{FSR} + \Delta$ and is referred to as control mode (CM) from now on. For $\Delta = 0$ the light would excite another TEM00 mode of the OMC. The detuning Δ can now be chosen arbitrarily for optomechanical control. Note that the microwave signal generator has a frequency modulation option. If enabled, the frequency ν_{FG} that creates the sidebands in the EOM is modulated by an external frequency δ and creates additional sidebands at $\nu_{\mathrm{FG}} \pm \delta$. For small external frequencies $\delta \ll \kappa_{\mathrm{FC}}$ the modulation will create optical sidebands of the CM mode which will be transmitted by the filtering cavity. That means

that the light leaking out of the filtering cavity has three frequency components: the CM mode at $\nu_{\mathrm{cav}} + \mathrm{FSR} + \Delta$, the lower sideband of the CM mode $\nu_{\mathrm{cav}} + FSR + \Delta - \delta$ and the upper sideband at $\nu_{\mathrm{cav}} + FSR + \Delta + \delta$. The additional sidebands will be used for optomechanical induced transparency measurements.

The Homodyne Read-Out

The homodyne read-out scheme is shown in figure 3.12. Light of the locking mode leaking out of the OMC (signal beam) is superimposed with the local oscillator (LO) at PBS2. The phase of the LO with respect to the signal beam is controlled with a mirror glued on a piezo stack (PZ-M). The LO is reflected at PBS1, propagates through a quarter waveplate ($\lambda/4$), is reflected by the PZ-M and propagates again through the quarter waveplate. Passing it twice effectively rotates the polarization of the LO by 90° degrees and therefore, the LO is transmitted at PBS1 and superimposed with the signal beam at PBS2. Typically, homodyne detection schemes use a 50:50 beamsplitter instead of

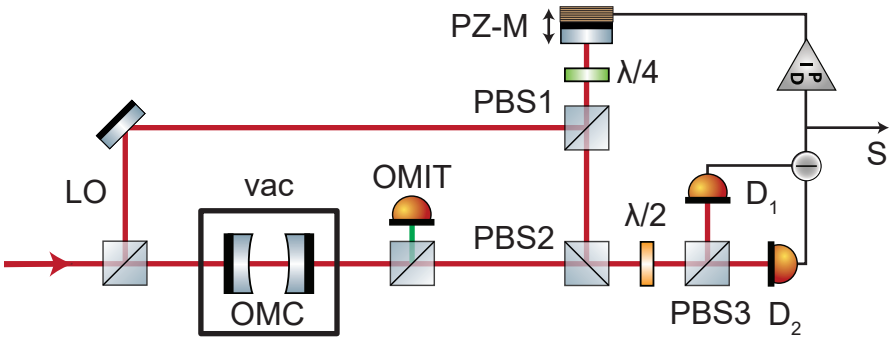

Figure 3.12.: Homodyne detection scheme: Light leaking out of the OMC is superimposed with a local oscillator beam (LO) at the polarizing beamsplitter (PBS2). To interfere both beams at PBS3, a half waveplate ($\lambda/2$) is used to rotate the polarization by 45° degrees. Two photodiodes D_1 and D_2 detect the transmitted and reflected port of PBS3. A mirror glued on a piezo stack (PZ-M) allows to control the phase of the LO. The difference signal between both photodiodes is used to stabilize the homodyne read-out with a PID feedback loop driving the PZ-M. The LO is first reflected at PBS1, reflected by the PZ-M and passes a quarter waveplate $\lambda/4$ twice such that its polarization is rotated by 90° degrees and transmitted at PBS1.

a polarizing beamsplitter. Here, the combination of PBS-$\lambda/2$-PBS has the same effect as a 50:50 beamsplitter. The electric field after PBS2 and the half waveplate is

$$E_{\lambda/2} = -\frac{i}{\sqrt{2}}(E_{\mathrm{LO}} + E_{\mathrm{SIG}})|H\rangle - \frac{i}{\sqrt{2}}(E_{\mathrm{LO}} - E_{\mathrm{SIG}})|V\rangle \tag{3.39}$$

with E_{LO} (E_{SIG}) the electric field of the local oscillator (signal beam) and $|H\rangle(|V\rangle)$ the basis vector for horizontal (vertical) polarization. The intensity measured at the homodyne photodiodes D_1 and D_2 is

$$I_{D_{1/2}} \propto \frac{1}{2}|E_{\mathrm{LO}} \pm E_{\mathrm{SIG}}|^2. \tag{3.40}$$

Starting from here, this is a standard homodyne detection scheme which is described elsewhere [136]. A balanced, amplified photodiode (Thorlabs: PDB420-C) is used for homodyne detection. A PID controller (Toptica: PID110) is used to lock the PZ-M to the desired homodyne phase.

3.3.2. Tweezer Setup

The optical tweezer setup consists of three parts: Beam preparation, feedback electronics, trapping and read-out, which is described in detail below:

Trapping and Read-Out

Figure 3.13 shows a schematic drawing of the trapping and read-out part of the tweezer setup. The trapping laser (red) and an orthogonally polarized, $\nu = 82$ MHz frequency shifted (with respect to the trapping laser) feedback laser (green) are delivered by a single mode fiber (SMF, see figure 3.14), enter the vacuum chamber (vac) and are aligned onto a long working distance WD = 3.4 mm, high NA = 0.8 microscope objective (MO, Olympus: LMPL 100x IR). The tightly focused laser beam forms the optical trap for nanoparticles. A collimation lens (CL, Thorlabs: A260-C) with a focal length of $f = 15$ mm is used to collect scattered light from the particle for position read-out. A quarter ($\lambda/4$) and a half ($\lambda/2$) waveplate in combination with a Glan-Laser polarizer (GLP, Thorlabs: GL10-C) are used to separate feedback and trapping laser after leaving the vacuum chamber. The beamsplitters PBS1 and PBS2 divide the beam into three parts for the three-dimensional read-out of the COM motion, as explained in chapter 3.1.2. Along the x-direction the mode is split by a D-shaped mirror (DS, Thorlabs: BBD1-E03) into two equal halves and each part is sent to the photodiode of a balanced photodetector (X_1 and X_2, Thorlabs: PDB420C-AC). The detector returns the difference signal

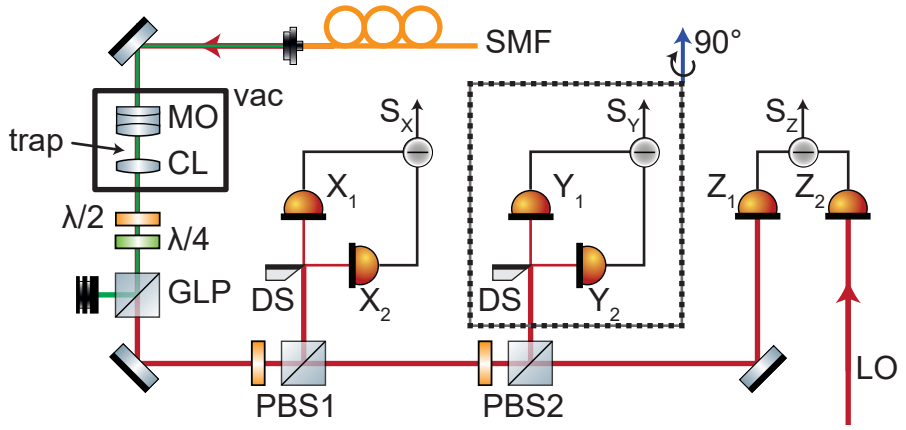

Figure 3.13.: The feedback (green) and trapping (red) laser enter the vacuum chamber (vac) from a single mode fiber (SMF). Inside the vacuum chamber is a high NA microscope objective (MO) and a collimation lens (CL) to form the optical trap and collect light for the read-out. A Glan-Laser polarizer (GLP) in combination with a half ($\lambda/2$) and a quarter ($\lambda/4$) waveplate are used to separate feedback and trapping laser. The trapping laser is split on PBS1 and PBS2 into three parts. Each part is used to detect the COM motion along one spatial direction. For radial read-out the mode is split into two halves with a D-shaped mirror (DS) and each half is detected separately with a photodiode (X_1 and X_2 for the x read-out and Y_1 and Y_2 for the y read-out). Note that the y read-out is rotated by 90° degrees with respect to the x read-out, along the axis indicated by the blue arrow. For axial read-out (z-direction) the signal beam is detected with photodiode Z_1 and the (LO) is detected with Z_2. The difference signal between each detector pair is proportional to its corresponding COM motion, see chapter 3.1.2.

S_x between the two diodes which is, according to equation 3.20, proportional to the particle displacement along the x-direction. The read-out along the y-direction is the same except the D-shaped mirror is rotated by 90° degrees with respect to the blue arrow, to detect the motion perpendicular to x. The third fraction is sent to the photodiode Z_1 of a balanced photodetector (Thorlabs: PDB420C-AC) and the same optical power from the trapping laser (LO), separated before interaction with the particle, is sent on the second diode Z_2. The difference signal S_z is proportional to the particle COM motion along the z-direction, see equation 3.19.

Tweezer Beam Preparation and Feedback Electronics

Figure 3.14 shows a drawing of the tweezer beam preparation setup and a schematic circuit diagram of the feedback electronics. Roughly $P \approx 10$ mW from a free-running Innolight/Coherent Mephisto laser (not shown in figure 3.14) are used to seed a fiber amplifier (Nufern: NUA-1064-PB-0005-B3). The frequency of the free-running laser is chosen far off-resonant with respect to the OMC resonance frequency ω_{cav} to avoid pumping the cavity via the tweezer. The output of the fiber amplifier is split into three parts with PBS1 and PBS2. The light transmitted at both, PBS1 and PBS2 is coupled into a single mode fiber and forms the optical trap in the optical tweezer setup. The fraction of light reflected at PBS2 is sent to the tweezer read-out and is used as local oscillator (LO) for z-detection. The light reflected at PBS1 passes an acousto-optical modulator (AOM, IntraAction Corp: ATM-804DA6M) which is driven by an DFE-804A4 dual channel frequency synthesizer (IntraAction Corp, only one channel is used). The first diffraction order is shifted by $\nu = 82$ MHz, is orthogonally polarized (green) with an additional half waveplate (not shown in figure 3.14) with respect to the trapping laser (red) and also coupled into the SMF via PBS3. This mode is used for parametric feedback cooling. The electronic feedback signal is sent into the modulation input of the AOM driver and results in an amplitude modulation of the feedback laser. For parametric feedback cooling, the spring constant needs to be modulated by twice the mechanical frequency. The optical potential of the feedback laser adds to the optical potential of the trapping laser. By modulating the intensity of the feedback laser the combined optical potential is modulated and hence, the spring constant of the levitated nanoparticle. Without loss of generality the signal processing is explained for the x-direction. In a first step the signal is bandpass filtered (HP and LP) around the mechanical frequency Ω_{x} to suppress technical noise (low frequency acoustical noise and noise peaks introduced by the fiber amplifier) and remnants of the other mechanical modes present due to imperfect isolation of the read-out. After filtering, the signal is squared (SQ) an a phase shift (ϕ_x) is applied to compensate for unwanted phase shifts introduced by the high- and lowpass filter and by the squaring circuit. This is done for each spatial direction independently and all three signals are added with an summing amplifier (S). In a last step the signal passes a switch (SW, Mini-Circuits: ZASWA-2-50DR+) which is electronically controlled and used to turn feedback cooling off or on.

In the beginning of the experiment we started with parametric feedback cooling along the axial direction only and used self-made analogue circuits, inspired by the PhD thesis of Jan Gieseler [111]. The circuit consisted of bandpass filter, see appendix A.1, with a center frequency of Ω_{z} to reject tech-

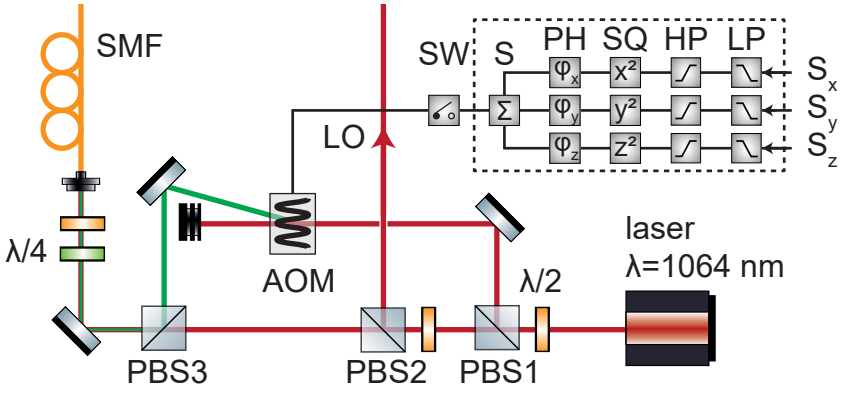

Figure 3.14.: Light from a fiber amplifier (laser $\lambda = 1064$ nm) is split into three parts at PBS1 and PBS2. The light transmitted at PBS2 is used for optical trapping and is coupled into a single mode fiber (SMF). Light reflected at PBS2 is sent to the read-out and serves as local oscillator (LO). Light reflected at PBS1 is sent through an acousto-optical modulator (AOM) and the first diffraction order is superimposed with the trapping laser at PBS3 and also coupled into the SMF. The optical power inside the first diffraction order is modulated by a signal from the feedback logic (dashed box). The feedback logic consists of a series of functions applied to the read-out signals in order to modulate the trap frequency for parametric feedback cooling (SW: switch, S: summing amplifier, PH: phase shift, SQ: squaring, HP: high-pass filter, LP: low-pass filter, S_i read-out signal along the i-axis).

nical noise peaks from the fiber amplifier and low frequency noise in the axial read-out. In a second step the signal was phase shifted, see appendix A.4, to compensate the delay introduced by the bandpass filter and the squaring circuit. For squaring, the circuit displayed in figure 26 of the AD734 (analogue multiplier) specification sheet [137] was used in order to generate the modulation signal at $2\Omega_z$. And in a last step, a variable gain amplifier, see appendix A.3, allowed for adjustment of the overall gain of the feedback signal. Nowadays, one phase-locked loop (PLL, Zurich Instruments: HF2LI) is used for each direction of motion. Instead of filtering and squaring the read-out signal, a PLL uses an internal PID controller in combination with a phase detector to lock a reference signal to the oscillation frequency at its input. The PLL is configured to output the second harmonic of the locked reference oscillator with an adjustable phase. The signals along each direction can be internally

added and are sent to the switch. The components inside the dashed line of figure 3.14 are all combined inside the three PLLs.

3.3.3. Mounting and Mirror Cutting

On of the main challenges of combining an optical tweezer with the Fabry-Pérot cavity from [14] is illustrated in figure 3.15. Typical available substrate for

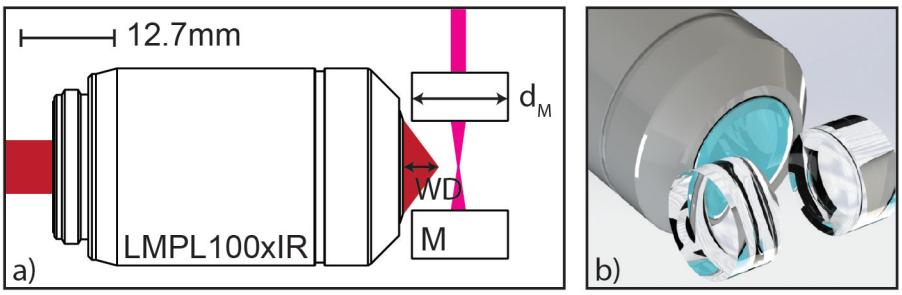

Figure 3.15.: Working distance versus substrate diameter: True-to-scale drawing of the Olympus LMPL100xIR microscope objective and the two mirrors (M) forming the Fabry-Pérot cavity. The drawing a) is a top view of the rendered picture b). The optical mode of the cavity (pink) and of the tweezer (red) are for illustration purpose only. The working distance (WD) of the microscope objective is not long enough to overlap the focus of the tweezer with the cavity mode as long as WD $< d_{\mathrm{M}}/2$.

cavity mirrors with a radius of curvature of $R = 1$ cm are only 1/2" or larger. The availability of long working distance, high numerical aperture lenses for the near-infrared is also limited. The only commercially off-the-shelf available lens complying our requirements is an Olympus LMPL100xIR microscope objective with a working distance of WD = 3.4 mm. As illustrated in figure 3.15 a), this working distance is too short to laterally reach the cavity axis and hence, not long enough to position a particle trapped with the microscope objective inside the mode of the cavity.

The waist of the TEM00 mode inside the cavity is described by the waist function $w(z) = w_0\sqrt{1-(z/\mathrm{z_R})^2}$, with $w_0 = 41$ μm and $\mathrm{z_R}$ the cavity Rayleigh length. For a cavity length of $l_{\mathrm{cav}} = 10.7$ mm, the waist of the cavity mode on the mirror is $w(l_{\mathrm{cav}}/2) = 61$ μm. This means that most of the mirror surface is not used to form the cavity mode. The problem was addressed in a collaboration with the group of Professor Martin Weitz at University of Bonn (especially Tobias Damm and the mechanical workshop). Due to their work

on optical microcavities [138], they have a long-standing experience in cutting high quality mirrors without degrading the optical quality. An initially 12.7 mm diameter mirror was cut to 4 mm wide strip, as shown in figure 3.16 a), which corresponds to 30 times the mode size on the mirror and hence, clipping losses are negligible. Now, the objective can be laterally closer to the cavity axis and a particle trapped in the tweezer can be positioned inside the cavity mode.

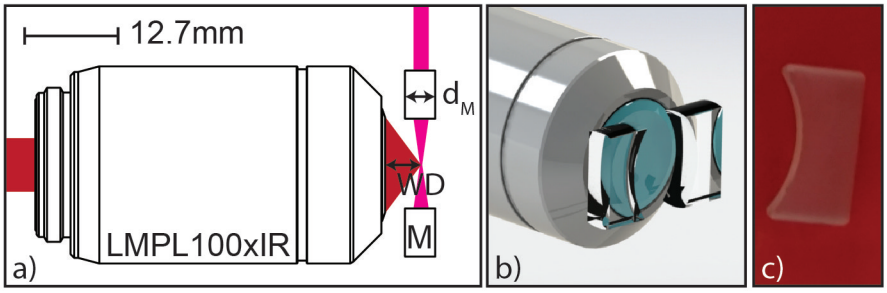

Figure 3.16.: a) True-to-scale drawing of the Olympus LMPL100xIR microscope objective and the two cut mirrors pieces (M) forming the Fabry-Pérot cavity. Due to the reduced width of the cavity mirrors the working distance of the microscope objective is long enough to overlap the tweezer trap with the cavity mode. b) Rendered picture of drawing shown in a). c) Photograph of one cut cavity mirror.

Figure 3.17 shows drawings of how cavity mirrors and tweezer are mounted. Part a) shows an aluminium metal mount on which the two cut cavity mirrors are glued. The groove along the horizontal direction is used to pump the cavity from one side (red arrow) and used for collection of the light leaking out of the cavity from the other side. The hole in the middle of the aluminium part is used to insert the collimation lens for the read-out of the tweezer. Part b) is a top view of the combined system of tweezer and cavity. The surface of cavity mount and mirrors shown in part a) are pointed towards the front face of the microscope objective. The collimation lens used for collection of the tweezer light is glued onto an Invar tube and is positioned through the hole in the cavity mirror mount (see part a)). This way of mounting the optical components allows trapping of a nanoparticle with the microscope objective and positioning it into the TEM00 mode of the cavity. The collimation lens is used for read-out of the particle motion. Part c) shows a side view of the cavity and tweezer mounting. The microscope objective is mounted onto a vacuum compatible, triaxial stepper motor (Mechonics: MX35) which is used to align the tweezer trap with respect to the cavity mode (one cavity mirror is indicated

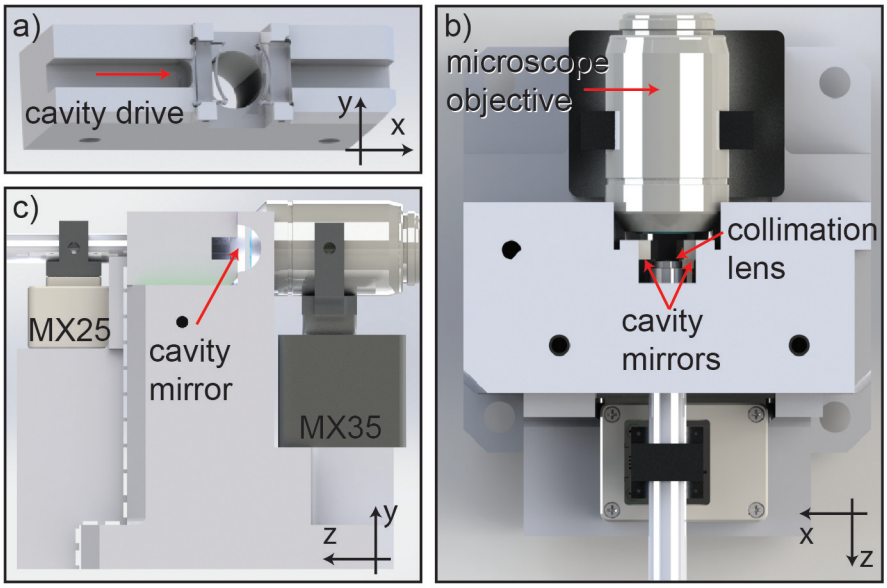

Figure 3.17.: Cavity and Tweezer Combination (black arrows indicate COM directions): a) Drawing of the cavity mirror mount. The cavity (two mirrors glued on aluminium mount) is driven via the left groove (red arrow) and the right groove enables detection of the light leaking out of the cavity. b) Top view of the microscope objective, the collimation lens mounted on an Invar tube and cavity in an assembled state. c) Side view: The microscope objective and the collimation lens tube are mounted on triaxial positioners. The red arrow indicates one cavity mirror

by an arrow). The collimation lens tube with the collimation lens is mounted onto another vacuum compatible, triaxial stepper motor (Mechonics: MX25). After alignment of the microscope objective with respect to the cavity mode, the MX25 is used to align the collimation lens with respect to the microscope objective.

3.3.4. Particle Loading and Trapping

Initial loading of particles into the combined tweezer-cavity experiment is a more complicated process compared to loading the HCPCF setup or loading the cavity-only experiment [14]. The focal volume of the microscope objective is on the order of $V_{\mathrm{foc}} = w_x \times w_y \times \mathrm{z_R} \approx 1\ \mu\mathrm{m}^3$, compared to $V_{\mathrm{foc}} \approx 600\ \mu\mathrm{m}^3$ at the HCPCF entrance and $V_{\mathrm{cav}} \approx 2.5 \times 10^7\ \mu\mathrm{m}^3$ for trapping in a cavity. As the trapping volume of the tweezer is significantly smaller than in the other two

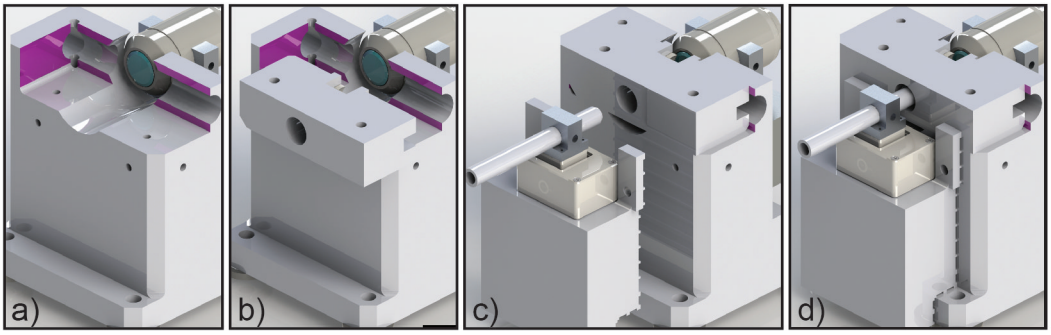

Figure 3.18.: Cavity insertion procedure: After a particle is initially trapped in the tweezer a) the cavity is inserted into the main aluminium block b). The aluminium piece on which the MX25 is mounted including collimation lens and collimation lens tube is laced into the hole of the cavity mirror holder and screwed into the main aluminium block c) & d).

cases, a higher concentration of nanoparticles is required to trap a particle. The particles are initially launched in the same way as described in chapter 2.2.5. An Omron MicroAir U22 ultrasonic nebulizer is used to nebulize a solution of Isopropanol and silica nanoparticles with a radius of $a = 71.5$ nm (Microparticles GmbH: $SIO_2 - F - 0.15$). The airborne particles are delivered close to the microscope objective via an inlet in the vacuum chamber. The ideal mass concentration between nanoparticles and solvent for trapping a particle in the tweezer was found heuristically to be 10^{-4}. However, this mass concentration is too high when the cavity is present, since initial loading of the tweezer would contaminate the high quality optical coatings of the cavity mirrors (we saw a reduction in finesse from $200,000$ to below $40,000$ from a single attempt!). This is the main reason for the modular design of cavity and collimation lens mount. In order to prevent degradation of the optical coating, the cavity is removed from the vacuum chamber before loading a particle into the tweezer.

The loading procedure happens in the following steps (figure 3.18). Step a): The cavity is removed from the vacuum chamber. In order to make this process as efficient as possible there is a CF quick access door with 10 cm diameter and viewport (Vacom: QAD100BK-AL-304) to remove the collimation lens including the MX25 stage and the cavity. The vacuum chamber is closed and evacuated to a pressure of roughly $p \approx 10$ mbar. Then, airborne nanoparticles from the ultrasonic nebulizer are sucked into the vacuum chamber until a particle occupies the tweezer trap. The trap is monitored with a CCD camera mounted on top of the vacuum chamber. Once a particle is trapped, the

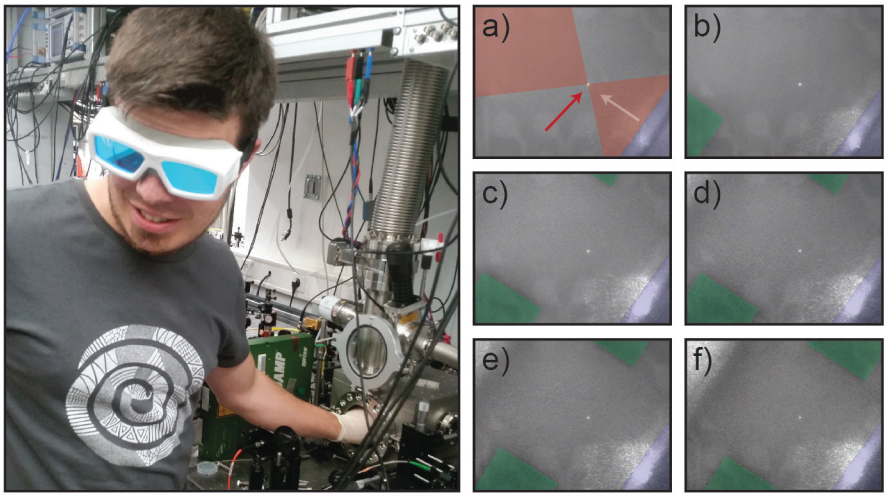

Figure 3.19.: The brave experimenter reaching into the vacuum chamber while a nanoparticle is trapped inside the tweezer (photograph on the left). a)-f): Six consecutive pictures of a video showing the insertion procedure. The microscope objective is indicated by the blue shaded area, a red arrow points towards the trapped particle and the trapping mode is indicated by the light red area. The green shaded areas indicate the position of the two cavity mirrors.

vacuum chamber is vented and the quick access door is opened. Step b): The cavity is inserted while a particle is trapped inside the tweezer. The purple surfaces shown in figure 3.18 a) and b) serve as arrester for the cavity mirror holder. The cavity is gently moved into the the holder until it touches the two purple surfaces. The insertion procedure is very reproducible, hardly any realignment of the cavity is necessary. Typically, only the last steering mirror before the cavity needs minor adjustment in order to restore the pre-aligned coupling. Step c): The MX25 stage with mount including the collimation lens and holder is inserted into the vacuum chamber. Part d): The collimation lens tube is laced into the hole of the cavity mirror holder and screwed into the main aluminium block. The last step is closing the quick door and evacuating the vacuum chamber.

Six consecutive pictures of a video inserting the cavity into the vacuum chamber are shown in figure 3.19. In the first picture the levitated particle is marked by a red arrow. The red area indicates the trapping mode and the blue area indicates the microscope objective. The cavity is moved in from the top left side and its two mirrors are highlighted with green areas. Once the cavity

is touching the two stop surfaces (purple surfaces in figure 3.18 a)), which is shown in picture f), the collimation lens on the MX25 is added and the vacuum chamber is closed. The photograph in the left shows myself inserting the cavity through the quick access door.

Although this procedure might seem crude and the HCPCF experiment [62] or the MOBOT experiment [108] are potential alternatives, it is surprisingly reliable and reproducible. With a few days of training, four out of five trapped particles inside the tweezer survive the entire procedure. The most common reason for particle loss is coming too close to the vicinity of the trapped particle with the cavity. The entire loading procedure takes approximately 20 min.

3.3.5. Alignment of the Tweezer to the Cavity Mode

In order to align the microscope objective and hence, the particle with respect to the TEM00 mode of the cavity, a CCD camera is placed behind the cavity (outside of the vacuum chamber). The direction of the camera is indicated by the blue arrow in figure 3.20 a). Part b) to e) display photographs taken with

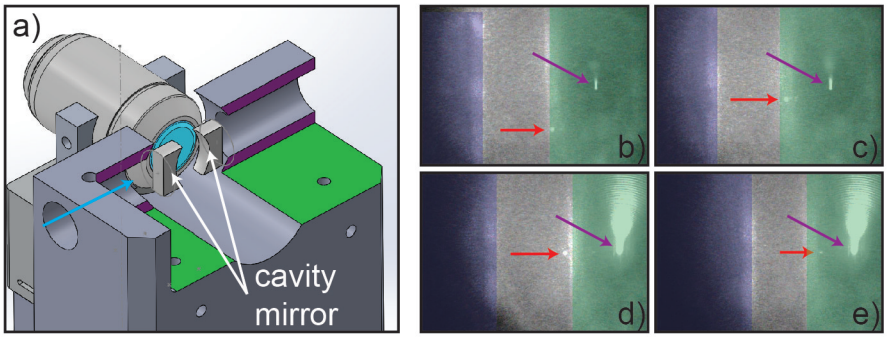

Figure 3.20.: a) The blue arrow highlights the camera perspective for pictures b)-e). b)-e): Alignment procedure between microscope objective and cavity mode (purple arrows) while a particle is trapped (red arrows). The blue area indicates the microscope objective and the green area indicates the cavity mirror.

this camera. The blue shaded area indicates the front part of the microscope objective, a red arrow points at the levitated particle, the green shaded area highlights one of the cavity mirrors and the purple arrow points at the TEM00 mode of the cavity. In the first three pictures the vertical position of the particle is adjusted with respect to the hight of the TEM00 mode by moving the microscope objective with the triaxial stage (MX35). Photographs d) and e) show how the microscope is moved towards the cavity mirror. Then, the

CCD camera is removed and the cavity homodyne read-out is monitored with a spectrum analyzer. The position of the microscope objective is systematically scanned around the position of the TEM00 mode until the motion of the particle becomes visible in the spectrum analyzer. Once the mechanical peak appears in the spectrum, this signal can be used to optimize the coupling between cavity mode and nanoparticle.

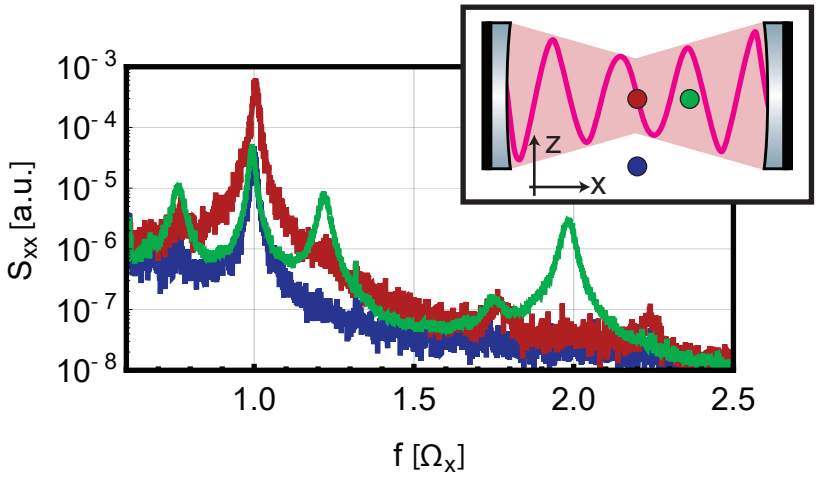

Figure 3.21.: Cavity Homodyne Read-out: The COM motion of a levitated particle inside the tweezer is aligned with respect to the linear slope of the cavity mode. Once the particle comes in the vicinity of the cavity field, its motion can be seen in the homodyne read-out of the cavity (blue trace). The position of the microscope objective with respect to the cavity mode is optimized by increasing the signal-to-noise ratio around the frequency of Ω_x and simultaneously minimizing the signal-to-noise at twice the mechanical frequency of the tweezer $2\Omega_x$. The colored dots (same color coding as traces) in the inset indicate the particle position inside the cavity standing wave

Figure 3.21 shows three homodyne read-out spectra S_{xx} while the microscope objective is aligned with respect to the tweezer. If the particle inside the tweezer comes in the vicinity of the cavity mode the homodyne read-out picks up the phase modulation due to the particle motion (blue trace). As soon as any coupling to the cavity mode is present, the signal-to-noise ratio around the frequency Ω_x, the motion along the cavity axis, needs to be maximised (red trace) while simultaneously minimizing the signal-to-noise ratio at the frequency $2\Omega_x$ kHz, which is indicative of quadratic coupling. This occurs if the particle is close to an antinode or a node of the standing wave inside the

cavity (green trace). In such a scenario the microscope objective needs to be moved along the cavity axis until the second harmonic vanishes (red trace).

This method is a convenient way of aligning the cavity and tweezer with respect to each other and of optimizing the coupling. Note that in the green trace, where the particle is close to an antinode or node of the cavity standing wave, a similar effect as described in chapter 3.1.4 appears. Due to the anharmonicity of the optical potential, the axial tweezer motion couples to the motion along the cavity axis and hence, two peaks at $\Omega_x \pm \Omega_z$ are observed.

3.3.6. Summary

The main result of this chapter is the ability to levitate a nanoparticle with an optical tweezer while simultaneously coupling it to a TEM00 mode of a high-finesse Fabry-Pérot cavity. This is achieved by reducing the diameter of high quality mirrors, three-dimensional alignment capabilities of the microscope objective and by consecutive execution of the experiment: Loading the tweezer without cavity present to protect the high quality mirrors and insertion of the cavity while the particle is trapped. These developments provide the basis to bring a levitated optomechanical system into high vacuum.

3.4. Experimental Levitated Cavity Optomechanics in High Vacuum

The previous chapter described how to equip a levitated cavity optomechanics experiment with an optical tweezer with the goal to operate in ultra-high vacuum and reach the strong quantum cooperativity regime $C_Q > 1$. Here the performance and the current limitations of the optical tweezer and the cavity are described. The mechanical losses Γ are solely measured with the tweezer down to the base pressure of the vacuum system ($p = 6 \times 10^{-7}$ mbar). OMIT measurements are performed with the combined system of tweezer and cavity to infer the optomechanical coupling rate g. Here we report the latest status of the currently ongoing experiments.

3.4.1. Relaxation Measurements

The mechanical losses are quantified with relaxation measurements. The procedure is completely analogous to the one used in the HCPCF experiment (chapter 2.5). The theoretical description can be found in chapter 3.1.5. A silica particle of radius $a = 71.5$ nm is levitated inside the optical tweezer without the cavity mode being present. All three spatial directions of the

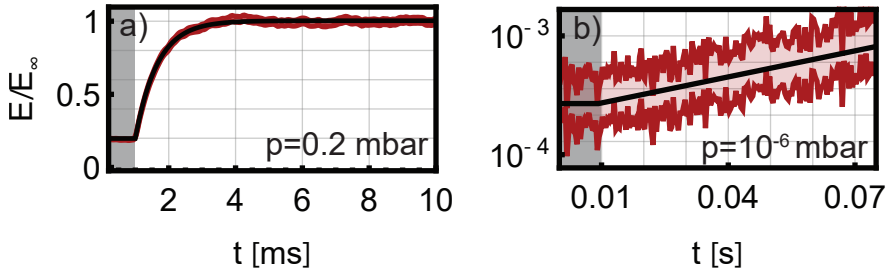

Figure 3.22.: Relaxation measurement of a particle levitated at a pressure of $p = 0.2$ mbar a) and $p = 10^{-6}$ mbar b). The particle is feedback cooled (indicated by the grey shaded area) to an effective temperature of $T_{\text{eff}} = 60$ K and $T_{\text{eff}} = 100$ mK, respectively. After reaching a steady state, feedback cooling is switched off and the relaxation towards thermal equilibrium is recorded. At high pressure the full exponential is observed whereas at low pressure only the linear part is measured to avoid losing the particle from the trap. The solid black curve is a fit to the particle energy (red).

particle motion are subject to parametric feedback cooling to avoid both, par-

ticle loss from the trap and coupling of modes. For pressures $p > 10^{-2}$ mbar, a pressure at which the particle stays trapped without feedback cooling, the three-dimensional feedback cooling is switched off until the COM motions relax back to thermal equilibrium $E_\infty = k_B T_0$. For pressures below $p < 10^{-2}$ mbar, feedback cooling is switched back on before relaxation to thermal equilibrium to prevent particle loss. Therefore, in the high-pressure regime the full exponential decay is resolved, while in the low-pressure regime only the linear part is accessible. Typically, the relaxation times for low pressures are on the order of $t \approx 1/(10\gamma_p)$. This procedure is repeated 5000 times for each pressure and the energy of the COM motions are computed as ensemble variance. To be precise, all recorded displacement trajectories were first bandpass filtered around the mechanical frequency with a bandwidth of 10 kHz, after which the variance was computed. Two examples for the tweezer x-direction (which coincides with the cavity axis) are shown in figure 3.22. Part a) shows a full relaxation to thermal equilibrium T_0 at a pressure of $p = 0.2$ mbar. The black curve is a fit to an exponential relaxation (equation 3.27). Part b) shows a relaxation measurement of the same particle at a pressure of $p = 10^{-6}$ mbar. The red shaded area is the computed variance within its error bars (note that the error bars for part b) are to little to be represented, however they are accounted for in the fit) and the solid black line is a fit to the linear part of the relaxation, see equation 3.28.

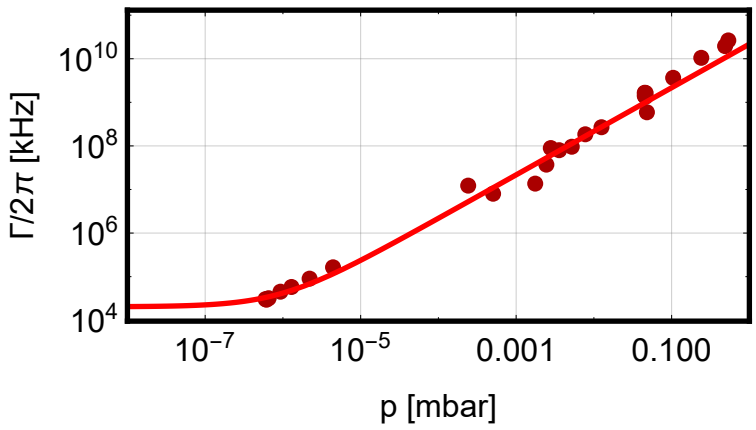

Figure 3.23.: Mechanical losses Γ are quantified via relaxation measurements along the x-axis as a function of pressures. The solid red line is a linear fit to the data indicating the recoil limit at low pressures.

In cases where a fit of a full relaxation was possible, the heating rate $\Gamma = E_\infty \gamma$ is computed with the two free fit parameters E_∞ and γ. In the cases

where only the beginning of the relaxation was observed, the slope of the fit returns the estimate for the mechanical losses Γ. Figure 3.23 shows a systematic measurement of the mechanical losses as function of pressure. The solid red line is a linear fit to the data. The plateau at low pressures indicates the recoil limit which is pressure independent and the linear behaviour at higher pressures resembles the mechanical losses due to collisions with residual air molecules in the vacuum chamber. Theoretical estimation of the recoil heating rate with equation 3.26 results in $\Gamma_{\mathrm{rc}} = 2\pi \times 7$ kHz (particle radius $a = 71.5$ nm, mechanical frequency $\Omega_{\mathrm{x}} = 2\pi \times 163$ kHz, trapping intensity $I = 6 \times 10^{11}$ W/m^2). The recoil heating rate from the fit is $\Gamma_{\mathrm{rc}} = 2\pi \times (20 \pm 7)$ kHz. The deviation to the theoretical prediction can be explained by the insufficient data for the relaxation measurement at low pressures. In order to get a better prediction for the recoil limit more data points which show a deviation from the linear pressure dependence are required. Further improvement of the vacuum system by installation of an ion pump would allow pumping to lower pressures. The lowest pressure achieved in the measurement presented here is $p = 6 \times 10^{-7}$ mbar and the total mechanical reheating rate at this pressure is $\Gamma = 2\pi \times 30$ kHz.

3.4.2. OMIT Measurements

The optomechanical interaction can change the transmission properties of the cavity via optomechanically induced transparency (OMIT), see chapter 3.2.3. This effect is used here to measure the optomechanical coupling rate g. Combination with the mechanical losses Γ and the optical losses κ allows us to compute the quantum cooperativity $C_Q = 4g^2/(\kappa\Gamma)$.

A particle with a radius of $a = 71.5$ nm is levitated with the tweezer and linearly coupled to the cavity mode, such that the interaction is described by equation 3.33. In addition to the strong, red-detuned control mode at a detuning of $\Delta = -\Omega_{\mathrm{m}}$, a second, weak probe mode is required to measure the transparency window in the cavity transmission induced by the optomechanical interaction. As already described in chapter 3.3.1, a phase modulation can be applied to the control mode in such a way that in addition to the carrier frequency at $\Delta = -\Omega_{\mathrm{m}}$, two sidebands at frequency $-\Omega_{\mathrm{m}} \pm \delta$ are generated. The output of a vector network analyzer (VNA, Rhode&Schwarz: ZNB8) is used to create the phase modulation at frequency δ, which is swept between 0 and $-1.5\Omega_{\mathrm{m}}$. The lower sideband at $-\Omega_{\mathrm{m}} - \delta$ moves away from the cavity resonance and is strongly suppressed by the cavity envelope. The upper sideband with frequency $-\Omega_{\mathrm{m}} + \delta$ moves towards the cavity resonance and is probing the transmission T. The resulting cavity field, comprising both, probe and control mode is monitored with the OMIT detector, see figure 3.10. The

detector signal of the interference between probe and control beam is used as input for the VNA. The VNA returns the transfer-function of the cavity optomechanical system as a function of the phase modulation δ, see equation 3.37.

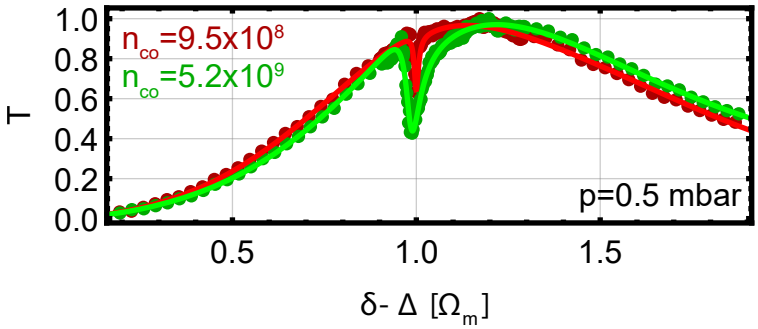

Figure 3.24.: OMIT measurements at high pressure: The red (green) data points represent the normalized transmission of the probe mode as a function of frequency $\delta - \Delta$ for $n_{\mathrm{co}} = 9.5 \times 10^8$ ($n_{\mathrm{co}} = 5.2 \times 10^9$) photons in the control mode. The frequency axis is normalized to the mechanical frequency Ω_{m} and while the detuning of the control mode is kept constant at $\Delta = -0.97\Omega_{\mathrm{m}}$ ($\Delta = -0.98\Omega_{\mathrm{m}}$), the frequency δ is swept over the cavity envelope. The solid lines are fits to the expected theoretical function resulting in an optomechanical coupling rate of $g = 2\pi \times 6$ kHz ($g = 2\pi \times 14$ kHz).

Figure 3.24 and figure 3.25 show preliminary results of OMIT measurements, both, at high pressure ($p = 0.5$ mbar) and at high vacuum ($p = 4 \times 10^{-6}$ mbar). During the high pressure measurements parametric feedback cooling was switched off all the time as particle loss does not occur. The particle position was optimized for maximal linear coupling to the cavity mode, see chapter 3.3.5, and the OMIT measurement was performed for two different control beam powers.

For the OMIT measurement in high vacuum, three-dimensional feedback cooling is necessary in order to keep the particle inside the trap. Once the particle is coupled linearly to the cavity mode, the strong control mode at $\Delta = -\Omega_{\mathrm{m}}$ and the probe mode sweep from 0 to $1.5\Omega_{\mathrm{m}}$ are initiated, the radial parametric feedback cooling is switched off for the time of one OMIT measurement ($t_{\mathrm{off}} < 1$ s). During the OMIT measurement the mechanical motion along the cavity axes is cooled via cavity-cooling (the control mode is on the red mechanical sideband), the axial tweezer motion (z) via parametric feedback and the remaining y-motion undergoes free oscillation until the feedback

cooling is switched back on. For an initial mode temperature of $T_{\text{eff}} \approx 0.13$ K (at a pressure of $p = 4 \times 10^{-6}$ mbar), according to the measurement shown in figure 3.6, and with a heating rate of $\Gamma \approx 170$ kHz, according to the measurement shown in figure 3.23, the effective mode temperature along the axes that undergoes free oscillations increases to $T_{\text{eff}} \approx 0.33$ K. As shown in figure

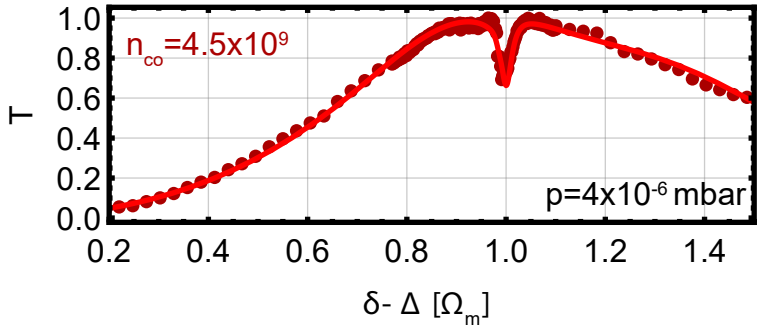

Figure 3.25.: OMIT measurements at low pressure: The red data points represent the normalized transmission of the probe mode as a function of frequency $\delta - \Delta$. The frequency axis is normalized to the mechanical frequency Ω_{m}, the detuning of the control mode is kept constant at $\Delta = -0.84\Omega_{\text{m}}$ while the probe frequency δ is swept over the cavity envelope. The solid line is a fit to the expected theoretical function resulting in an optomechanical coupling rate of $g = 2\pi \times 13$ kHz for $n_{\text{co}} = 4.5 \times 10^9$ photons in the control mode.

3.8 the three orthogonal modes are still decoupled at $T_{\text{eff}} = 15$ K. Hence, we can safely assume that no mode-coupling occurs at $T_{\text{eff}} \approx 0.33$ K, i.e. the free oscillations along the radial cavity axes should not interfere with the OMIT measurements.

A detailed theoretical treatment of the OMIT measurements performed here, as well as fitting data to theory and error estimation are a part of the PhD work of Uros Delic [121]. The main result of this chapter is: The combination of optical tweezer and cavity is functional and the OMIT measurements show unambiguously the coherent optomechanical coupling between COM motion of a levitated nanoparticle and a cavity mode at high vacuum ($p = 4 \times 10^{-6}$).

3.4.3. Estimate of the Quantum Cooperativity

The measurement results from the previous two chapters allow a tentative estimate of the quantum cooperativity at the present state of the experiment. At the lowest pressure of $p = 4 \times 10^{-6}$ mbar, where an OMIT measurement was

performed, an optomechanical coupling rate of $g = 2\pi \times 13$ kHz was inferred. The corresponding mechanical losses at the same pressure are $\Gamma = 2\pi \times 164$ kHz and the cavity linewidth, which is pressure independent, was determined to be $\kappa = 2\pi \times 200$ kHz (independent optical measurement without trapped particle). This results in a quantum cooperativity of

$$C_Q = \frac{4g^2}{\kappa\Gamma} = 0.02.$$

Note that this value for C_Q is obtained by independent measurements of the individual parameters. The mechanical losses were measured without cavity field present and hence the contribution of the control mode to the recoil heating is not accounted for. The presence of the control mode increases the recoil heating rate by $\Gamma = 2\pi \times 150$ Hz (computed value with particle radius $a = 71.5$ nm, mechanical frequency $\Omega_x = 2\pi \times 163$ kHz, control mode photon number $n_c = 5.4 \times 10^9$ corresponding to a control mode intensity of $I = 1.4 \times 10^{10}$ W/m^2). Assuming the coupling rate g stays the same, independent of pressure, the highest achievable quantum cooperativity is $C_Q = 0.11$ (limited by the measured mechanical losses of $\Gamma = 2\pi \times 30$ kHz at a pressure of $p = 6 \times 10^{-7}$ mbar).

3.5. Summary and Outlook

This chapter was motivated by the prospects of levitated cavity optomechanics for room-temperature quantum experiments with macroscopic objects. A necessary requirement to perform this type of experiment is reaching the strong quantum cooperativity regime $C_Q > 1$. Our previous experiment operated at a value of $C_Q \approx 10^{-7}$, limited by mechanical losses Γ due to particle escape from the optical trap around a pressure of $p \approx 1$ mbar. Instead of using a cavity mode to optically trap and control a nanoparticle, an optical tweezer with parametric feedback cooling is used to stably trap a particle and couple it to the cavity mode. Operation of the combined system at a pressure of $p = 4 \times 10^{-6}$ mbar was demonstrated, reaching an estimated quantum cooperativity of $C_Q = 0.02$, an improvement by five orders of magnitude while decreasing the mechanical losses by 6 orders of magnitude.

A more rigorous characterization of the optomechanical parameters are necessary to find the maximal reachable quantum cooperativity of the current system. The next step is to perform combined mechanical loss measurements, as described in chapter 3.4.1, including the cavity control mode and operation of the combined system at the base pressure of the vacuum system. As a second step, the vacuum system needs to be improved in order to operate tweezer and cavity at the recoil limit [57], which, for the current particle size, is expected at a pressure around $p = 10^{-8}$ mbar, see figure 3.22. The remaining parameter that can be improved to reach the strong quantum cooperativity regime is the optomechanical coupling rate $g = \sqrt{n}_{\mathrm{co}} g_0$. The most obvious way to increase the coupling is to increase the number of photons circulating inside the control mode n_{co} until either heating and drifting of the cavity due to a too high intra-cavity power limits this approach, or until the control mode reaches a similar intensity as the tweezer and starts to act as a trap. The particle would leave the linear slope of the standing wave and move towards the next antinode, where the linear coupling is reduced. Note that in the recoil limited regime particle size does not enter the quantum cooperativity. The mechanical losses for a cavity-tweezer system operating at the recoil limit are solely given by recoil heating, which is proportional to the particle volume $\Gamma \propto a^3$, see equation 3.26. The optomechanical coupling $g \propto a^{3/2}\ w_0^{-2}$ is proportional to the square-root of the volume and inversely proportional to the cavity mode waist, see chapter 3.2.1. Ultimately, the quantum cooperativity in the recoil limit is proportional to

$$C_Q = \frac{4g^2}{\kappa\Gamma} \propto \frac{1}{w_0^4}$$

and independent of particle radius a. Another way to increase the coupling

is a reduction in the cavity waist w_0, as shown in the above equation. These directions are also explored in [121].

A. Analog Electronic Circuits

A.1. Multiple Feedback Bandpass Filter

A multiple feedback bandpass filter is used to reject unwanted frequency components in a signal, i.e. noise peaks from a fiber amplifier. The design and values for the components were chosen with the help of this[1] homepage. Figure A.1 shows its circuit diagram. The transfer function of the filter is

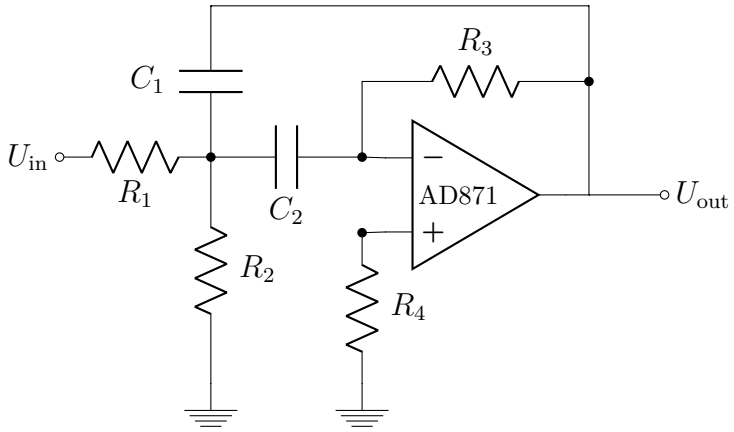

Figure A.1.: Multiple feedback bandpass filter

$$U_{\text{out}}(\omega) = -\frac{U_{\text{in}}}{R_1 C_1} \frac{\omega}{\omega^2 + \omega\left(\frac{1}{R_3 C_2} + \frac{1}{R_3 C_1}\right) + \frac{1}{R_3 C_1 C_2}\left(\frac{1}{R_1} + \frac{1}{R_2}\right)}$$

and its center frequency is given by

$$\omega_0 = \sqrt{\frac{1}{R_3 C_1 C_2}\left(\frac{1}{R_1} + \frac{1}{R_2}\right)}.$$

Resistor $R_4 = 10\text{k}\Omega$ is used to ground the positive input of the operational amplifier. Figure A.2 shows the frequency response of the multiple feedback bandpass filter for a center frequency of $\omega_0 = 2\pi \times 300$ kHz with the following components: $R_1 = 5.1$ kΩ, $R_2 = 3.6$ kΩ, $R_3 = 9.1$ kΩ, $R_4 = 10$ kΩ, $C_1 = 100$ pF, $C_2 = 150$ pF and a AD817 from Analog Devices [139].

[1] http://sim.okawa-denshi.jp/en/OPtazyuBakeisan.htm

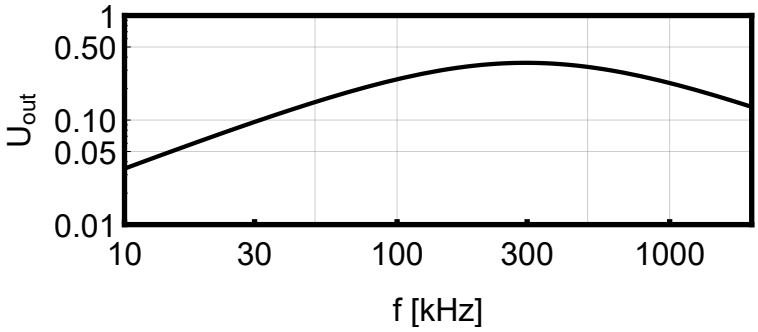

Figure A.2.: Amplitude response of a multiple feedback bandpass filter for $\omega_0 = 2\pi \times 300\text{kHz}$

A.2. Multiple Feedback Highpass Filter

This highpass filter is a part of the feedback cooling electronics in the HCPCF experiment. It suppresses low frequency acoustic noise in the read-out signal. The design and values for the components were chosen with the help of this[2] homepage. Figure A.3 shows its circuit diagram. The transfer function of the

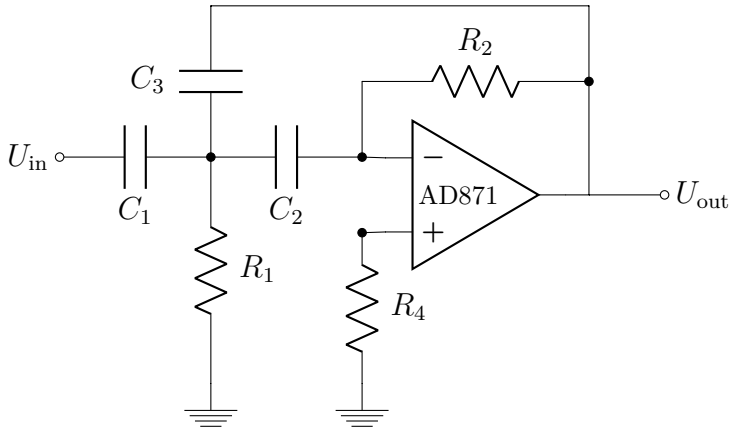

Figure A.3.: Multiple feedback highpass filter

filter is

$$U_{\text{out}}(\omega) = -U_{\text{in}} \frac{1}{C_3} \frac{\omega^2 C}{\omega^2 + \omega \frac{C_1+C_2+C_3}{R_2 C_2 C_3} + \frac{1}{R_1 R_2 C_2 C_3}}$$

and its cut-off frequency is given by

$$\omega_0 = \frac{1}{\sqrt{R_1 R_2 C_2 C_3}}$$

[2] http://sim.okawa-denshi.jp/en/OPtazyuBakeisan.htm

Resistor $R_4 = 10\text{k}\Omega$ is used to ground the positive input of the operational amplifier. Figure A.4 shows the frequency response for a multiple feedback

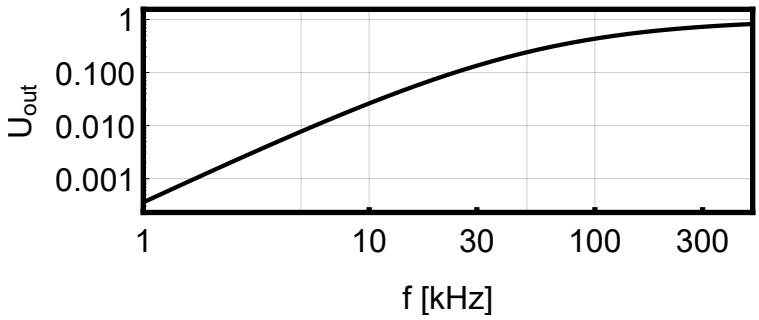

Figure A.4.: Amplitude response of a multiple feedback highpass filter for $\omega_0 = 2\pi \times 50$ kHz

high-pass filter for a cut-off frequency of $\omega_0 = 2\pi \times 50$ kHz with the following components: $R_1 = 3\,\text{k}\Omega$, $R_2 = 6.8\,\text{k}\Omega$, $R_4 = 10\,\text{k}\Omega$, $C_1 = 680$ pF, $C_2 = 680$ pF, $C_3 = 680$ pF and a AD817 from Analog Devices [139].

A.3. Variable Gain Amplifier

The variable gain amplifier is used to continuously amplify an arbitrary input voltage U_{in}, e.g. for feedback control. The design used here is from [140] and shown in figure A.5.

The capacitor C_2 limits the gain towards DC-frequencies and the capacitor C_1 in combination with resistor R_4 builds a highpass filter to block DC signals entering the amplifier. The transfer function of the circuit is given by

$$U_{\text{out}} = U_{\text{in}} \frac{R_1 + R_2}{R_1} = g U_{\text{in}}$$

with the gain $g = (R_1 + R_2)/R_1$. By changing the value of R_2 the gain g of the amplifier is changed. A typical implementation uses the following components: $C_1 = 220$ nF, $C_2 = 4.7\ \mu$F, $R_4 = 100\ \text{k}\Omega$. For a variable gain between $g = 1$ and $g \approx 10$ the defines the remaining components: $R_1 = 1\ \text{k}\Omega$, a potentiometer with $R_2 = 10\text{k}\Omega$ and a AD817 from Analog Devices [139].

A.4. Phase Shifter

The phase-shifter circuit is used to effectively delay an oscillatory signal $U_{\text{in}}(t)$ by a time t_0. For an oscillation frequency Ω, the phase shift corresponding to

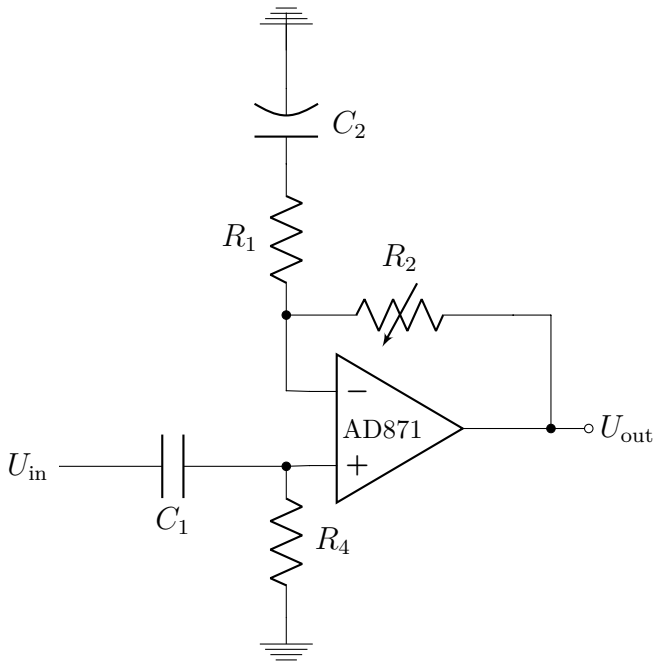

Figure A.5.: Variable gain amplifier

t_0 is $\phi = \Omega t_0$. The circuit diagram is shown in figure A.6 and based on [141]. The complex transfer function of this circuit is given by

$$U_{\text{in}}(\omega) = U_{\text{out}} \frac{1 - \omega^2 R^2 C^2 - 2i\omega RC}{1 + \omega^2 R^2 C^2}$$

with $R = R_2 + R_4$. The circuit has unity gain $|U_{\text{in}}/U_{\text{out}}| = 1$ and the phase angle ϕ between input signal U_{in} and output signal U_{out} is given by

$$\tan\phi = \frac{-2\omega RC}{1 + \omega^2 R^2 C^2}$$

The value of $R = R_2 + R_4$ can be changed with the potentiometer R_2 and hence, the phase between ϕ between input and output signal. The circuit is used to introduce a well defined delay for axial direct feedback cooling in the HCPCF and for parametric feedback cooling in the tweezer. For example, the circuit for direct axial feedback consists of the following components: $R_1 = 12$ kΩ, $R_4 = 120$ Ω, a potentiometer with $R_2 = 10$ kΩ, $C = 100$ pF and a OP37 from Analog Devices [142].

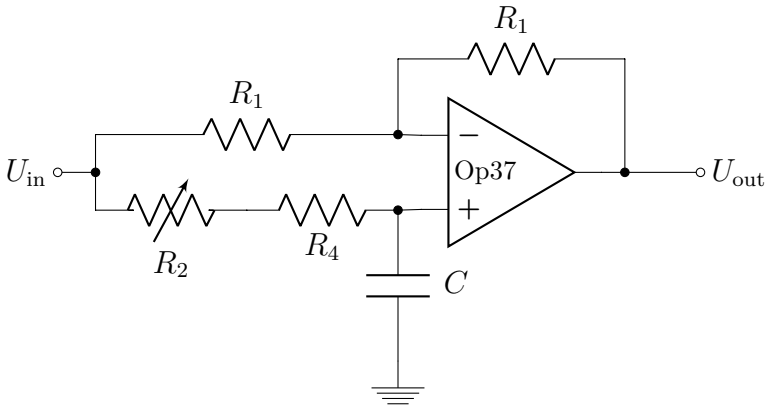

Figure A.6.: Phase shifter

A.5. Differential Amplifier

For the locking schemes of particle read-outs as well as for homodyne detection we need the difference between two voltage signals U_1 and U_2. The differential amplifier circuit shown in figure A.7 is a simple circuit to perform this operation. The transfer function of this circuit is given by

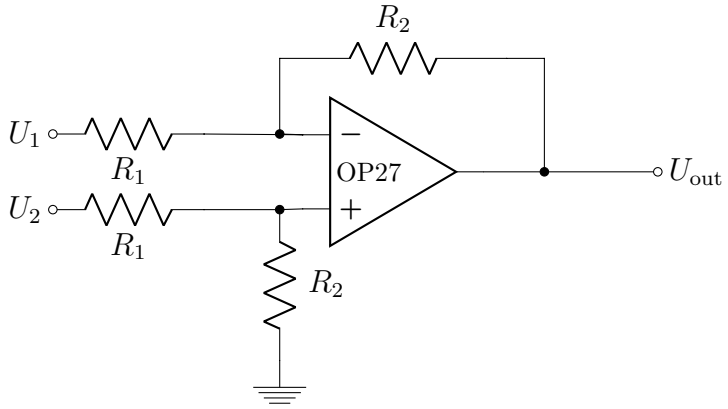

Figure A.7.: Differential amplifier

$$U_{\text{out}} = \frac{R_2}{R_1}(U_2 - U_1).$$

For $R_1 = R_2 = 10\text{k}\Omega$, the output voltage resembles the exact difference voltage between the two input voltages. As operational amplifier a OP27 from Analog Devices [143] is used.

A.6. Differentiator

For radial electrical feedback cooling, an analog differentiator is used to derive the modulation signal proportional to the particle velocity. The differentiator circuit shown in figure A.8 returns the time derivative $U_{\text{out}} \propto dU_{\text{in}}/dt$ of an input voltage signal U_{in}. The transfer function of the circuit is given by

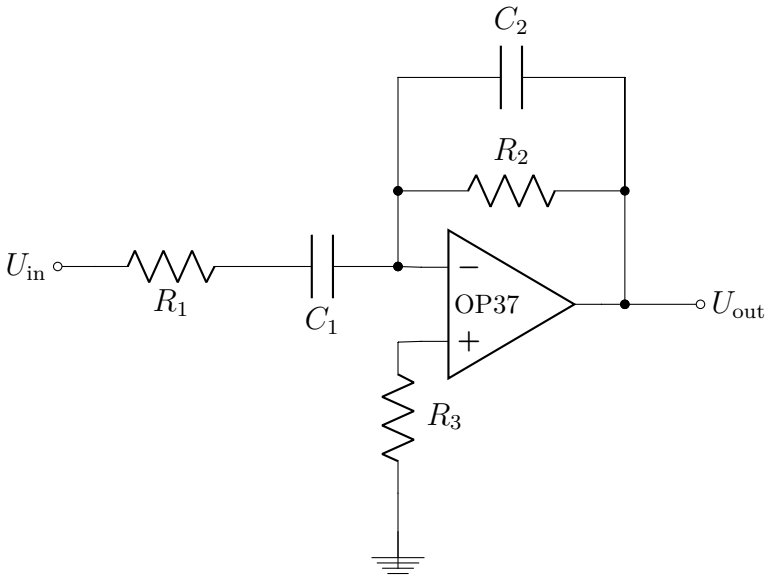

Figure A.8.: Differentiator

$$U_{\text{out}} = -R_2 C_1 \frac{dU_{\text{in}}}{dt}.$$

The additional resistor R_1 and capacitance C_2 limit the gain at high frequencies to suppress noise amplification. The circuit used for radial electrical feedback in the HCPCF experiment consists of the following components: $R_1 = 15\ \Omega$, $R_2 = 1\ \text{k}\Omega$, $R_3 = 10\ \text{k}\Omega$, $C_1 = 4\ \text{nF}$, $C_2 = 400\ \text{pF}$ an a OP37 from Analog Devices [142].

Bibliography

[1] A. Ashkin. Acceleration and Trapping of Particles by Radiation Pressure. *Physical Review Letters*, 24(4):156–159, jan 1970.

[2] A. Ashkin. Optical Levitation by Radiation Pressure. *Applied Physics Letters*, 19(8):283, 1971.

[3] A. Ashkin and J. M. Dziedzic. Optical levitation in high vacuum. *Applied Physics Letters*, 28(6):333, 1976.

[4] J. Gieseler, L. Novotny, and R. Quidant. Thermal nonlinearities in a nanomechanical oscillator. *Nature Physics*, 9(12):806–810, nov 2013.

[5] D. E. Chang, C. A. Regal, S. B. Papp, D. J. Wilson, J. Ye, O. Painter, H. J. Kimble, and P. Zoller. Cavity opto-mechanics using an optically levitated nanosphere. *Proceedings of the National Academy of Sciences*, 107(3):1005–1010, jan 2010.

[6] S. Chu, J. E. Bjorkholm, A. Ashkin, and A. Cable. Experimental Observation of Optically Trapped Atoms. *Physical Review Letters*, 57(3):314–317, jul 1986.

[7] W. D. Phillips. Nobel Lecture: Laser cooling and trapping of neutral atoms. *Reviews of Modern Physics*, 70(3):721–741, jul 1998.

[8] A. Ashkin and J. Dziedzic. Optical trapping and manipulation of viruses and bacteria. *Science*, 235(4795):1517–1520, mar 1987.

[9] T. Takekoshi and R. J. Knize. Optical Guiding of Atoms through a Hollow-Core Photonic Band-Gap Fiber. *Physical Review Letters*, 98(21):210404, may 2007.

[10] C. A. Christensen, S. Will, M. Saba, G.-B. Jo, Y.-I. Shin, W. Ketterle, and D. Pritchard. Trapping of ultracold atoms in a hollow-core photonic crystal fiber. *Physical Review A*, 78(3):033429, sep 2008.

[11] F. Benabid, J. C. Knight, and P. St. J. Russell. Particle levitation and guidance in hollow-core photonic crystal fiber. *Optics Express*, 10(21):1195, oct 2002.

[12] O. A. Schmidt, M. K. Garbos, T. G. Euser, and P. St. J. Russell. Metrology of laser-guided particles in air-filled hollow-core photonic crystal fiber. *Optics Letters*, 37(1):91, jan 2012.

[13] O. A. Schmidt, T. G. Euser, and P. St. J. Russell. Mode-based microparticle conveyor belt in air-filled hollow-core photonic crystal fiber. *Optics Express*, 21(24):29383, dec 2013.

[14] N. Kiesel, F. Blaser, U. Delic, D. Grass, R. Kaltenbaek, and M. Aspelmeyer. Cavity cooling of an optically levitated submicron particle. *Proceedings of the National Academy of Sciences*, 110(35):14180–14185, aug 2013.

[15] Z.-Q. Yin, A. A. Geraci, and T. Li. Optomechanics of levitated dielectric particle. *International Journal of Modern Physics B*, 27(26):1330018, oct 2013.

[16] O. Romero-Isart, A. Pflanzer, F. Blaser, R. Kaltenbaek, N. Kiesel, M. Aspelmeyer, and J. Cirac. Large Quantum Superpositions and Interference of Massive Nanometer-Sized Objects. *Physical Review Letters*, 107(020405):1–4, jul 2011.

[17] R. Kaltenbaek, G. Hechenblaikner, N. Kiesel, O. Romero-Isart, K. Schwab, U. Johann, and M. Aspelmeyer. Macroscopic quantum resonators (MAQRO). *Experimental Astronomy*, 34(2):123–164, mar 2012.

[18] A. A. Geraci, S. B. Papp, and J. Kitching. Short-range force detection using optically-cooled levitated microspheres. *Physical Review Letters*, 105(10):1–4, jun 2010.

[19] A. Arvanitaki and A. A. Geraci. Detecting High-Frequency Gravitational Waves with Optically Levitated Sensors. *Physical Review Letters*, 110(7):071105, feb 2013.

[20] J. D. Teufel, T. Donner, D. Li, J. W. Harlow, M. S. Allman, K. Cicak, A. J. Sirois, J. D. Whittaker, K. W. Lehnert, and R. W. Simmonds. Sideband cooling of micromechanical motion to the quantum ground state. *Nature*, 475(7356):359–363, jul 2011.

[21] J. Chan, T. Alegre, A. Safavi-Naeini, J. T. Hill, A. Krause, S. Gröblacher, M. Aspelmeyer, and O. Painter. Laser cooling of a nanomechanical oscillator into its quantum ground state. *Nature*, 478(7367):89–92, oct 2011.

[22] D. W. C. Brooks, T. Botter, S. Schreppler, T. P. Purdy, N. Brahms, and D. M. Stamper-Kurn. Non-classical light generated by quantum-noise-driven cavity optomechanics. *Nature*, 488(7412):476–480, aug 2012.

[23] A. H. Safavi-Naeini, S. Gröblacher, J. T. Hill, J. Chan, M. Aspelmeyer, and O. Painter. Squeezed light from a silicon micromechanical resonator. *Nature*, 500(7461):185–189, aug 2013.

[24] T. P. Purdy, P.-L. Yu, R. W. Peterson, N. S. Kampel, and C. A. Regal. Strong Optomechanical Squeezing of Light. *Physical Review X*, 3(3):031012, sep 2013.

[25] R. Riedinger, S. Hong, R. A. Norte, J. A. Slater, J. Shang, A. G. Krause, V. Anant, M. Aspelmeyer, and S. Gröblacher. Non-classical correlations between single photons and phonons from a mechanical oscillator. *Nature*, 530(7590):313–316, jan 2016.

[26] S. Hong, R. Riedinger, I. Marinković, A. Wallucks, S. G. Hofer, R. A. Norte, M. Aspelmeyer, and S. Gröblacher. Hanbury Brown and Twiss interferometry of single phonons from an optomechanical resonator. *Science*, 358(6360):203–206, oct 2017.

[27] T. A. Palomaki, J. D. Teufel, R. W. Simmonds, and K. W. Lehnert. Entangling mechanical motion with microwave fields. *Science (New York, N.Y.)*, 342(6159):710–3, nov 2013.

[28] R. Riedinger, A. Wallucks, I. Marinković, C. Löschnauer, M. Aspelmeyer, S. Hong, and S. Gröblacher. Remote quantum entanglement between two micromechanical oscillators. *Nature*, 556(7702):473–477, apr 2018.

[29] T. A. Birks, P. J. Roberts, P. St. J. Russell, D. M. Atkin, and T. J. Shepherd. Full 2-D photonic bandgaps in silica/air structures. *Electronics Letters*, 31(22):1941–1943, oct 1995.

[30] NKT Photonics. *HC-1060-02 Hollow Core Photonic Bandgap Fiber for 1060 nm Range Applications*. HC-1060-02-100409.

[31] R. F. Cregan, B. J. Mangan, J. C. Knight, T. A. Birks, P. St. J. Russell, P. J. Roberts, and D. C. Allan. Single-Mode Photonic Band Gap Guidance of Light in Air. *Science*, 285(5433):1537–1539, sep 1999.

[32] G. Humbert, J. C. Knight, G. Bouwmans, P. St. J. Russell, D. P. Williams, P. J. Roberts, and B. J. Mangan. Hollow core photonic crystal fibers for beam delivery. *Optics Express*, 12(8):1477, apr 2004.

[33] A. Ermolov, K. F. Mak, F. Tani, P. Hölzer, J. C. Travers, and P. St. J. Russell. Low loss hollow optical-waveguide connection from atmospheric pressure to ultra-high vacuum. *Applied Physics Letters*, 103(26):261115, dec 2013.

[34] F. Benabid, F. Couny, J. C. Knight, T. A. Birks, and P. St. J. Russell. Compact, stable and efficient all-fibre gas cells using hollow-core photonic crystal fibres. *Nature*, 434(7032):488–491, mar 2005.

[35] G. Epple, K. S. Kleinbach, T. G. Euser, N. Y. Joly, T. Pfau, P. St. J. Russell, and R. Löw. Rydberg atoms in hollow-core photonic crystal fibres. *Nature Communications*, 5(May):4132, jun 2014.

[36] O. A. Schmidt, M. K. Garbos, T. G. Euser, and P. St. J. Russell. Reconfigurable Optothermal Microparticle Trap in Air-Filled Hollow-Core Photonic Crystal Fiber. *Physical Review Letters*, 109(2):024502, jul 2012.

[37] J. C. Knight. New Ways to Guide Light. *Science*, 296(5566):276–277, apr 2002.

[38] P. St. J. Russell. Photonic Crystal Fibers. *Science*, 299(5605):358–362, jan 2003.

[39] P. St. J. Russell. Photonic-Crystal Fibers. *Journal of Lightwave Technology*, 24(12):4729–4749, dec 2006.

[40] F. Benabid. Hollow-core photonic bandgap fibre: new light guidance for new science and technology. *Philosophical Transactions of the Royal Society A: Mathematical, Physical and Engineering Sciences*, 364(1849):3439–3462, dec 2006.

[41] F. Benabid and P. J. Roberts. Linear and nonlinear optical properties of hollow core photonic crystal fiber. *Journal of Modern Optics*, 58(2):87–124, jan 2011.

[42] A. Rohrbach and E. H. K. Stelzer. Optical trapping of dielectric particles in arbitrary fields. *Journal of the Optical Society of America A*, 18(4):839, apr 2001.

[43] K. C. Neuman and S. M. Block. Optical trapping. *Review of Scientific Instruments*, 75(9):2787–2809, sep 2004.

[44] A. Jonás and P. Zemánek. Light at work: The use of optical forces for particle manipulation, sorting, and analysis. *Electrophoresis*, 29(24):4813–4851, dec 2008.

[45] E. A. J. Marcatili and R. A. Schmeltzer. Hollow Metallic and Dielectric Waveguides for Long Distance Optical Transmission and Lasers. *Bell System Technical Journal*, 43(4):1783–1809, jul 1964.

[46] J. Fesel. *Position readout of an optically trapped nano sphere in a hollow core photonic crystal fiber as a step towards parametric feedback cooling.* Master thesis, University of Vienna, 2014.

[47] L. Novotny and B. Hecht. *Principles of Nano-Optic.* Cambridge University Press, 2006.

[48] G. Gouesbet and G. Gréhan. *Generalized Lorenz-Mie Theories.* Springer International Publishing AG, second edition, 2017.

[49] L. Rayleigh. XXXIV. On the transmission of light through an atmosphere containing small particles in suspension, and on the origin of the blue of the sky. *The London, Edinburgh, and Dublin Philosophical Magazine and Journal of Science*, 47(287):375–384, apr 1899.

[50] Y. Harada and T. Asakura. Radiation forces on a dielectric sphere in the Rayleigh scattering regime. *Optics Communications*, 124(5-6):529–541, mar 1996.

[51] T. A. Nieminen, V. L. Y. Loke, A. B. Stilgoe, G. Knöner, A. M. Brańczyk, N. R. Heckenberg, and H. Rubinsztein-Dunlop. Optical tweezers computational toolbox. *Journal of Optics A: Pure and Applied Optics*, 9(8):S196–S203, aug 2007.

[52] J. D. Jackson. *Classical Electrodynamics.* Wiley, third edition, 1998.

[53] T. Čižmár, V. Garcés-Chávez, K. Dholakia, and P. Zemánek. Optical conveyor belt for delivery of submicron objects. *Applied Physics Letters*, 86(17):174101, apr 2005.

[54] D. S. Lemons and A. Gythiel. Paul Langevin's 1908 paper "On the Theory of Brownian Motion" ["Sur la théorie du mouvement brownien," C. R. Acad. Sci. (Paris) 146 , 530–533 (1908)]. *American Journal of Physics*, 65(11):1079–1081, nov 1997.

[55] M. Aspelmeyer, Tobias J. Kippenberg, and F. Marquardt. Cavity optomechanics. *Reviews of Modern Physics*, 86(4):1391–1452, dec 2014.

[56] S. A. Beresnev, V. G. Chernyak, and G. A. Fomyagin. Motion of a spherical particle in a rarefied gas. Part 2. Drag and thermal polarization. *Journal of Fluid Mechanics*, 219(-1):405, oct 1990.

[57] V. Jain, J. Gieseler, C. Moritz, C. Dellago, R. Quidant, and L. Novotny. Direct Measurement of Photon Recoil from a Levitated Nanoparticle. *Physical Review Letters*, 116(24):243601, jun 2016.

[58] A. A. Clerk, M. H. Devoret, S. M. Girvin, F. Marquardt, and R. J. Schoelkopf. Introduction to quantum noise, measurement, and amplification. *Reviews of Modern Physics*, 82(2):1155–1208, apr 2010.

[59] J. Millen, T. Deesuwan, P. F. Barker, and J. Anders. Nanoscale temperature measurements using non-equilibrium Brownian dynamics of a levitated nanosphere. *Nature nanotechnology*, 9(May):425–429, may 2014.

[60] E. Hebestreit, R. Reimann, M. Frimmer, and L. Novotny. Measuring the internal temperature of a levitated nanoparticle in high vacuum. *Physical Review A*, 97(4):043803, apr 2018.

[61] E. Hebestreit, M. Frimmer, R. Reimann, C. Dellago, F. Ricci, and L. Novotny. Calibration and energy measurement of optically levitated nanoparticle sensors. *Review of Scientific Instruments*, 89(3):033111, mar 2018.

[62] D. Grass, J. Fesel, S. G. Hofer, N. Kiesel, and M. Aspelmeyer. Optical trapping and control of nanoparticles inside evacuated hollow core photonic crystal fibers. *Applied Physics Letters*, 108(22):221103, may 2016.

[63] D. Grass. *Optical Trapping and Transport of Nanoparticles with Hollow Core Photonic Crystal Fibers*. Master thesis, University of Vienna, 2013.

[64] NKT Photonics. *Fiber Handling, Stripping, Cleaving and Coupling*, August 2009.

[65] D. R. Burnham and D. McGloin. Holographic optical trapping of aerosol droplets. *Optics Express*, 14(9):4175, may 2006.

[66] S. Kuhr, W. Alt, D. Schrader, I. Dotsenko, Y. Miroshnychenko, W. Rosenfeld, M. Khudaverdyan, V. Gomer, A. Rauschenbeutel, and D. Meschede. Coherence Properties and Quantum State Transportation in an Optical Conveyor Belt. *Physical Review Letters*, 91(21):213002, nov 2003.

[67] T. R. Albrecht, P. Grütter, D. Horne, and D. Rugar. Frequency modulation detection using high- Q cantilevers for enhanced force microscope sensitivity. *Journal of Applied Physics*, 69(2):668–673, jan 1991.

[68] B. Abbott et al. Analysis of LIGO data for gravitational waves from binary neutron stars. *Physical Review D*, 69(12):122001, jun 2004.

[69] P. F. Cohadon, A. Heidmann, and M. Pinard. Cooling of a Mirror by Radiation Pressure. *Physical Review Letters*, 83(16):3174–3177, oct 1999.

[70] D. Kleckner and D. Bouwmeester. Sub-kelvin optical cooling of a micromechanical resonator. *Nature*, 444(7115):75–78, nov 2006.

[71] M. Poggio, C. L. Degen, H. J. Mamin, and D. Rugar. Feedback Cooling of a Cantilever's Fundamental Mode below 5 mK. *Physical Review Letters*, 99(1):017201, jul 2007.

[72] A. Ashkin and J. M. Dziedzic. Feedback stabilization of optically levitated particles. *Applied Physics Letters*, 30(4):202, 1977.

[73] T. Li, S. Kheifets, and M. G. Raizen. Millikelvin cooling of an optically trapped microsphere in vacuum. *Nature Physics*, 7(7):527–530, mar 2011.

[74] D. C. Moore, A. D. Rider, and G. Gratta. Search for Millicharged Particles Using Optically Levitated Microspheres. *Physical Review Letters*, 113(25):251801, dec 2014.

[75] G. Ranjit, D. P. Atherton, J. H. Stutz, M. Cunningham, and A. A. Geraci. Attonewton force detection using microspheres in a dual-beam optical trap in high vacuum. *Physical Review A*, 91(5):051805, may 2015.

[76] G. Ranjit, M. Cunningham, K. Casey, and A. A. Geraci. Zeptonewton force sensing with nanospheres in an optical lattice. *Physical Review A*, 93(5):1–5, mar 2016.

[77] M. Frimmer, K. Luszcz, S. Ferreiro, V. Jain, E. Hebestreit, and L. Novotny. Controlling the net charge on a nanoparticle optically levitated in vacuum. *Physical Review A*, 95(6):061801, jun 2017.

[78] F. Lindenfelser, B. Keitch, D. Kienzler, D. Bykov, P. Uebel, M. A. Schmidt, P. St. J. Russell, and J. P. Home. An ion trap built with photonic crystal fibre technology. *Review of Scientific Instruments*, 86(3):033107, mar 2015.

[79] O. Romero-Isart, M. L. Juan, R. Quidant, and J. I. Cirac. Toward quantum superposition of living organisms. *New Journal of Physics*, 12(3):033015, mar 2010.

[80] P. F. Barker and M. N. Shneider. Cavity cooling of an optically trapped nanoparticle. *Physical Review A*, 81(2):023826, feb 2010.

[81] J. Bateman, S. Nimmrichter, K. Hornberger, and H. Ulbricht. Near-field interferometry of a free-falling nanoparticle from a point-like source. *Nature Communications*, 5:4788, sep 2014.

[82] O. Romero-Isart. Quantum superposition of massive objects and collapse models. *Physical Review A*, 84(5):052121, nov 2011.

[83] P. Asenbaum, S. Kuhn, S. Nimmrichter, U. Sezer, and M. Arndt. Cavity cooling of free silicon nanoparticles in high vacuum. *Nature Communications*, 4:2743, nov 2013.

[84] S. Kuhn, P. Asenbaum, A. Kosloff, M. Sclafani, B. A. Stickler, S. Nimmrichter, K. Hornberger, O. Cheshnovsky, F. Patolsky, and M. Arndt. Cavity-Assisted Manipulation of Freely Rotating Silicon Nanorods in High Vacuum. *Nano Letters*, 15(8):5604–5608, aug 2015.

[85] G. A. T. Pender, P. F. Barker, F. Marquardt, J. Millen, and T. S. Monteiro. Optomechanical cooling of levitated spheres with doubly resonant fields. *Physical Review A*, 85(2):021802, feb 2012.

[86] J. F. O'Hanlon. *A Users's Guide to Vacuum Technology*. John Wiley & Sons, Inc., third edition, 2003.

[87] C. A. Siegele. *3D positioning of optical levitated nanoparticles using hollow core fibers*. Bachelor thesis, University of Vienna, 2016.

[88] L. Boltzmann. *I. Theil: Theorie der Gase mit einatomigen Molekülen, deren Dimensionen gegen die mittlere Weglänge verschwinden (Bd. 1 von 2)*. Barth, first edition, 1896.

[89] L. Boltzmann. *II. Theil: Theorie van der Waals'; Gase mit zusammengesetzten Molekülen; Gasdissociation; Schlussbemerkungen (Bd. 2 von 2)*. Barth, first edition, 1898.

[90] C. Cercignani. *The Boltzmann Equation and Its Applications*. Springer-Verlag New York, first edition, 1988.

[91] F. M. Sharipov and V. D. Seleznev. Rarefied gas flow through a long tube at any pressure ratio. *Journal of Vacuum Science & Technology A: Vacuum, Surfaces, and Films*, 12(5):2933–2935, sep 1994.

[92] S. Varoutis, D. Valougeorgis, O. Sazhin, and F. Sharipov. Rarefied gas flow through short tubes into vacuum. *Journal of Vacuum Science & Technology A: Vacuum, Surfaces, and Films*, 26(2):228–238, 2008.

[93] Z. Yang and S. V. Garimella. Rarefied gas flow in microtubes at different inlet-outlet pressure ratios. *Physics of Fluids*, 21(5):052005, may 2009.

[94] J. Gieseler, R. Quidant, C. Dellago, and L. Novotny. Dynamic relaxation of a levitated nanoparticle from a non-equilibrium steady state. *Nature Nanotechnology*, 9(5):358–364, may 2014.

[95] T. S. Monteiro, J. Millen, G. A. T. Pender, F. Marquardt, D. E. Chang, and P. F. Barker. Dynamics of levitated nanospheres: towards the strong coupling regime. *New Journal of Physics*, 15(1):015001, jan 2013.

[96] A. Geraci and H. Goldman. Sensing short range forces with a nanosphere matter-wave interferometer. *Physical Review D*, 92(6):062002, sep 2015.

[97] D. Sesko, T. Walker, C. Monroe, A. Gallagher, and C. Wieman. Collisional losses from a light-force atom trap. *Physical Review Letters*, 63(9):961–964, aug 1989.

[98] C. N. Cohen-Tannoudji. Nobel Lecture: Manipulating atoms with photons. *Reviews of Modern Physics*, 70(3):707–719, jul 1998.

[99] A. Ashkin. Trapping of Atoms by Resonance Radiation Pressure. *Physical Review Letters*, 40(12):729–732, mar 1978.

[100] A. Ashkin, J. M. Dziedzic, J. E. Bjorkholm, and S. Chu. Observation of a single-beam gradient force optical trap for dielectric particles. *Optics Letters*, 11(5):288, may 1986.

[101] J. Gieseler, B. Deutsch, R. Quidant, and L. Novotny. Subkelvin Parametric Feedback Cooling of a Laser-Trapped Nanoparticle. *Physical Review Letters*, 109(10):103603, sep 2012.

[102] R. A. Norte, J. P. Moura, and S. Gröblacher. Mechanical Resonators for Quantum Optomechanics Experiments at Room Temperature. *Physical Review Letters*, 116(14):147202, apr 2016.

[103] Y. Tsaturyan, A. Barg, E. S. Polzik, and A. Schliesser. Ultracoherent nanomechanical resonators via soft clamping and dissipation dilution. *Nature Nanotechnology*, 12(8):776–783, jun 2017.

[104] L. P. Neukirch, J. Gieseler, R. Quidant, L. Novotny, and N. A. Vamivakas. Observation of nitrogen vacancy photoluminescence from an optically levitated nanodiamond. *Optics Letters*, 38(16):2976, aug 2013.

[105] J. Gieseler, L. Novotny, C. Moritz, and C. Dellago. Non-equilibrium steady state of a driven levitated particle with feedback cooling. *New Journal of Physics*, 17(4):045011, apr 2015.

[106] F. Ricci, R. A. Rica, M. Spasenovic, J. Gieseler, L. Rondin, L. Novotny, and R. Quidant. Optically levitated nanoparticle as a model system for stochastic bistable dynamics. *Nature Communications*, 8(May):1–7, 2017.

[107] J. Gieseler, M. Spasenović, L. Novotny, and R. Quidant. Nonlinear Mode Coupling and Synchronization of a Vacuum-Trapped Nanoparticle. *Physical Review Letters*, 112(10):103603, mar 2014.

[108] P. Mestres, J. Berthelot, M. Spasenović, J. Gieseler, L. Novotny, and R. Quidant. Cooling and manipulation of a levitated nanoparticle with an optical fiber trap. *Applied Physics Letters*, 107(15):151102, oct 2015.

[109] M. Frimmer, J. Gieseler, and L. Novotny. Cooling Mechanical Oscillators by Coherent Control. *Physical Review Letters*, 117(16):163601, oct 2016.

[110] L. Rondin, J. Gieseler, F. Ricci, R. Quidant, C. Dellago, and L. Novotny. Direct measurement of Kramers turnover with a levitated nanoparticle. *Nature Nanotechnology*, 12(12):1130–1133, oct 2017.

[111] J. Gieseler. *Dynamics of optically levitated nanoparticles in high vacuum*. PhD thesis, Universitat Politècnica de Catalunya, 2014.

[112] V. Jain. *Levitated optomechanics at the recoil limit*. PhD thesis, ETH Zurich, 2017.

[113] D. Meschede. *Optik, Licht und Laser*. Vieweg + Teubner, third edition, 2008.

[114] K. Visscher and G. K. Brakenhoff. Theoretical study of optically induced forces on spherical particles in a single beam trap ii: Mie scatterers. *Optik*, 90:57–60, 1992.

[115] M. E. Gehm, K. M. O'Hara, T. A. Savard, and J. E. Thomas. Dynamics of noise-induced heating in atom traps. *Physical Review A*, 58(5):3914–3921, nov 1998.

[116] B. Rodenburg, L. P. Neukirch, A. N. Vamivakas, and M. Bhattacharya. Quantum model of cooling and force sensing with an optically trapped nanoparticle. *Optica*, 3(3):318, mar 2016.

[117] J. Vovrosh, M. Rashid, D. Hempston, J. Bateman, M. Paternostro, and H. Ulbricht. Parametric feedback cooling of levitated optomechanics in a parabolic mirror trap. *Journal of the Optical Society of America B*, 34(7):1421, jul 2017.

[118] L. Novotny. Radiation damping of a polarizable particle. *Physical Review A*, 96(3):032108, sep 2017.

[119] J. Millen, P. Z. G. Fonseca, T. Mavrogordatos, T. S. Monteiro, and P. F. Barker. Cavity Cooling a Single Charged Levitated Nanosphere. *Physical Review Letters*, 114(12):123602, mar 2015.

[120] P. Z. G. Fonseca, E. B. Aranas, J. Millen, T. S. Monteiro, and P. F. Barker. Nonlinear Dynamics and Strong Cavity Cooling of Levitated Nanoparticles. *Physical Review Letters*, 117(17):173602, oct 2016.

[121] U. Delic. *in preparation*. Phd thesis, University of Vienna, 2018.

[122] A. C. Pflanzer, O. Romero-Isart, and J. I. Cirac. Master-equation approach to optomechanics with arbitrary dielectrics. *Physical Review A*, 86(1):013802, jul 2012.

[123] F. Marquardt, J. Chen, A. Clerk, and S. Girvin. Quantum Theory of Cavity-Assisted Sideband Cooling of Mechanical Motion. *Physical Review Letters*, 99(9):1–4, aug 2007.

[124] I. Wilson-Rae, N. Nooshi, W. Zwerger, and T. J. Kippenberg. Theory of Ground State Cooling of a Mechanical Oscillator Using Dynamical Backaction. *Physical Review Letters*, 99(9):093901, aug 2007.

[125] C. Genes, D. Vitali, P. Tombesi, S. Gigan, and M. Aspelmeyer. Ground-state cooling of a micromechanical oscillator: Comparing cold damping and cavity-assisted cooling schemes. *Physical Review A*, 77(3):033804, mar 2008.

[126] S. Gigan, H. R. Böhm, M. Paternostro, F. Blaser, G. Langer, J. B. Hertzberg, K. C. Schwab, D. Bäuerle, M. Aspelmeyer, and A. Zeilinger. Self-cooling of a micromirror by radiation pressure. *Nature*, 444(7115):67–70, nov 2006.

[127] O. Arcizet, P.-F. Cohadon, T. Briant, M. Pinard, and A. Heidmann. Radiation-pressure cooling and optomechanical instability of a micromirror. *Nature*, 444(7115):71–74, nov 2006.

[128] A. Schliesser, P. Del'Haye, N. Nooshi, K. J. Vahala, and T. J. Kippenberg. Radiation Pressure Cooling of a Micromechanical Oscillator Using Dynamical Backaction. *Physical Review Letters*, 97(24):243905, dec 2006.

[129] A. D. O'Connell, M. Hofheinz, M. Ansmann, R. C. Bialczak, M. Lenander, E. Lucero, M. Neeley, D. Sank, H. Wang, M. Weides, J. Wenner, J. M. Martinis, and A. N. Cleland. Quantum ground state and single-phonon control of a mechanical resonator. *Nature*, 464(7289):697–703, 2010.

[130] T. Rocheleau, T. Ndukum, C. Macklin, J. B. Hertzberg, A. A. Clerk, and K. C. Schwab. Preparation and detection of a mechanical resonator near the ground state of motion. *Nature*, 463(7277):72–75, jan 2010.

[131] G. S. Agarwal and S. Huang. Electromagnetically induced transparency in mechanical effects of light. *Physical Review A*, 81(4):041803, apr 2010.

[132] M. Fleischhauer, A. Imamoglu, and J. P. Marangos. Electromagnetically induced transparency: Optics in coherent media. *Reviews of Modern Physics*, 77(2):633–673, jul 2005.

[133] A. H. Safavi-Naeini, T. P. M. Alegre, J. Chan, M. Eichenfield, M. Winger, Q. Lin, J. T. Hill, D. E. Chang, and O. Painter. Electromagnetically induced transparency and slow light with optomechanics. *Nature*, 472(7341):69–73, apr 2011.

[134] S. Weis, R. Riviere, S. Deleglise, E. Gavartin, O. Arcizet, A. Schliesser, and T. J. Kippenberg. Optomechanically Induced Transparency. *Science*, 330(6010):1520–1523, dec 2010.

[135] E. D. Black. An introduction to Pound–Drever–Hall laser frequency stabilization. *American Journal of Physics*, 69(1):79–87, jan 2001.

[136] H.-A. Bachor and T. C. Ralph. *A Guide to Experiments in Quantum Optics*. Wiley-VCH, second edition, 2004.

[137] Analog Devices. *10 MHz, Four-Quadrant Multiplier/Divider AD734*, 2011. Rev. E.

[138] J. Klaers, J. Schmitt, F. Vewinger, and M. Weitz. Bose–Einstein condensation of photons in an optical microcavity. *Nature*, 468(7323):545–548, nov 2010.

[139] Analog Devices. *AD817, High Speed, Low Power, Wide Supply Range Amplifier*, 1995. Rev. B.

[140] P. Horowitz. *The Art of Electronics*. Cambridge University Press, third edition, 2015.

[141] H. Zumbahlen. *Mini Tutorial MT-202, Allpass Filter*. Analog Devices, 2012. Rev. 0.

[142] Analog Devices. *OP37 Low Noise, Precision, High Speed Operational Amplifier Operational Amplifier*, 2005. Rev. B.

[143] Analog Devices. *OP27 Low Noise, Precision Operational Amplifier*, 2015. Rev. H.